FINITE ELEMENT ANALYSIS OF NITROGEN SPECIES TRANSPORT AND TRANSFORMATION IN THE UNSATURATED ZONE

BY

Jagath Janapriya Kaluarachchi

Dissertation submitted to the Faculty of the
Virginia Polytechnic Institute and State University
in partial fulfillment of the requirement for the degree of

DOCTOR OF PHILOSOPHY

in

Environmental Sciences and Engineering

APPROVED:

J. C. Parker, Chairman

J. T. Novak

R. B. Reneau, Jr.

T. Kuppusamy

T. A. Dillaha

January, 1988

Blacksburg, Virginia

FINITE ELEMENT ANALYSIS OF NITROGEN SPECIES TRANSPORT AND TRANSFORMATION IN THE UNSATURATED ZONE

by

Jagath Janapriya Kaluarachchi

Committee Chairman: J. C. Parker

Environmental Sciences and Engineering

(ABSTRACT)

A two-dimensional finite element model was developed to predict water flow and nitrogen species transport and transformation in variably saturated soil. In the finite element analysis various numerical algorithms were examined to evaluate methods of improving the efficiency of the traditional finite element approach. Results indicate that when undeformed linear rectangular elements or linear traingular elements were used, the method of influence coefficients is more efficient than traditional numerical integration methods in evaluating the element matrices while maintaining accuracy. Also with moderately nonlinear flow problems, use of a fourth order Runge-Kutte method produced improved effciency over fixed or variable time step schemes for time integration. Hysteretic simulations with air entrapment showed that effects of hysteresis are greatly enhanced by the presence of air entrapment due to large differences in water contents between different saturation paths. Flux-controlled boundary conditions produced negligible hysteretic effects while maximum effects were caused under potential type boundary conditions. The magnitude of

hysteretic effects are also affected by the definition of initial conditions. Heterogenity in the porous medium tends to reduce hysteretic effects. The finite element model developed to solve the convective-dispersive equation for nitrogen transport utilized an upstream weighting scheme to reduce numerical oscillation associated with low dispersion coeffcients. The accuracy and validity of the model were evaluated using both published and field data. The results indicate overall predictions of various nitrogen fractions are quite sensitive to the first order nitrfication rate. However, use of kinetic constants based on published results in the literature, especially in the absence of detailed field investigations, may still be sufficient to provide dependable results through simulations. Hysteresis greatly affects the transport of nitrogen species under potential type boundary conditions, but these effects are reduced substantially in the presence of high intensity line sources. Under such circumstances, it is sufficient to neglect hysteresis and use either the main drainage or the main wetting branch of the pressure-saturation relationship for simulations.

TO MY LATE FATHER AND MOTHER

ACKNOWLEDGEMENTS

I wish to express my deepest gratitute to Dr. J. C. Parker for his constant encouragement and guidance throughout the course of this research. I am also thankful to the members of the graduate committee, Dr. R. B. Reneau, Dr. John Novak, Dr. T. Dillaha, Dr. T. Kuppusamy and Dr. Clifford Randall for their support and cooperation during my course of studies. I wish to thank all the people associated with my work during the last three years, especially to my collegues . Acknowledgements are also due to of the Agronomy department. Finally I take this opportunity to thank the members of my family and the Health Department of Virginia for providing the necessary financial support.

TABLE OF CONTENTS

CHAPTER I

INTRODUCTION

Contamination of groundwater resources is a common occurrence associated with land application of partially treated wastewater, disposal of hazardous materials in an uncontrolled manner, and application of fertilizer and pesticides to plants. In industrialized areas, groundwater pollution sources arise from disposal of untreated or partially treated industrial wastes containing heavy metals or hydrocarbon compounds. In rural areas, groundwater pollution may occur due to agricultural chemical usage or the disposal of secondary wastewater via subsurface drainfields. The most common form of pollution due to such application is increased loading of chemical species especially nitrogen to the aquifers. Problems associated with nitrogen species are more difficult to assess due to the complex nature of the nitrogen cycle. Nitrogen in soils can exist in various forms depending on the microbial population and environmental factors such as soil temperature, pH, water content and carbon content. The most common soluble forms of nitrogen in soils are NH_4^+ and NO_3^- while organic nitrogen remains mostly as an immobile fraction.

From the standpoint of predicting groundwater contaminants, the most important nitrogen species is NO_3^- due to its rapid movement within the soil profile. This is mainly due to limited adsorption of NO_3^- on soil solids compared to NH_4^+ which is subjected to adsorption on cation exchange sites. Within the nitrogen cycle, various nitrogen

fractions are linked together through biologically mediated kinetics. These kinetic parameters control the reactions and are dependent on numerous environmental factors. Water content of the soil is one of the important factors associated with the distribution of various nitrogen species. Anaerobic conditions usually prevail along the few upper layers due to higher water content. Under such conditions, free O_2 is generally low and active denitrifying bacteria will reduce NO_3^- to N_2. Adsorption of NH_4^+ to exchange sites is also rapid within the saturated zone and active movement of NH_4^+ will occur if all exchange sites are fully occupied. Soil pH also plays a major role in determining the distribution of different nitrogen species in the system. Under acidic conditions, nitrogen occurs mainly in the form of NH_4^+ while under basic conditions, NH_4^+ will be transformed to NH_3 which can be released from soil as a gas.

The foregoing discussion mainly focused attention on the complexicity associated with the nitrogen cycle in soils. In nitrogen simulation studies, nitrogen species transport is seldomly restricted to the saturated flow domains. Since nitrogen transport is strongly influenced on processes which occur in the unsaturated zone, knowledge of the dynamics of flow in the unsaturated zone is critical to the prediction of nitrogen transport. Unfortunately, analysis of water flow in the unsaturated zone is complex from a mathematical point of view due to the nonlinear and hysteretic behavior of soil hydraulic properties. For accurate prediction of nitrogen transport in field conditions, it is important to obtain the correct water content and velocity distribution of the flow domain. Solution of the flow equation

usually requires a numerical approach such as the finite difference or finite element method. Another approach is to simplify the mathematical problem and adopt a quasi-analytical method. The serious limitation of the latter approach is that in simplifying the problem, the actual conditions in the field are neglected and the accuracy in the final prediction is seriously degraded. Numerical solutions on the otherhand usually require substantial computing effort especially in the case of large field problems. Also if simulations are carried over a long period of time under highly nonlinear flow conditions, computing effort can be substantial. In addition to the basic solution of the flow problem, it is important to verify the accuracy of the solution with respect to conservation of mass.

Solution of the convective-dispersive equation for any given species is straightforward using numerical techniques when nonlinearity is absent in the constitutive relations. In transport problems, nonlinearity will arise mainly due to nonlinear adsorption isotherms. Once a mathematical model is developed, it is important to evaluate the accuracy of the model. Evaluation of the accuracy of a given numerical model is best accomplished by comparison with experimental data. In the absence of such data, an equally preferable approach is to perform the accuracy evaluation using published data or analytical solutions to simplified problems. For calibration purposes of a given site, field experiments are needed to obtain the governing constants of the flow domain and the model can be used for subsequent simulations for a given set of field conditions.

In this study, a suitable numerical model will be described to solve the problem of nitrogen transport and transformation in the unsaturated zone in an efficient manner. Attention will focus on various aspects of the flow and transport equation solutions. Considerations in the flow problem will include analysis of effects of different boundary conditions such as seepage and surface controlled boundaries, hysteresis which includes air entrapment in the pressure-saturation relationships and soil heterogenity. The convective-dispersive transport of two nitrogen species will be considered and a suitable numerical approach is developed. Effects of hysteresis on the transport will also be addressed. Chapter II of this study will address the topic of water flow in the unsaturated zone and Chapter III is an extension dealing with the hysteretic effects. Chapter IV will discuss the numerical model for the transport of nitrogen species in the unsaturated zone and finally Chapter V will focus attention on the effects of hysteresis on transport mechanisms. Publications associated with this work are cited in Appendix F.

CHAPTER II

FINITE ELEMENT ANALYSIS OF WATER FLOW IN VARIABLY SATURATED SOIL

ABSTRACT

A two-dimensional Galerkin finite element model for water flow in variably saturated soil is presented. A fourth-order Runge-Kutte time integration method is employed which is shown to allow use of time steps approximately 2 times greater than for a traditional finite difference approximation of time derivatives. Computer execution costs for the Runge-Kutte method are greater than for the finite difference approximation for short total simulation times due to the start up cost of the Runge-Kutte method but for longer simulation times the Runge-Kutte method yields considerable reduction in computational effort. A comparison of the method of influence coefficients and 2 x 2 Gaussian integration to compute element matrices indicates that the influence coefficient method reduces execution time to 40% of that required for numerical quadrature. Computed pressure heads and fluxes using the influence coefficient method or numerical integration are found to be in close agreement with each other even under conditions of highly nonlinear soil properties in a heterogeneous domain.

INTRODUCTION

Contamination of soil and groundwater resources due to waste disposal in landfills, drainfields, lagoons and other facilities is of great importance from environmental and economic viewpoints. Because the major mechanism of chemical transport through vadose and saturated zones is advection, accurate models for water flow under variably saturated conditions is a prerequisite to modeling solute movement. Numerical models for variably saturated flow commonly employ finite difference or finite element techniques (Cooley, 1971; Neuman, 1973; Yeh and Ward, 1980; Wagner et al., 1980). One of the major difficulties in modeling variably saturated flow arises due to the highly nonlinear nature of the medium properties which may lead to numerical instability. Use of refined discretizations of temporal and spatial domains diminish such problems but may increase computational costs markedly. A number of techniques may be employed to handle nonlinear problems more efficiently such as predictor-corrector methods for extrapolation in time (Guymen et al., 1970), automatic time marching criteria (Cooley, 1971), and lumping of mass matrices in the finite element method (Huyakorn and Pinder, 1983). Another useful technique which may markedly reduce computational costs for finite element solutions is the method of influence coefficients. This method, which is applicable to spatial domains that are discretized by linear rectangular or triangular elements, eliminates costly numerical integration for computing element matrices (Huyakorn et al., 1984).

In the present paper, we present a finite element solution for flow

in a two-dimensional variably saturated medium which incorporates general time-dependent boundary conditions and internal sources or sinks which may arise in modeling subsurface drainfield lines in vertical section or wells in plan view. Consideration is given to a number of methods of improving computational efficiency with particular attention to application of the method of influence coefficients and a fourth-order predictor-corrector time integration method. Accuracy and computational efficiency of the model will be evaluated by comparison with analytical solutions and results of different numerical schemes.

NUMERICAL MODEL DESCRIPTION

Governing Equations

The single-phase formulation of the equations describing flow in a variably saturated domain under isothermal conditions in two dimensions can be written:

$$U(\psi) \equiv \frac{\partial}{\partial x}\left[K_x(\psi)\,\frac{\partial \phi}{\partial x}\right] + \frac{\partial}{\partial z}\left[K_z(\psi)\,\frac{\partial \phi}{\partial z}\right] + Q - C(\psi)\,\frac{\partial \psi}{\partial t} = 0 \qquad (2.1)$$

where U is a differential operator, ψ is the pressure head, $\phi=\psi+z$ is the total hydraulic head, K_x and K_z are components of the conductivity tensor along the assumed principal directions x and z with z the vertical coordinate measured positive upwards, Q is the point source or sink term for the region, $C = \partial\theta/\partial\psi$ is the specific water capacity with θ the volumetric water content, and t is time. Initial and boundary conditions for (2.1) are

$$\psi(x,z,0) = \psi_o(x,z) \qquad \text{for } t = 0 \text{ in } R \tag{2.2a}$$

$$\psi(x,z,t) = \psi_1(x,z,t) \qquad \text{for } t > 0 \text{ on } T_1 \tag{2.2b}$$

$$-\left[K_X \frac{\partial \Phi}{\partial x} \bar{n}_X + K_Z \frac{\partial \Phi}{\partial z} \bar{n}_Z\right] . \bar{n} = q_n(t) \quad \text{for } t > 0 \text{ on } T_2 \tag{2.2c}$$

where R denotes the entire flow domain and T_1 and T_2 are portions of the boundary. Equation (2.2a) describes the initial condition in terms of the pressure function ψ_o. Equation (2.2b) describes the boundary T_1 on which Dirichlet or potential-type boundary conditions are applicable. Equation (2.2c) describes the Neumann or flux-type boundary condition on T_2 where $\bar{n}$ is the unit normal vector drawn outward from the boundary, $\bar{n}_X$ and $\bar{n}_Z$ are unit vectors in the x and z directions and q_n is the magnitude of the flux normal to the boundary. Water flux at any point in the flow region is given by:

$$q_X = -K_X \frac{\partial \Phi}{\partial x} \tag{2.3a}$$

$$q_Z = -K_Z \frac{\partial \Phi}{\partial z} \tag{2.3b}$$

where q_X and q_Z are components of flux in the x and z directions. In equations (2.1) to (2.3), the hydraulic properties K_X, K_Z and C are in general highly nonlinear functions of pressure head ψ.

Discretization of Spatial Domain

Galerkin analysis. Equation (2.1) can be solved using the method of weighted residuals based on Galerkin's approximation. Assume

$$\psi(t) = \sum_{j=1}^{m} N_j(x,z)\ \psi_j(t) \tag{2.4}$$

where m is the number of nodes per element, N_j is the shape function describing ψ, and ψ_j is the nodal value of ψ at node j.

Applying Galerkin's approximation to (2.1) gives

$$\int_R N_i U(\psi)\ dR = 0 \tag{2.5}$$

Using the relationship $\Phi = \psi + z$ and Green's theorem on (2.5) gives,

$$\int_R C(\psi) N_i \frac{\partial \psi}{\partial t} dR + \int_R \left[K_x(\psi) \frac{\partial N_i}{\partial x} \frac{\partial \psi}{\partial x} + K_z(\psi) \frac{\partial N_i}{\partial z} \frac{\partial \psi}{\partial z} \right] dR$$

$$+ \int_R K_z(\psi) \frac{\partial N_i}{\partial z}\ dR - \int_S N_i \left[K_x(\psi) \frac{\partial \Phi}{\partial x} + K_z(\psi) \frac{\partial \Phi}{\partial z} \right]\ dS - \int_R N_i Q\ dR = 0 \tag{2.6}$$

where S refers to the part of the surface on which the surface integral is applicable.

From (2.2c) and (2.6):

$$\int_R N_i C(\psi) \frac{\partial \psi}{\partial t}\ dR + \int_R \left[K_x(\psi) \frac{\partial N_i}{\partial x} \frac{\partial \psi}{\partial x} + K_z(\psi) \frac{\partial N_i}{\partial z} \frac{\partial \psi}{\partial z} \right] dR$$

$$+ \int_R K_z(\psi) \frac{\partial N_i}{\partial z} \, dR + \int_S N_i q_n \, dS - \int_R N_i Q \, dR = 0 \tag{2.7}$$

We may rewrite (2.7) in matrix form after applying the approximation given by (2.4) to obtain

$$[M] \{\partial\psi/\partial t\} + [E] \{\psi\} + \{F\} = 0 \tag{2.8}$$

where

$$M^e_{ij} = \int_{R_e} C(\psi) \, N_i N_j \, dR \tag{2.9a}$$

$$E^e_{ij} = \int_{R_e} \left[K_x(\psi) \frac{\partial N_i}{\partial x} \frac{\partial N_j}{\partial x} + K_z(\psi) \frac{\partial N_i}{\partial z} \frac{\partial N_j}{\partial z} \right] dR \tag{2.9b}$$

$$F^e_i = \int_{S_e} N_i q_n \, dS + \int_{R_e} K_z(\psi) \frac{\partial N_i}{\partial z} \, dR - \int_{R_e} N_i Q \, dR \tag{2.9c}$$

where e denotes the element quantities. For computational efficiency, the mass matrix [M] can be lumped as follows:

$$M^e_{ij} = \begin{cases} \sum_{J=1}^{m} \int_{R_e} C(\psi) N_i N_j \, dR & i = j \\ 0 & i \neq j \end{cases} \tag{2.9d}$$

Treatment of sources or sinks. If a point source or sink, Q^*, is located at a node, it can be added directly to the final load vector {F} at the node after weighting by an appropriate time incremental factor depending on the time integration scheme employed. In the event that

a point source or sink is located within an element, the following assumption is used to distribute the source proportionately to each node of the element (Segerlind, 1984):

$$Q = Q^* \ \delta(x-x_o)\ \delta(z-z_o) \tag{2.10}$$

where δ is a unit impulse function and x_o and y_o are coordinates of the point source. Using (2.10), the source-sink term in (2.9c) is given by

$$\int N_i Q dR = Q^* N_i(x_o, z_o) \tag{2.11}$$

Element properties and element integration. A detailed description of shape functions and related computations is given by Huyakorn and Pinder (1983). In the present analysis, we consider linear rectangular and linear triangular elements (Fig. 2.1). Linear shape functions for rectanglar elements can be defined as:

$$N_i(\xi,\eta) = \frac{1}{4}(1 + \xi\xi_i)(1 + \eta\eta_i), \qquad i = 1,\ldots, 4 \tag{2.12}$$

where ξ and η are local coordinates and $\xi_i = \pm 1$, $\eta_i = \pm 1$ are nodal local coordinates. Transformation from local to global coordinates is given by

$$x = \sum_{i=1}^{4} N_i(\xi,\eta)x_i \tag{2.13a}$$

$$z = \sum_{i=1}^{4} N_i(\xi,\eta)z_i \tag{2.13b}$$

In the case of triangular elements,

$$N_i(x,z) = \frac{1}{2\Delta}(\alpha_i + \beta_i x + \gamma_i z) \text{ and } i = 1,2,3 \tag{2.13c}$$

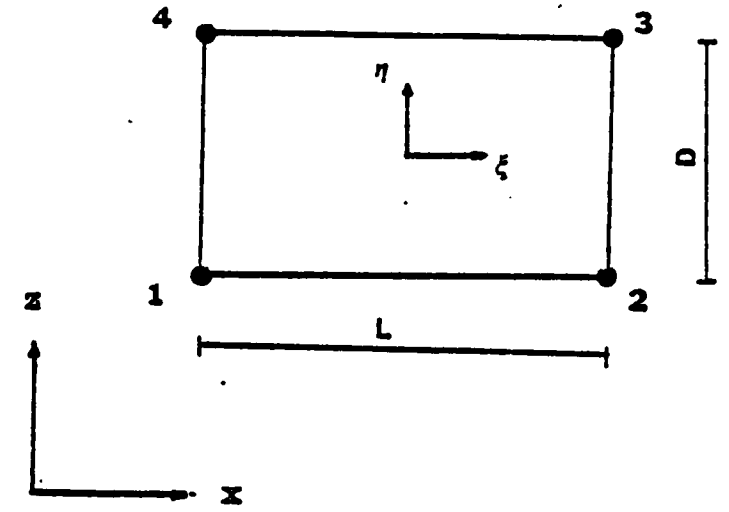

A.

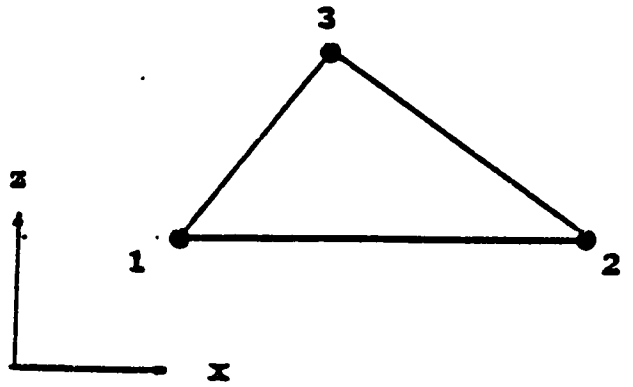

B.

Figure 2.1 Element geometry for (a) linear rectangular element and (b) linear traingular element.

where Δ is the area of the element. Values of α_i, β_i, γ_i, and Δ are defined in Appendix B.

Element integration and influence coefficient method. To carry out the element integrations indicated by (2.9a) - (2.9c), two methods are investigated. The first procedure, which is conventional in finite element analysis, utilizes numerical integration with a 2 x 2 Gaussian quadrature scheme. In this method, the hydraulic properties within an element are evaluated as

$$K_x(\psi) = \sum_{i=1}^{m} N_i \, [K_x(\psi)]_i \qquad (2.14a)$$

$$K_z(\psi) = \sum_{i=1}^{m} N_i \, [K_z(\psi)]_i \qquad (2.14b)$$

$$C(\psi) = \sum_{i=1}^{m} N_i \, [C(\psi)]_i N_i \qquad (2.14c)$$

where N_i are the same shape functions employed in (2.4) and i refers to the local nodal numbering.

In the method of influence coefficients proposed by Huyakorn et al. (1984) for utilization with linear rectangular or triangular elements, the required element integrations are carried out analytically eliminating the need for costly numerical integration. Huyakorn et al. demonstrated 90 percent cost savings without loss in accuracy for one-dimensional flow problems using this technique, but did not evaluate the accuracy or efficiency for two-dimensional flow problems. Because the accuracy of results obtained from solute transport models

depends strongly on accuracy in predicting nodal hydraulic fluxes, we are particularly interested in evaluating the effects of the influence coefficient method on nodal flux predictions for two-dimensional flow.

According to Huyakorn and Pinder (1984), (2.9a) - (2.9c) for a rectangular element can be written with flux and point source terms neglected as

$$[M] = \frac{DLC}{4} [T^*] \tag{2.15a}$$

$$[E] = \frac{DK_X}{L} [S_X^*] + \frac{LK_Z}{D} [S_Z^*] \tag{2.15b}$$

$$\{F\} = \frac{LK_Z}{2} \{V^*\} \tag{2.15c}$$

Where C, K_X K_Z refer to element centroid values of $C(\psi)$, $K_X(\psi)$, and $K_Z(\psi)$, D and L are dimensions of the element (Fig. 2.1a) and matrices $[T^*]$, $[S_X^*]$, $[S_Z^*]$ and vector $\{V^*\}$ are given in Appendix A. Appendix B gives the results of a similar analysis for linear triangular elements.

Nodal fluxes. When the method of influence coefficients is used, the hydraulic flux given by (2.3a) and (2.3b) can be approximated for linear rectangular elements by:

$$q_X = K_X \cdot (\Phi_1 + \Phi_4 - \Phi_2 - \Phi_3)/2L \tag{2.16a}$$

and

$$q_Z = K_Z \cdot (\Phi_1 + \Phi_2 - \Phi_3 - \Phi_4)/2D \tag{2.16b}$$

add for linear triangular elements by:

$$q_X = K_X (\beta_1\Phi_1 + \beta_2\Phi_2 + \beta_3\Phi_3) \tag{2.16c}$$

and

$$q_z = K_z\ (\gamma_1\Phi_1 + \gamma_2\Phi_2 + \gamma_3\Phi_3) \tag{2.16d}$$

Equations (2.3a) and (2.3b) can also be numerically integrated to predict nodal fluxes. For this purpose, the Galerkin approximation can be used and the final element equations are

$$[W]\ \{q_x\} = [Y]\ \{\Phi\} \tag{2.17a}$$

$$[W]\ \{q_z\} = [Y^*]\ \{\Phi\} \tag{2.17b}$$

where

$$W^e_{ij} = \int_{R_e} N_i\ N_j\ dR \tag{2.17c}$$

$$Y^e_{ij} = \int_{R_e} K_x(\psi)\ N_i\ \frac{\partial N_j}{\partial x}\ dR \tag{2.17d}$$

$$Y^{*e}_{ij} = \int_{R_e} K_z(\psi)\ N_i\ \frac{\partial N_j}{\partial z}\ dR \tag{2.17e}$$

Here shape functions describing the total potential Φ within an element are considered to be same as those describing element geometry.

Time Marching Schemes

Finite difference method. The finite difference form of (2.8) can be written at time level $(k+\omega)$ as:

$$[A]^{k+\omega}\ \{\psi\}^{k+1} = \{B\}^{k+\omega} \tag{2.18}$$

where

$$[A]^{k+\omega} = \frac{[M]}{\Delta t_{fd}}^{k+\omega} + \omega[E]^{k+\omega} \tag{2.19a}$$

$$\{B\}^{k+\omega} = \left[\frac{[M]^{k+\omega}}{\Delta t_{fd}} - (1-\omega)\ [E]^{k+\omega} \right] \{\psi\}^{k} - \{F\}^{k+\omega} \qquad (2.19b)$$

and

$$\{\psi\}^{k+\omega} = (1-\omega)\ \{\psi\}^{k} + \omega\{\psi\}^{k+1} \qquad (2.19c)$$

Here k refers to any time level at which the pressure heads are known, Δt_{fd} is the time increment for the finite difference scheme, and ω is a time-weighting coefficient. For ω = 0, 1 and 0.5, we obtain explicit, fully implicit and Crank-Nicolson methods, respectively.

Equations (2.17) and (2.18) are solved iteratively with the first estimate of $\{\psi\}^{k+1}$ obtained by linear extrapolation from the k-1 and k time steps subsequent to the first time increment. Evaluation of [M], [E] and {F} at the $k+\omega$ time level employs soil hydraulic properties corresponding to $\{\psi\}^{k+\omega}$ given by (2.18c). Iteration is continued until convergence is obtained for $\{\psi\}^{k+1}$.

Predictor-corrector method. Although the finite-difference scheme may be applied to highly nonlinear problems if care is taken in selecting a suitable time increment, potentially greater efficiency is possible by the use of predictor-corrector methods. Here we employ a fourth-order Runge-Kutte method to integrate (2.8). The resulting recursion formula may be written as (Carnahan et al., 1969):

$$[A^*]\ \{\psi\}^{k+1} = \{B^*\} \qquad (2.20)$$

where

$$[A^*] = [M]^{k+1} + \frac{12}{25}\ \Delta t_{rk}\ [E]^{k+1} \qquad (2.21a)$$

$$\{B^*\} = \frac{12}{25}\,\Delta t_{rk}\,\{F\}^{k+1} + \frac{[M]^{k+1}}{25}\cdot$$

$$\left\{48\{\psi\}^{k} - 36\{\psi\}^{k-1} + 16\{\psi\}^{k-2} - 3\{\psi\}^{k-3}\right\} \qquad (2.21b)$$

in which Δt_{rk} is the time step for the Runge-Kutte analysis. For the first iteration of (2.20), $\{\psi\}^{k+1}$ is extrapolated via a cubic polynomial using known values of $\{\psi\}$ at k, k-1, k-2 and k-3 time levels. The new vector $\{\psi\}^{k+1}$ obtained from solution of (2.20) is employed again in (2.21) and the procedure iterated until convergence occurs.

Before the Runge-Kutte procedure can be employed, a sufficient number of time steps must be carried out by the finite difference scheme to generate results at time levels Δt_{rk}, $2\Delta t_{rk}$ and $3\Delta t_{rk}$. If Δt_{fd} is selected to be an integer fraction of Δt_{rk} (i.e., $\Delta t_{rk}/\Delta t_{fd} = N$), then after 3N time steps using the finite difference scheme, the predictor-corrector method may be implemented.

A computer code HYDRO written in FORTRAN was developed to implement the finite element solution of the flow problem described in the preceding sections. The program has the capability of stipulating time-dependent flux- or potential-type boundary conditions with point sources located arbitrarily within the domain. Linear rectangular and triangular elements can be employed. Options in the program allow use of either numerical integration or the influence coefficient method for element matrices and either finite difference or Runge-Kutte time integration. In the symmetric global matrix, only the upper elements are stored. Solution of the final assembled matrix equations is performed using a direct Gaussion elimination procedure.

RESULTS AND DISCUSSION

Accuracy and Stability

In order to verify the general model formulation and specifically the treatment of point sources and sinks, we consider first a simple case of saturated flow to a well in a confined aquifer of finite dimensions with a single recharge boundary. The problem may be posed as follows:

$$S \frac{\partial H}{\partial t} = T_x \frac{\partial^2 H}{\partial x^2} + T_y \frac{\partial^2 H}{\partial y^2} + Q\, \delta(x-x_w)\, \delta(y-y_w) \qquad (2.22)$$

subject to

$$H = 0 \quad x_o \leq x \leq x_1 \quad y_o \leq y \leq y_1 \quad t = 0 \qquad (2.23a)$$

$$H = H_o \quad x = x_o \quad y_o \leq y \leq y_1 \quad t > 0 \qquad (2.23b)$$

$$\partial H/\partial x = 0 \quad x = x_1 \quad y_o \leq y \leq y_1 \quad t > 0 \qquad (2.23c)$$

$$\partial H/\partial y = 0 \quad x_o \leq x \leq x_1 \quad y = y_o \quad t > 0 \qquad (2.23d)$$

$$\partial H/\partial y = 0 \quad x_o \leq x \leq x_1 \quad y = y_1 \quad t > 0 \qquad (2.23e)$$

where H is piezometric head, x and y are horizontal coordinates, S is the storage coefficient, T_x and T_y are transmissivities, and Q is the pumping rate of a well located at point (x_w, y_w). Recharge occurs along the plane at $x = x_o$ (Fig. 2.2). Analytical solutions of (2.22) subject to (2.23) for constant S, T_x and T_y have been given by Cleary and Ungs (1977).

We consider here an example problem discussed by the latter

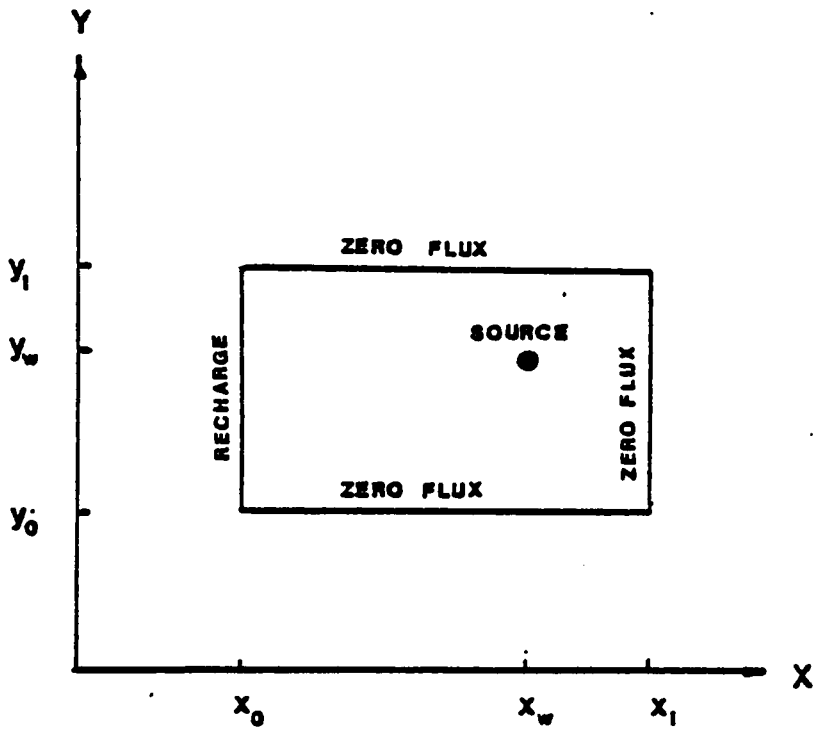

Figure 2.2 Flow domain for the point source problem

authors for $H_o = 0$, $S = 0.01$, $T_x = T_y = 745$ m^2 day^{-1} and $Q = 3500$ m^3 day^{-1}. Three finite element meshes were used to predict drawdown after 10 days using a Runge-Kutte time step of 2 days. The configuration of the spatial domain and the three element meshes are shown in Fig. 2.3. A comparison of analytical and numerical results for the three mesh configurations for a transect taken perpendicular to the recharge boundary are shown in Fig. 2.4. Reasonably accurate results are observed especially with mesh C which has fewer total nodes than meshes A and B but finer discretization in the vicinity of the well.

We consider next a problem described by Wagner et al. (1980) involving a partially saturated soil subjected to a downward flux at the soil surface with a water table initially located at a depth of 2.3 m (Fig. 2.5a). The soil surface and the water table both have a slope of 1:332. Initial pressure head values correspond to an equilibrium state. Lateral boundaries below the water table are constant head. Lateral boundaries above the water table and the lower boundary are zero flux. The mesh discritization used by previous authors is shown in Fig. 2.5b and is used in the present analysis. We wish to consider first the stability and accuracy of the proposed Runge-Kutte time integration scheme in comparison to the finite difference method for fixed time increment size for the problem described above with the surface flux equal to 0.01 cm/hr. The element matrices for both methods used the 2 x 2 Gaussian quadrature scheme. Pressure head variations along the initial water table were computed at different simulation times using different time increments for each time integration method. Pressure

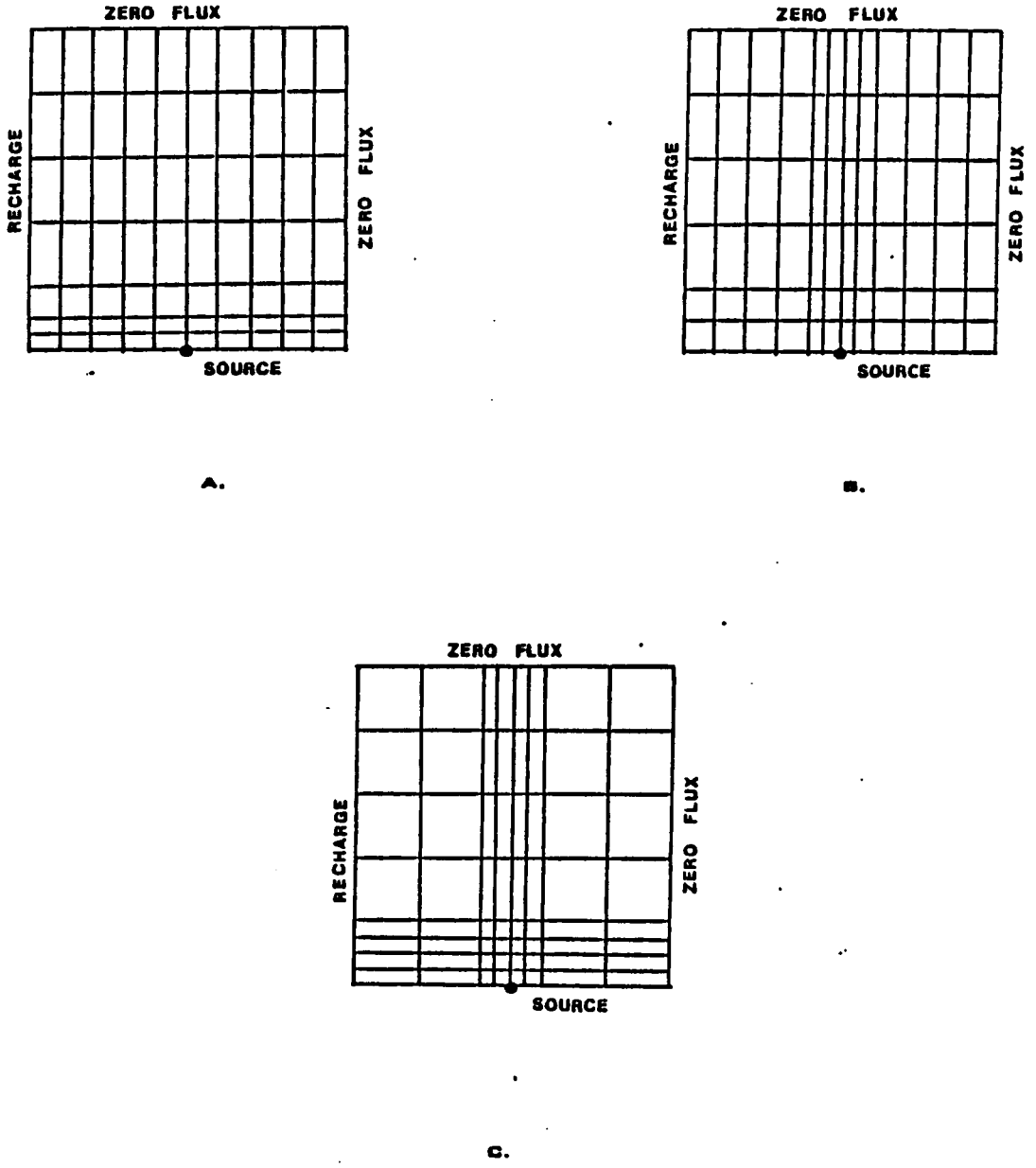

Figure 2.3 Discretized finite element domain for point-source problem. Only top part of the domain shown due to symmetry (a) Mesh A; (b) Mesh B; (c) Mesh C.

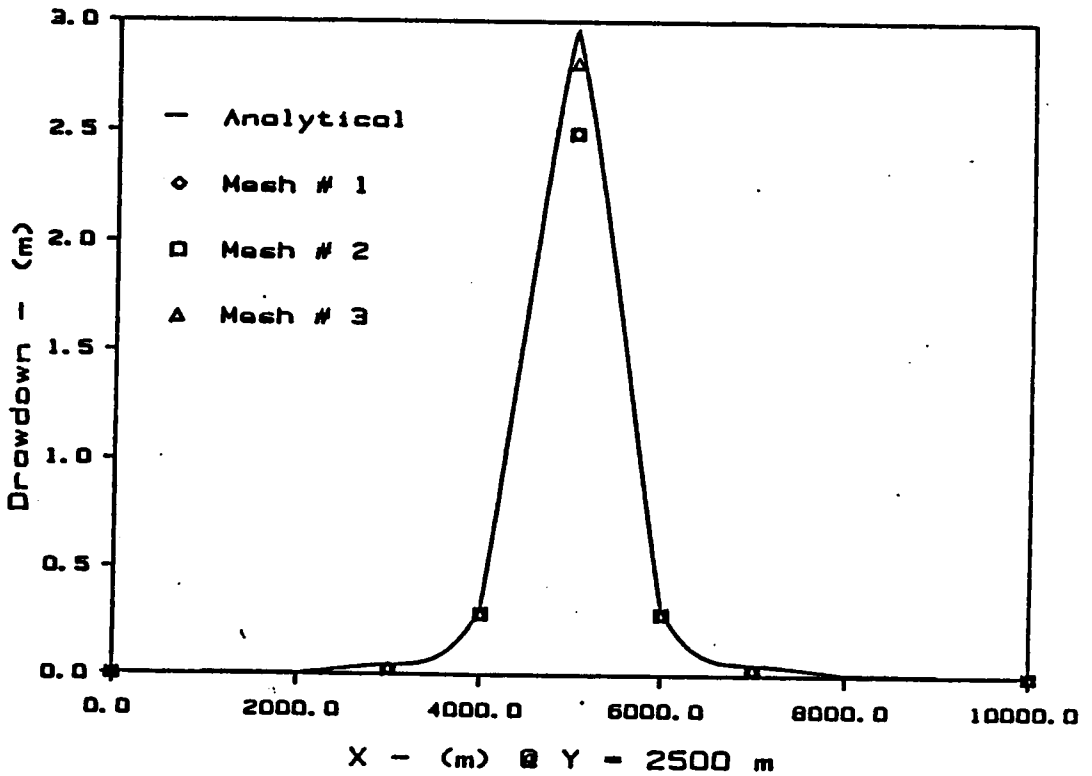

Figure 2.4 Drawdown along a transect perpendicular to the recharge plane at a time of 10 days for the point-source problem.

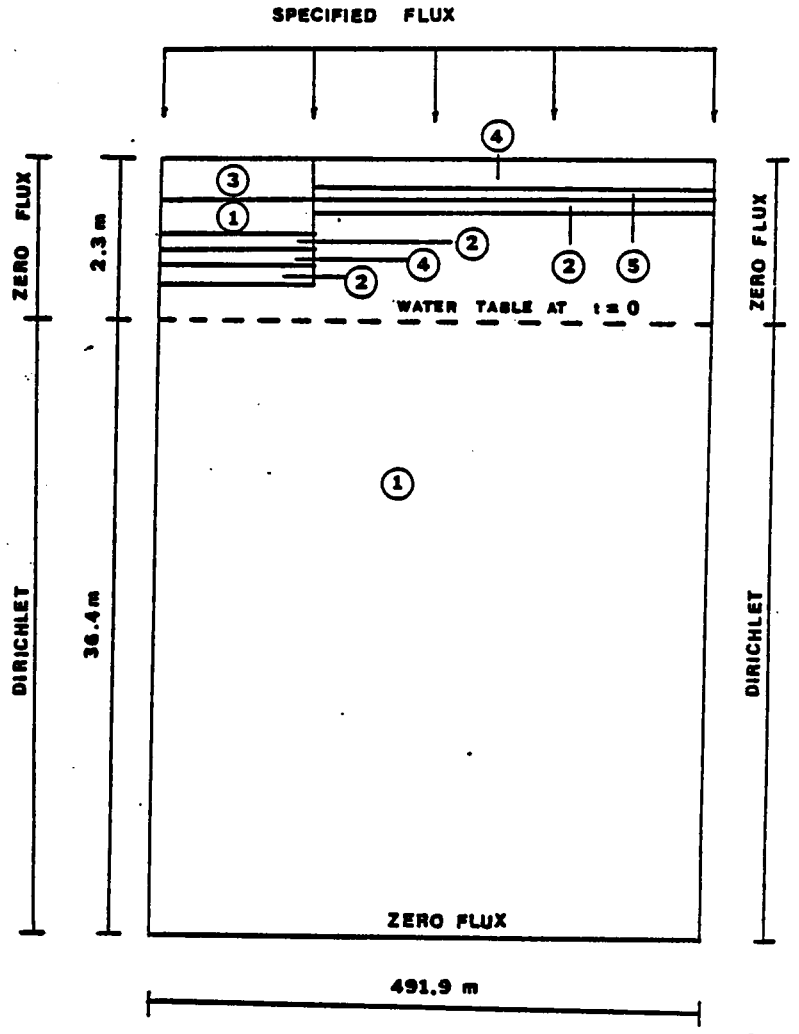

Figure 2.5a Flow domain for the problem of Wagner et al. (1980). Boundary conditions and material distribution. Numbers on curves denote material type given in Appendix C.

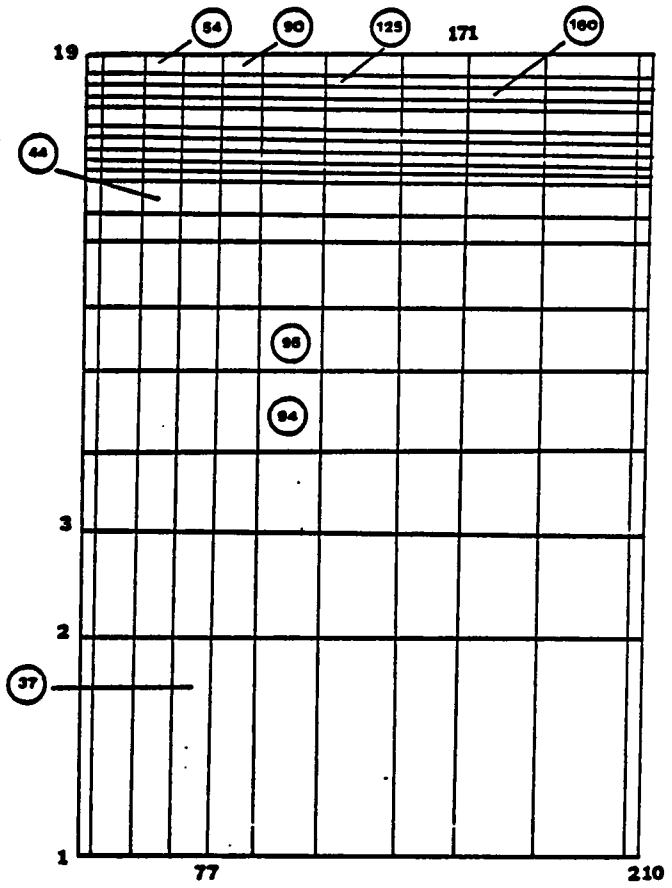

Figure 2.5b Flow domain for the problem of Wagner et al. (1980). Finite element discretization with node and element numbering. Selected elements identified for later reference.

head values at this level were selected because changes in head were maximum at this location. In the analyses by both methods, allowable number of iterations for a given time increment was 8 for a convergence accuracy of 0.001 cm. If results for a given time increment were found to deviate excessively from the corresponding results at a lower time increment, the higher time increment was not considered to be suitable for the analysis.

In the Runge-Kutte method, two time increments, 15 and 60 hours were selected and computation was continued to simulation times much greater than 3 Δt_{rk} to clearly show the accuracy and stability of the method as compared to the finite difference method. Three finite difference subdivisions of the first three time increments were used for both 15 and 60 hour Runge-Kutte time increments to start the method. The results in Fig. 2.6a show that at the larger time increment of 60 hours, some deviation from the correct solution occurs at higher times, however, the deviations are not large. The results at a time increment of 50 hours although not shown, predicted excellent agreement with the results for a time increment of 15 hours. Further increases of Δt_{rk} beyond 60 hours produced large deviations in the solutions and a higher number of iterations to converge. These results suggest that Δt_{rk} of approximately 60 hours to be the optimum for this problem.

Analysis using the finite difference method showed the maximum time increment satisfying the previously mentioned convergence criteria to be 30 hours. Results of Δt_{fd} equal to 30 hours yielded essentially identical results to those for 15 hours (Fig. 2.6b). Comparison of the

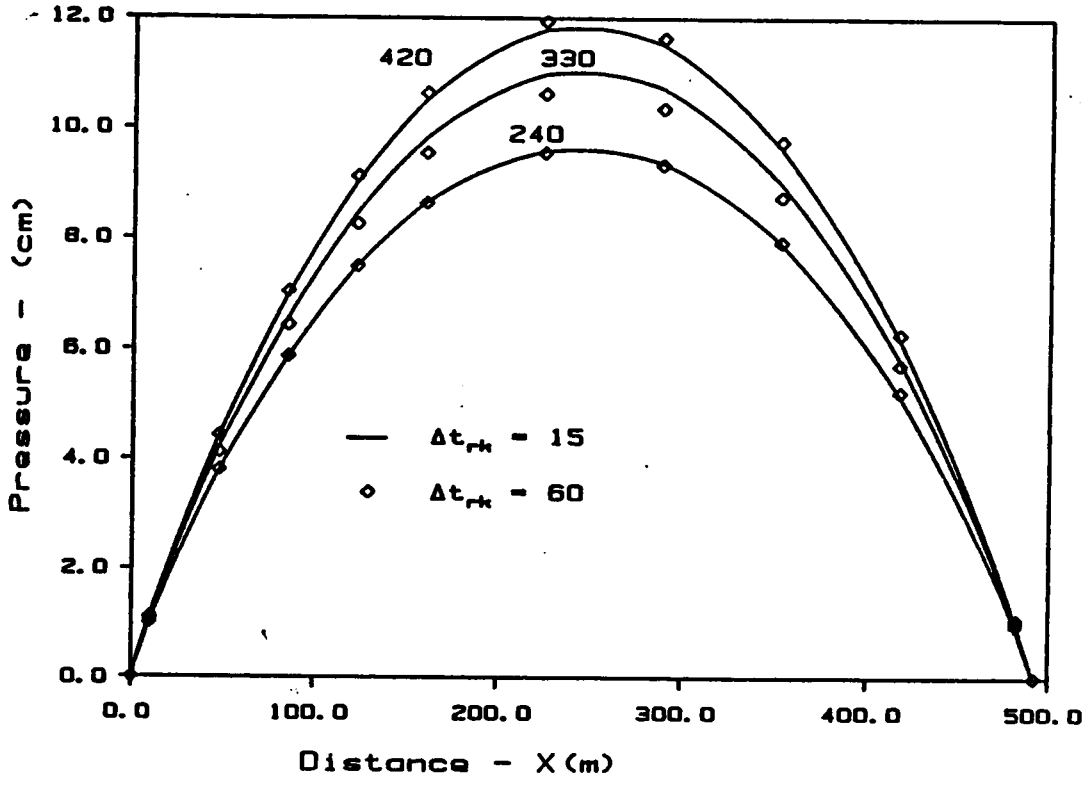

Figure 2.6a Accuracy and stability of the computed pressure heads at the level of the original watertable for Runge-Kutte time increments. Numbers on curves denote time in hours.

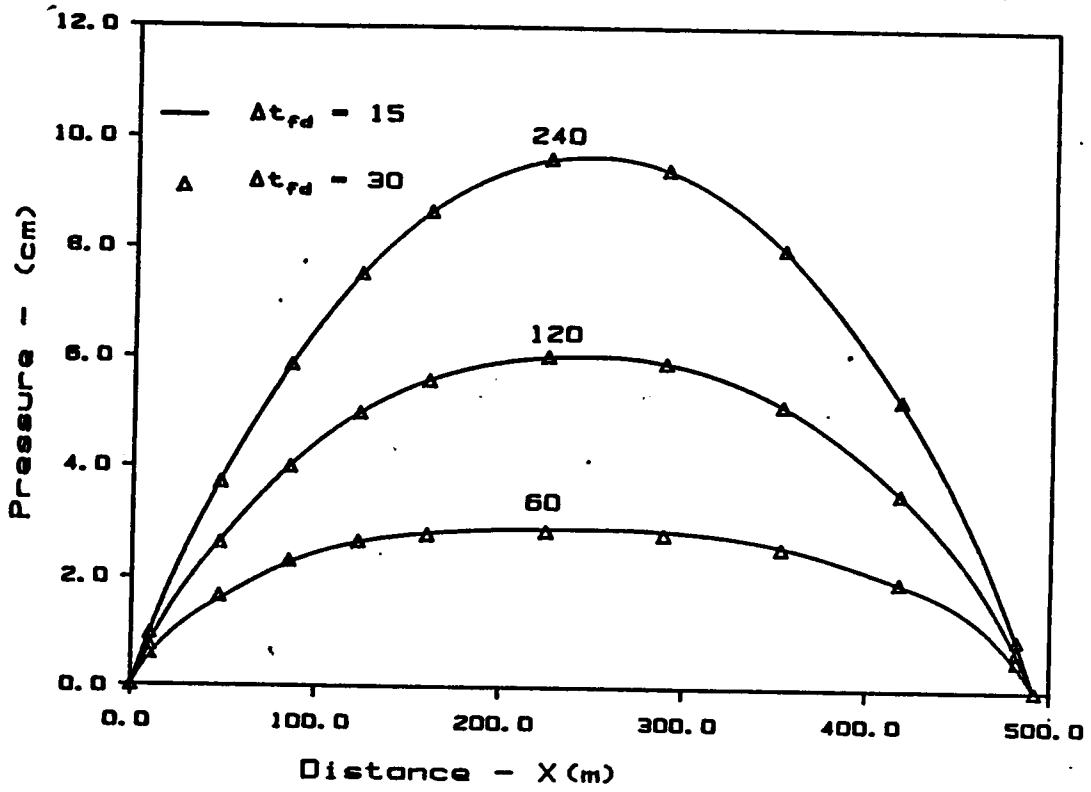

Figure 2.6b Accuracy and stability of the computed pressure heads at the level of the original watertable for two finite difference time increments. Numbers on curves denote time in hours.

Runge-Kutte and finite difference methods indicate agreement between the results and shows that the proposed computational procedure yields accurate and stable results for time steps significantly greater than the conventional finite difference approach.

Time Integration Scheme

We wish now to evaluate computational efficiency of the Runge-Kutte time integration method in comparison with the traditional finite difference scheme using either fixed or variable time increments. For this purpose, the unsaturated flow problem described in the previous section was used with a minor modification corresponding to the assumption that upper and lower boundaries are horizontal yielding rectangular elements (Fig. 2.5b). The reason for this change is to subsequently allow the results obtained in these analyses to be compared with those obtained using the method of influence coefficients. The convergence criteria, initial pressure head values and boundary conditions remain identical to those described in the previous section.

A comparison of CPU times for HYDRO runs using the Runge-Kutte method and the finite difference method with fixed time increments is given in Table 2.1. Three subdivisions of the time increment were used for starting of the Runge-Kutte method. The results of the previous section indicate that the number of subdivisions could be reduced to 2, however, generally the optimum number of subdivisions would not be known a priori and the use of 3 subdivisions would be a conservative practice.

Table 2.1 Execution times in CPU seconds for time integration and element integration methods using an IBM 3084 system

Finite Difference			Runge-Kutte		
Problem*	Numerical Integration (2 x 2)	Influence Coefficient	Problem*	Numerical Integration (2 x 2)	Influence Coefficient
Δt_{fd}=25 T_{max}=400	35.7	21.6	t_{rk}=50 T_{max}=400	30.7	18.9
Δt_{fd}=25 T_{max}=800	65.6	39.7	Δt_{rk}=50 T_{max}=800	45.2	26.2
Ratio	1.83	1.83	Ratio	1.47	1.39

*

T_{max} is the maximum simulation time in hours; "Ratio" is the ratio of CPU time for T_{max} = 400 and 800 for same element and time integration methods

The results in Table 2.2 indicate that when 2 x 2 numerical integration is employed with the finite difference scheme, the execution time is CPU seconds increased by 83% when the simulation time was doubled. In comparison, the corresponding increase in CPU time for the Runge-Kutte method was only 47%. For the larger simulation duration, the total CPU time used by the Runge-Kutte method is substantially less than that required for the finite difference scheme. The main reason for this is the capability of using higher time increments with Runge-Kutte method. If the number of time interval subdivisions for the starting of the Runge-Kutte procedure was reduced from 3 to 2, CPU time would be further reduced for the Runge-Kutte method. However, for long total simulation times, the effect of the number of subdivisions on the execution cost will be small. For highly nonlinear flow problems, it will be safer to use smaller subdivisions to ensure accurate results for the first three time increments.

The foregoing discussion consider a comparison of computation efficiencies of the Runge-Kutte method and the finite difference method using fixed time increments. One advantage of the finite difference method of time integration is the ease of implementing automatic adjustment of the time increment. Commonly, a minimum and a maximum number of iterations per time increment is specified. If the actual number of iterations used falls beyond the specified range, the time increment is increased or decreased by a specified factor for the next time step. We consider here minimum and maximum iterations set to 3 and 6, respectively for a convergence accuracy of 0.01 cm. The time

Table 2.2 Execution time in CPU seconds using IBM 3084 system for Runge-Kutte and variable time-increment finite difference methods.

Finite Difference with variable time increment			Runge-Kutte		
Initial Δt_{fd} (hr)	T_{max} (hr)	CPU Time (s)	Δt_{rk} (hr)	T_{max} (hr)	CPU Time (s)
0.25	6.3	43.5	0.25	6.0	44.7
0.5	6.2	48.4	0.5	6.0	36.7
0.5	25.4	103.2	0.5	25.0	93.6
1.0	6.3	58.5	1.0	6.0	37.4
1.5	6.2	59.4	1.5	6.0	40.0
1.5	24.2	100.6	1.5	25.5	59.0

T_{max} is the maximum simulation time in hours.

step is changed by a factor of 25% if the number of iterations falls outside this range. The previously discussed flow problem is considered again, only now with the surface flux increased to 1.0 cm/hr to increase the difficulties in convergence. Element matrices are computed using the influence coefficient method. A comparison of CPU times for the problem solved using variable time increments with the finite difference method and with the Runge-Kutte method are shown in Table 2.2. For the largest time increment of 1.5 hours, 8 subdivisions were needed for convergence and the remaining time increments used 4 subdivisions with the Runge-Kutte method. The number of subdivisions used for 1.5 hour time increment case was high because the time increment within a subdivision needs to be compared to a value such that the solution using finite difference method would converge. For small simulation times in comparison to the time increment used, the results indicate that variable time increment finite difference scheme to be as attractive as the Runge-Kutte method. This true due to the reduction of the number of iterations required to converge as compared to the number of iterations required to compress a larger time increment to a smaller value for convergence. As the time increment is increased for the same simulation time, Runge-Kutte method gradually provided better computational efficiency than the finite difference method. In the next step of analysis, the simulation time was increased by fourfolds and two time increments were used in the analysis. For the case of 0.5 hour time increment, Runge-Kutte method was slightly more efficient than the finite difference method as the effectiveness of the Runge-Kutte method is not reflected at smaller

time increments. The efficiency of the Runge-Kutte method is however explicitly shown at the higher time increment of 1.5 hours where the total CPU time used was only 60% of that of the finite difference scheme. Also the total increase in CPU time with the former method for a fourfold increase in simulation time was 50% at this higher time increment. Therefore these results suggest that at higher simulation times, optimum use of the Runge-Kutte method can be obtained by using larger time steps.

Element Matrix Integration Schemes

An important objective of this paper is to evaluate the relative efficiencies of the different element matrix integration schemes. For this comparison, the modified flow domain discussed in the previous example using only linear rectangular elements was analysed using both the influence coefficient method and 2 x 2 Gaussian quadrature for element matrix computation. The applied surface flux was 0.01 cm/hr. The Runge-Kutte method with Δt_{rk} of 50 hours and 3 subdivisions for starting was used for time integration and the convergence accuracy was 0.001 cm. Pressure head variations along the initial water table are shown in Fig. 2.7 for the two element integration schemes. Agreement between the results of the two methods is good and comparable. Computational costs for the influence coefficient method was approximately 60% of that was used by the numerical integration scheme (Table 2.1). Similar gains were achieved regardless of the method of time integration used. These results indicate that average soil hydraulic properties within an element may be safely employed in computing element matrices.

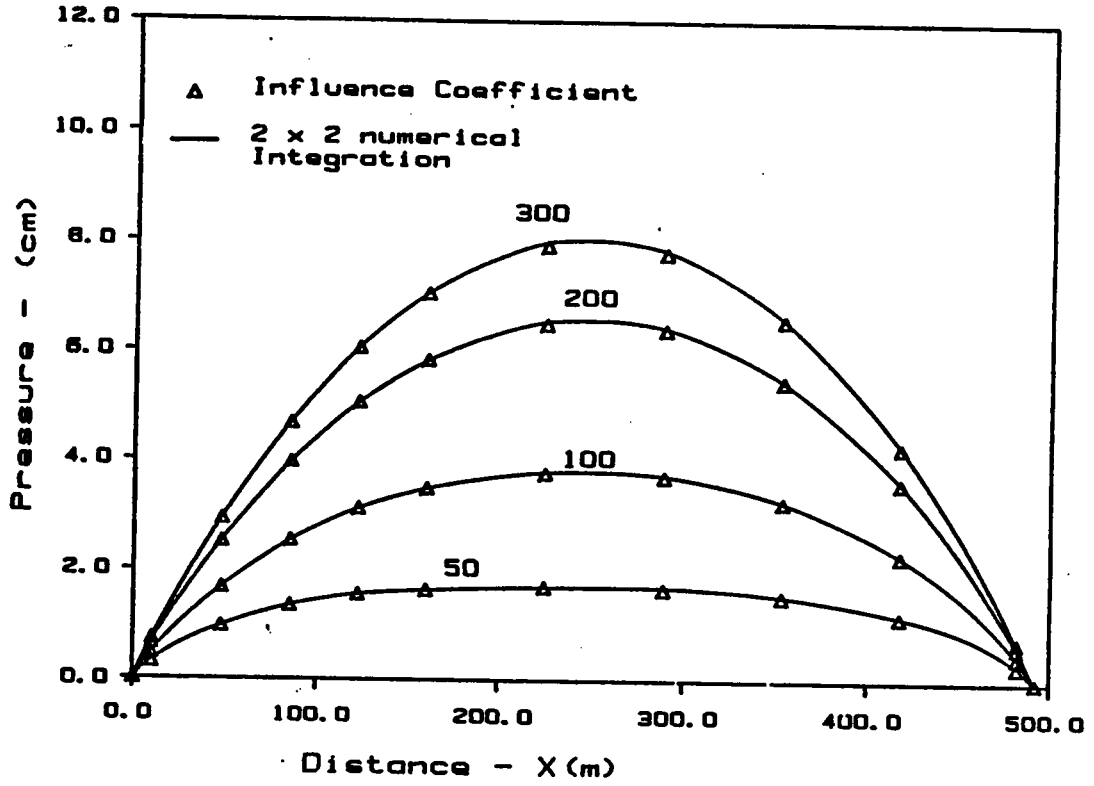

Figure 2.7 Variation of pressure head with time at the level of the original watertable for the rectangular flow domain. Numbers on curves denote time in hours.

One important reason to model fluid flow is to obtain mean velocities for subsequent analysis of solute transport. Therefore it is of great importance that flow velocities be computed accurately. To evaluate the accuracy of hydraulic fluxes predicted by the influence coefficient method, we consider again the problem presented in Table 2.2. Fluxes were computed at centroids of four elements that correspond to locations of maximum nonlinearity in soil properties (Fig. 2.5b). Element fluxes for the numerical integration scheme were computed from nodal fluxes computed from (2.17). The influence coefficient method yields centroidal fluxes directly (Eq. 2.16). Good agreement between the two methods was obtained for both vertical and horizontal components of the flux (Table 2.3). A similar analysis using a higher input flow rate close to the saturated hydraulic conductivity of the upper soil layer produced excellent agreement for the pressure and only minor absolute deviations in computed fluxes by the two element integration methods.

In the previous examples, the soil was nonhomogeneous but variations in soil hydraulic properties with depth were moderate. To evaluate the applicability of the influence coefficient method in more heterogeneous media, a case of strongly stratified soil is considered. The geometry, initial conditions and boundary conditions remain as before with the surface flux equal to 0.01 cm h^{-1} but with soil properties as shown in Fig. 2.8. Pressure head variations along the initial water table level were computed with HYDRO using both the influence coefficient method and 2 x 2 numerical integration for element matrix computation and using Runge-Kutte time integration with

Table 2.3 Computed centroidal Darcy's flux of four selected elements at a time of 300 hours.

Element	q_x-cm/hr		q_z-cm/hr	
	Numerical Integration	Influence Coefficient	Numerical Integration	Influence Coefficient
44	-0.157×10^{-1}	-0.155×10^{-1}	-0.659×10^{-2}	-0.743×10^{-2}
54	-0.259×10^{-4}	-0.305×10^{-4}	-0.704×10^{-2}	-0.751×10^{-2}
95	-0.866×10^{-2}	-0.857×10^{-2}	-0.538×10^{-2}	-0.577×10^{-2}
160	0.271×10^{-4}	0.263×10^{-4}	0.626×10^{-2}	0.709×10^{-2}

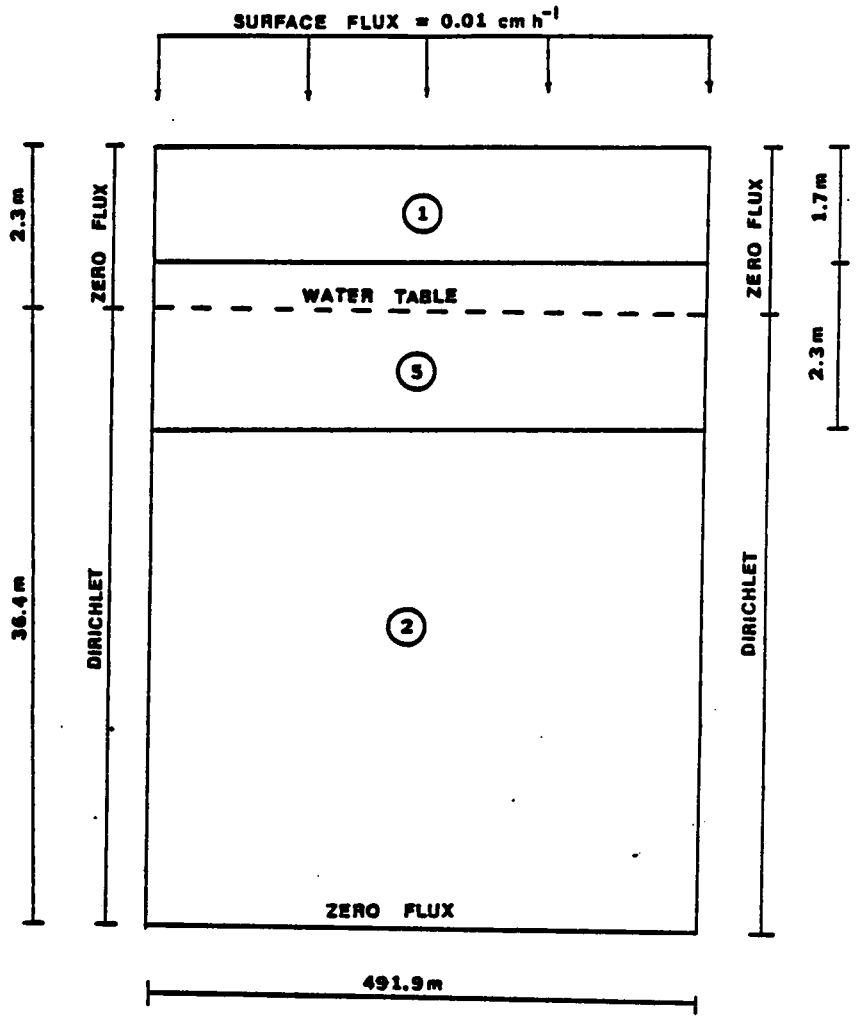

Figure 2.8 Details of the flow domain for the strongly stratified soil medium. Material numbers refer to soil properties given in Appendix C.

Δt_{rk} = 30 h having five subdivisions for the first three time increments. The results for the two methods are again in good agreement (Fig. 2.9). Variations of centroidal fluxes with time were investigated for three elements selected to represent locations of highly nonlinear soil properties. The agreement between the results of the two methods are excellent for horizontal fluxes (Fig. 2.10b), however, some discripencies occur for vertical fluxes at short simulation times (Fig. 2.10a). A possible reason for these deviations is the use of centroidal soil hydraulic properties within an element at times of rapid changes in pressure head.

The discussion of the previous sections related to the various element matrices and time integration schemes suggest that the flexibility of the computer code HYDRO can be increased by incorporating the variable time increment finite difference method to solve the flow problem within the subdivisions of the first three time increments. This procedure would automatically yield the optimum time increment of a subdivision. In specyfying the number of subdivisions, care must be taken to not use a too larger value that would cause convergence problems at subsequent predictor-corrector steps.

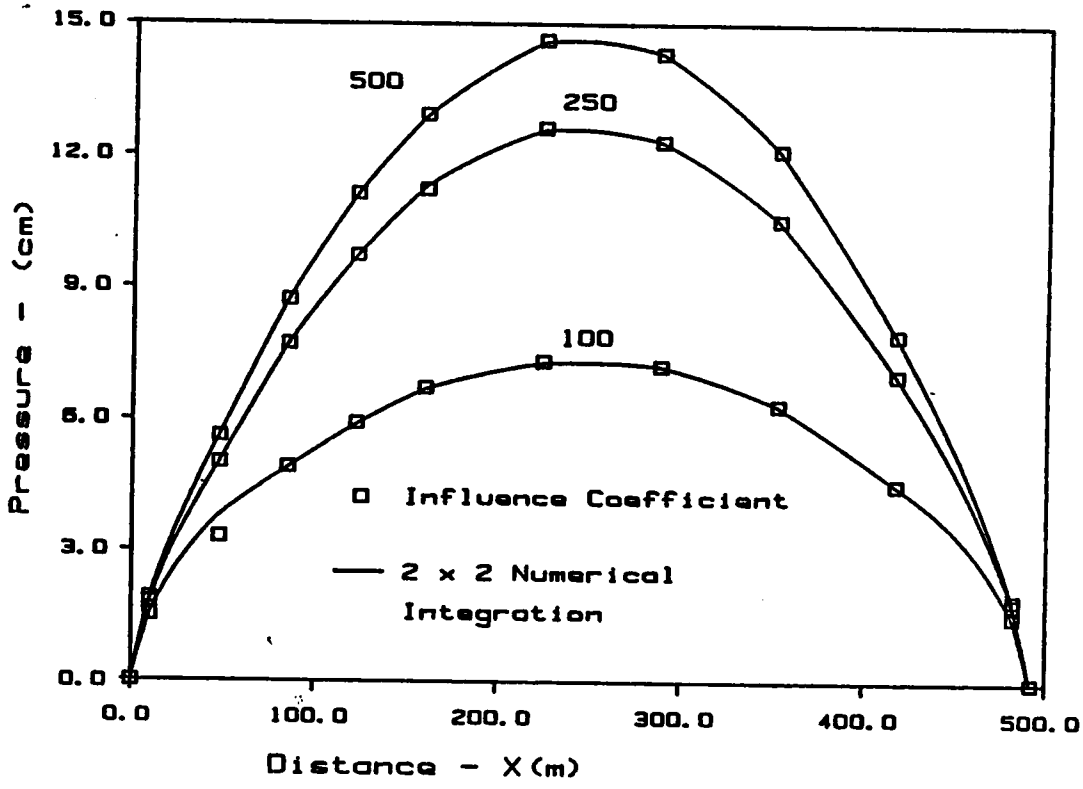

Figure 2.9 Variation of pressure head with time at the level of the original water table for the stratified soil problem. Numbers on curves denote time in hours.

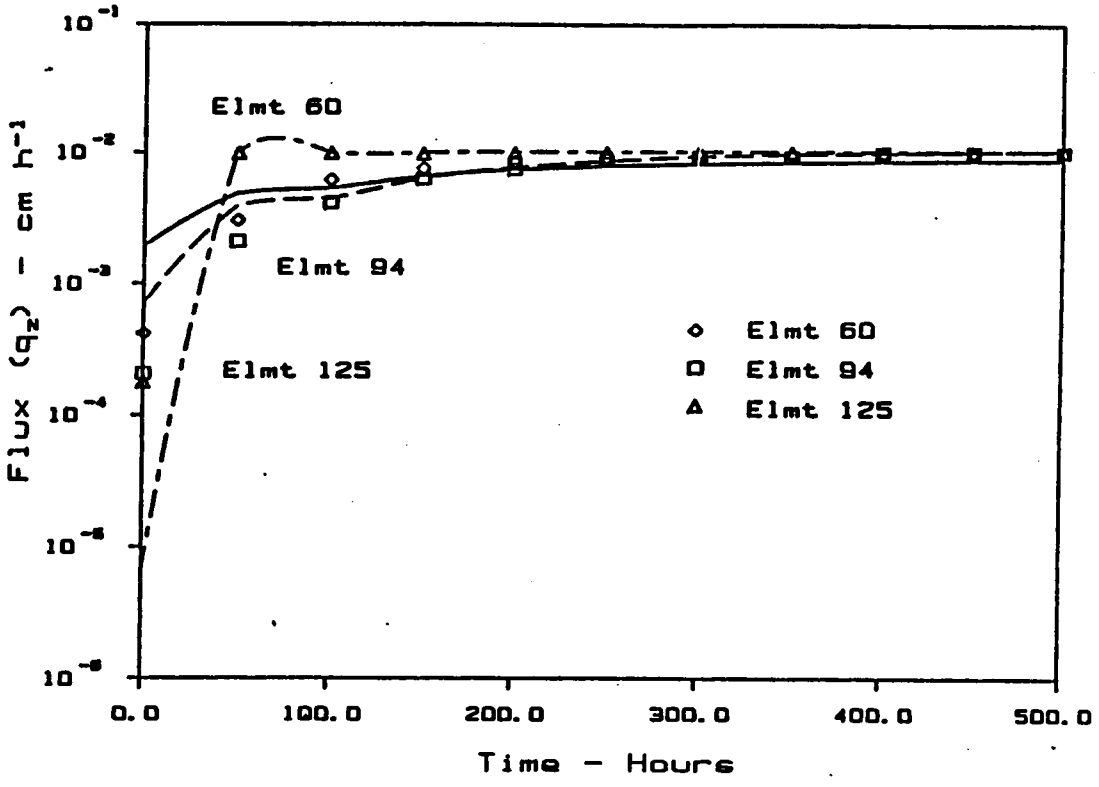

Figure 2.10a Variation of centroidal vertical flux q_z with time for three selected elements for the stratified soil problem.

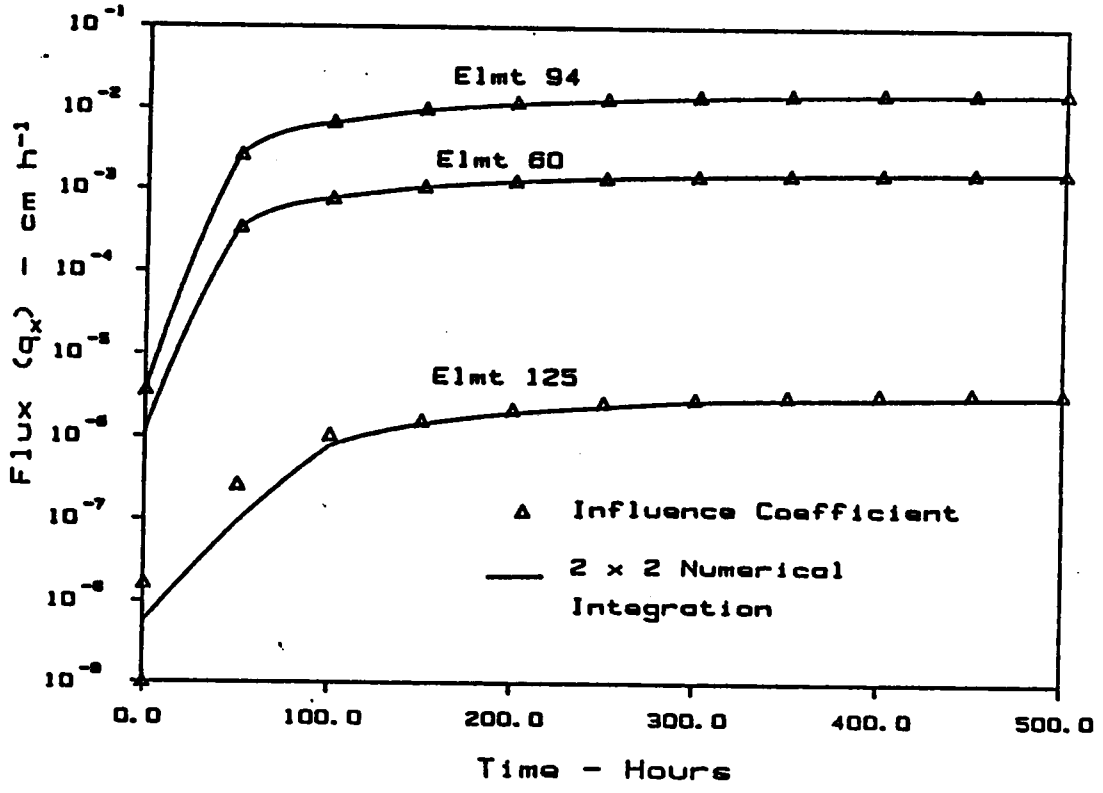

Figure 2.10b Variation of centroidal vertical flux q_x with time for three selected elements for the stratified soil problem.

CONCLUSIONS

From the results presented in the previous sections, the following conclusions can be drawn.

1) The finite element method incorporating a suitable time marching scheme can be effectively used to analyze flow in a partially saturated medium with various boundary conditions and point sources. Use of a predictor-corrector method with fourth order Runge-Kutte approximations to handle time integration allows the use of higher time increments than when time derivatives are approximated by finite differences. The Runge-Kutte approach can be successfully applied by incorporating a suitable extrapolation technique to estimate the value of the variable at any node for the next time increment. In all cases studied, convergence occurred within 3 to 4 iterations with an accuracy of 0.001 cm.

2. The minimum number of subdivisions required for the first three time increments of the Runge-Kutte method will depend on the size of the Runge-Kutte time step as well as on the nature of the problem concerned. In the analysis of soils with highly nonlinear soil properties or heterogenity or boundaries involving rapid changes in pressure head values, it is desirable to increase the number of subdivision than decreasing the time increment for overall computation efficiency. In general it is preferable to use between 3 to 5 subdivisions for most field problems and this value can be increased if necessary for soils with highly nonhomogeneous and nonlinear soil properties or if higher time increments are

desired.

3. The minimum number of subdivisions required for the first three time increments of the Runge-Kutte method will depend on the size of the Runge-Kutte time step as well as on the nature of the problem. In the analysis of soils with highly nonlinear soil properties or with boundaries involving rapid changes in pressure head, it is desirable to increase the number of subdivisions rather than decrease the Runge-Kutte time increment to obtain best overall computational efficiency for relatively long simulation times. In general it has been found that 3-5 subdivisions are appropriate for most problems. This value may need to be increased for soils with highly nonhomogeneous and nonlinear soil properties or if higher time increments are desired.

4. The method of influence coefficients produced heads that agreed closely with those obtained using numerical integration. Rates of convergence and solution accuracy produced by this method were good for heterogeneous soil profiles with highly nonlinear soil properties. The use of centroidal soil properties in computing element matrices gave dependable results and reduced computational costs. The only limitation of the influence coefficient method is that the geometry of the domain must be discretized using only linear rectangular or triangular elements.

5. Hydraulic fluxes computed by the method of influence coefficients generally compared well with those computed by numerical integration although some deviations were observed under highly nonlinear conditions perhaps owing to the use of average element

properties. For subsequent analysis of the movement of chemical wastes, fluxes could be computed with less effort by computing the total potential field directly.

6. The average total CPU time required with the influence coefficient method was approximately 60% of that for 2 x 2 Gaussian integration. Therefore, the method of influence coefficients provides an attractive method of increasing the computational efficiency of finite element solutions of highly nonlinear flow problems while maintaining solution accuracy.

REFERENCES

Carnahan, B., H. A. Luther and J. O. Wilkes. 1969. Applied Numerical Methods. John Wiley and Sons, New York, 604 pp.

Cleary, R. W. and M. J. Ungs. 1977. Analytical models for groundwater pollution and hydrology. Rep. 78-WR-15, Dept. of Civil Eng., Princeton University, Princeton, New Jersey, 166 pp.

Cooley, R. L. 1971. A finite difference method for unsteady flow is variably saturated porous media: Applications to a single pumping well, Water Resour. Res. 7:1607-1625.

Davis, L. A. and S. P. Neuman. 1983. Documentation and User's Guide: UNSAT2-Variably Saturated Flow Model - NUREG/CR-3390, U.S. Nuclear Regulatory Commission, Washington, DC..

Guymon, G. L., V. H. Scott and L. R. Herrmann. 1970. A general numerical solution of the two-dimensional diffusion-convection equation by the finite element method. Water Resour. Res. 6:1611-1617.

Huyakorn, P.S. and G. F. Pinder. 1983. Computational Methods in Subsurface Flow. Academic Press, New York, 473 pp.

Huyakorn, P. S., D. Thomas and B. M. Thompson. 1984. Techniques for making finite elements competitive in modeling flows in variably saturated porous media. Water Resour. Res. 20:1099-1115.

Neuman, S. P. 1973. Saturated-unsaturated seepage by finite elements. Proc. ASCE, J. Hydraul. Div., (HY12) 99:2233-2250.

Segerlind, L. J. 1984. Applied Finite Element Analysis, John Wiley and Sons, New York., 411 pp.

Wagner, J., C. E. Ruiz-Calzada, C. G. Enfield, T. Phan and D. G. Kent. 1980. Computer Models for Two Dimensional Subterranean Flows and Pollutant Transport. U.S. Environmental Protection Agency Rep., Rep., No. CR-806931.

Yeh, G. T. and D. S. Ward. 1980. FEMWATER: A Finite Element Model of Water Flow Through Saturated-Unsaturated Porous Media. ORNL-5567, Oak Ridge Nat. Laboratory, Oak Ridge, Tennessee., 149 pp.

CHAPTER III

EFFECTS OF HYSTERESIS WITH AIR ENTRAPMENT ON WATER FLOW

ABSTRACT

Effects of hysteresis with air entrapment on water content and head distributions, surface fluxes and water balance components are investigated by finite element simulations of flow in one- and two-dimensional spatial domains. Results of one-dimensional analyses indicate that effects of hysteresis are markedly influenced by surface boundary conditions and to a lesser extent by initial conditions. Stipulation of flux-controlled boundary conditions results in minimal hysteretic effects, while potential-type boundary conditions produce substantial deviations between hysteretic and nonhysteretic simulations. The latter effects are attributable in large part to differences in surface conductivity associated with air entrapment. Predicted water content distributions for nonhysteretic simulations using main drying functions deviated much more from hysteretic model results than nonhysteretic simulations based on main wetting functions. For two-dimensional problems, predicted infiltration, evaporation and seepage fluxes and soil water storage changes were much higher for nonhysteretic simulations using main drying functions than for hysteretic simulations; predictions based on main wetting functions deviated less markedly from hysteretic simulations. Introduction of heterogeneity in the porous medium diminished effects of hysteresis on infiltration and seepage, but accentuated differences in evaporation due

to interactions between evaporation and seepage boundaries suggesting that the influence of heterogeneity on hysteretic effects will be problem-specific.

INTRODUCTION

Hysteresis in soil hydraulic properties is commonly neglected in analyses of water movement in the unsaturated zone. To a large extent this is motivated by expediency since hysteretic models are computationally more involved than nonhysteretic models and require information which is often not readily available. Unanimity does not exist concerning the significance of hysteresis on field scale flow and transport predictions. While a number of studies have demonstrated substantial errors may be incurred by ignoring hysteresis (Rubin, 1967; Royer and Vachaud, 1975; Beese and van der Ploeg, 1976; Stauffer and Dracos, 1984), others have found effects to be rather small (Pickens and Gillham, 1980). It is sometimes suggested that effects of spatial variability of soil hydraulic properties may overwhelm local hysteretic effects; however, it has been shown that such variability will itself induce apparent hysteretic effects at larger spatial averaging scales (Montaglou and Gelhar, 1985) indicating that the magnitude of hysteretic effects will depend on the implied scale of averaging for a particular problem.

A number of models for describing the hysteretic relationship between water content (θ) and pressure head (h) have been developed. These include theoretical models of pore-scale hysteresis based on the

domain theory of capillary hysteresis (Topp, 1971; Mualem, 1974, 1984) and a variety of empirical models (Gillham et al., 1976; Killough, 1976; Hoa et al., 1977; Scott et al., 1983). Calibration, in both instances, generally requires knowledge of one primary wetting branch and one primary draining branch of $\theta(h)$. A substantial constraint on the general applicability of most hysteresis models is the assumption that $\theta(h)$ exhibits closure at $h=0$, indicating residual air entrapment to be either nonexistant or independent of saturation history. In field soils, variations in air entrapment are expected which have been shown to substantially affect water flow (Stauffer and Dracos, 1984; Fayer and Hillel, 1986a, 1986b).

Numerical models capable of solving complex variably saturated flow problems have been well documented in literature (e.g., Neuman, 1973; Huyakorn et al., 1984; Kaluarachchi and Parker, 1987). Analyses of hysteretic flow for one-dimensional (Rubin, 1967; Staple, 1969; Dane and Wierenga, 1975; Milly, 1982; Curtis and Watson; 1984) and two-dimensional problems (Perrens and Watson, 1977; Hoa et al., 1977; Pickens and Gillham, 1980; Stauffer and Dracos, 1984; Fayer and Hillel, 1986b) have identified various facets of the effects of hysteresis for specific conditions. However, no systematic analyses of the effects of varying boundary and initial conditions or flow domain geometry and material heterogeneity have been reported, and except for specific case studies by Stauffer and Dracos (1984) and Fayer and Hillel (1986b), effects of air entrapment have not been considered. In this paper, we present results of such analyses with the purpose of evaluating effects of hysteresis with air entrapment on water movement for situations of

sufficient complexity to allow inference to realistic field problems.

MODEL DESCRIPTION

Hydraulic properties

We will employ the model of Kool and Parker (1987) to describe hysteretic soil hydraulic properties. This model uses an empirical scheme to describe the hysteretic pressure-saturation, $\theta(h)$, functional including entrapped air effects, and predicts the assumed nonhysteretic hydraulic conductivity function $K(\theta)$ from the $\theta(h)$ relations. The principal advantage of the model is its parametric simplicity, which substantially lightens the burden of calibration and facilitates its implementation with minimal effort. Guidelines for parameter evaluation have been given by Kool and Parker (1987) and Kool et al. (1986). Only the essential features of the model will be outlined here.

Main drainage and wetting branches of the $\theta(h)$ functional are described by van Genuchten's (1980) equation written as:

$$\theta^d(h) = \begin{cases} \theta_r + (\theta_s{}^d - \theta_r)[1+|\alpha^d h|^n]^{-m} & h < 0 \\ \theta_s{}^d & h \geq 0 \end{cases} \qquad (3.1a)$$

$$\theta^w(h) = \begin{cases} \theta_r + (\theta_s{}^w - \theta_r)[1+|\alpha^w h|^n]^{-m} & h < 0 \\ \theta_s{}^w & h \geq 0 \end{cases} \qquad (3.1b)$$

where $\theta_s{}^d$ and $\theta_s{}^w$ are satiated water contents for the main drying curve, $\theta^d(h)$, and main wetting curve, $\theta^w(h)$, respectively, θ_r is the residual water content, α^d and α^w are path-dependent parameters, n is

a parameter assumed independent of saturation path (see Kool and Parker, 1987), and m=1-1/n. The difference $\theta_s^d - \theta_s^w$ represents the maximum residual entrapped air content.

Drainage scanning $\theta(h)$ curves are predicted by rescaling $\theta^d(h)$ to pass through θ_r and the last wetting-to-drying reversal point $(\theta_\Delta, h_\Delta)$ by replacing θ_s^d in (3.1a) by:

$$\theta_u^d = \frac{\theta_\Delta [\theta_s^d - \theta_r] - \theta_r [\theta_s^d - \theta^d(h_\Delta)]}{\theta^d(h_\Delta) - \theta_r} \tag{3.2}$$

Imbibition scanning curves are predicted by replacing θ_r and θ_s^w in (3.1b) by θ_ℓ and θ_u^w, respectively, defined by

$$\theta_\ell = \frac{\theta_\Delta[\theta_s^w - \theta_r] - \theta_u^w [\theta^w(h_\Delta) - \theta_r]}{\theta_s^w - \theta^w(h_\Delta)} \tag{3.3}$$

$$\theta_u^w = \theta_s^d - \theta_{ar} \tag{3.4}$$

where $(\theta_\Delta, h_\Delta)$ is now the last drying-to-wetting reversal point, and θ_{ar} is the residual entrapped air content (i.e., entrapped air at h=0 on the wetting scanning curve) estimated by:

$$\theta_{ar} = \left[\frac{1}{\theta_s^d - \theta_\Delta} + \frac{1}{\theta_s^d - \theta_s^w} + \frac{1}{\theta_s^d - \theta_r} \right]^{-1} \tag{3.5}$$

Note that θ_{ar} depends on saturation history through θ_Δ. Specifically, as the water content at initiation of wetting (i.e., θ_Δ) diminishes, residual entrapped air increases such that $\theta_u \to \theta_s^w$ as $\theta_\Delta \to \theta_r$ where θ_u is the satiated water content. As a result, if the soil has been recently subjected to marked drying, scanning hysteresis loops will be nearly

closed in the vicinity of θ_s^w, while for less dry prior conditions, higher satiated water contents, $\theta_u > \theta_s^w$, will occur.

The foregoing $\theta(h)$ model is attractive by virtue of its computational simplicity and the necessity of only storing the most recent reversal point. The cost of not imposing closure of scanning loops is that a "pumping" phenomenon will arise if cyclic boundary conditions occur (Jaynes, 1985). Alternative $\theta(h)$ models may be employed to avoid such problems (e.g., Hanks et al., 1969; Mualem, 1974, 1984; Parker and Lenhard, 1987). However, in the present study we will confine our attention to problems involving a small number of reversals for which the proposed model will suffice.

To describe components of the hydraulic conductivity tensor, K_{ij}, we assume that $K_{ij} = k_r K_{sij}$ where k_r is the relative permeability and K_{sij} is the ij saturated conductivity defined as the value at $\theta=\theta_s^d$. We assume k_r to be nonhysteretic and given by:

$$k_r = S_e^{1/2} \left[1 - (1-S_e^{1/m})^m \right]^2 \tag{3.6a}$$

$$S_e = (\theta-\theta_r)/(\theta_s^d-\theta_r) \tag{3.6b}$$

where S_e is the effective saturation.

Variably-saturated flow

Water flow in an isothermal, incompressible, variably saturated porous medium in two dimensions will be described by Richard's equation assuming pressure gradients in the continuous air phase to be negligible. The form we employ is

$$C(h)\,\frac{\partial h}{\partial t} = \frac{\partial}{\partial x}\left[K_x(h)\,\frac{\partial \Phi}{\partial x}\right] + \frac{\partial}{\partial z}\left[K_z(h)\,\frac{\partial \Phi}{\partial z}\right] \qquad (3.7)$$

where h is the pressure head, Φ=h+z is the total hydraulic head, K_x and K_z are components of the conductivity tensor along the assumed principal directions x and z with z the vertical coordinate measured positive upwards, $C = \partial\theta/\partial h$ is the specific water capacity, and t is time. Initial and boundary conditions for (3.7) are

$$h(x,z,t) = h_o(x,z) \qquad \text{for } t = 0 \text{ in } S \qquad (3.8a)$$

$$\theta(x,z,t) = \theta_o(x,z) \qquad \text{for } t = 0 \text{ in } S \qquad (3.8b)$$

$$h(x,z,t) = h_1(x,z,t) \qquad \text{for } t > 0 \text{ on } \Gamma_1 \qquad (3.8c)$$

$$-\left[K_x\,\frac{\partial \Phi}{\partial x} + K_z\,\frac{\partial \Phi}{\partial z}\right]\cdot \bar{n} = q_n(t) \qquad \text{for } t > 0 \text{ on } \Gamma_2 \qquad (3.8d)$$

where S denotes the entire flow domain and Γ_1 and Γ_2 are portions of the boundary. Equations (3.8a) and (3.8b) describe the initial condition in terms of pressure h_o and water content θ_o both of which must be stipulated owing to the nonuniqueness of $\theta(h)$. Equations (3.8c) and (3.8d) describe Dirichlet or potential-type boundary conditions on Γ_1 and Neumann or flux-type boundary conditions on Γ_2 where $\bar{n}$ is the unit normal outward vector and q_n is the magnitude of the normal flux across the boundary.

In addition to the boundary conditions described by (3.8c) and (3.8d) with h_1 and q_n known functions of time, conditions are often encountered in flow problems in which h_1 and q_n are time-dependent

functions of flow. Specifically, atmospheric boundary conditions may occur on boundary segments in contact with the atmosphere on which $|q_n|$ is maximized subject to the constraint that $h_{min} < h < 0$. On potential seepage boundaries, the additional constraint is imposed that if a point on the potential seepage face occurs at which q_n changes sign, h=0 at all nodes along the face with elevations lower than this point. The length of the seepage boundary is time-dependent and requires a suitable iterative procedure to be evaluated. The finite element program HYDRO decribed in chapter II (Kaluarachchi and Parker, 1987), with modifications to accomodate atmospheric and seepage boundary conditions and to implement the hydraulic property model described in the preceding section, was used for the analyses reported in this paper. Numerical accuracy of the code was verified for a number of the simulations by performing mass balance checks which indicated mass balance errors within 5 percent in all cases.

NUMERICAL SIMULATIONS

Flow simulations were conducted for a number of hypothetical scenarios with various initial and boundary conditions in one- and two-dimensional homogeneous and nonhomogeneous domains. Each scenario was analysed using three procedures to define the constitutive relationships: (1) hysteretic $\theta(h)$ as described in the preceding section, (2) nonhysteretic $\theta(h)$ corresponding to the main wetting curve, and (3) nonhysteretic $\theta(h)$ corresponding to the main drying curve. For brevity, these simulations will be referred to as H,

NW and ND cases, respectively. One-dimensional problems will be used to identify critical factors associated with the initial and surface boundary conditions to be investigated further in two-dimensional flow domains.

Hydraulic properties of the hypothetical materials employed in the simulations (Table 3.1) are illustrated in Fig. 3.1. Note that both soil materials have nonclosed main hysteresis branches indicative of air entrapment (Fig. 3.1a). Most simulations will involve homogeneous Soil 1. Soil 2 was selected to represent a material with lower conductivity than Soil 1 for use in nonhomogeneous two-dimensional simulations. Hydraulic conductivities were assumed to be isotropic ($K_S=K_{SX}=K_{SZ}$) with K_S of Soil 1 taken 20 times greater than that of Soil 2. Identical nonhysteretic $k_r(\theta)$ functions (Eq. 3.6) were employed for all three simulation procedures.

It may be noted that the ND and NW cases bracket the extremes of nonhysteretic $\theta(h)$ curves which may be experimentally determined. The most common calibration procedure for $\theta(h)$ is to use laboratory equilibrium drainage measurments. In principle, one may obtain $\theta^d(h)$ from such measurements if care is taken to achieve complete saturation. In practice, a drying scanning curve will normally be measured for which $\theta_u<\theta_s^d$. Similarly for imbibition measurements, wetting scanning curves with $\theta_s^w<\theta_u<\theta_s^d$ will normally be obtained. In the case of field measurements under ambient atmospheric conditions, single-valued functions may be fit through data which comprise a complex sequence of scanning paths bounded by $\theta^w(h)$ and $\theta^d(h)$.

Table 3.1 Parameters of van Genuchten's model describing soil hydraulic properties used in simulations.

Soil	α^d (cm^{-1})	α^w (cm^{-1})	n	θ_r	θ_s^d	θ_s^w	K_s ($cm\ h^{-1}$)
1	0.028	0.040	3.0	0.12	0.50	0.40	2.0
2	0.029	0.042	2.9	0.15	0.49	0.42	0.1

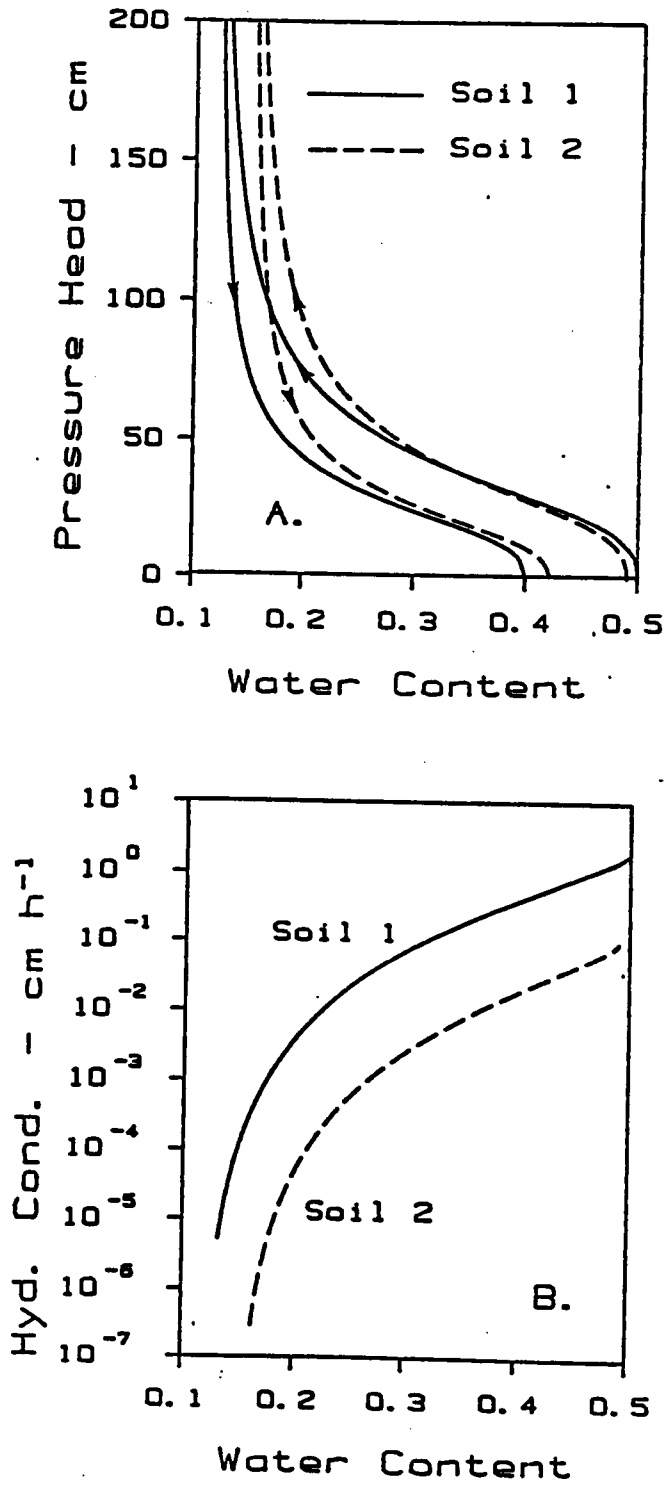

Figure 3.1 Hydraulic properties of soils used in simulations.

Example 1: One-dimensional flux infiltration with uniform initial conditions.

The objective of the first two examples is to evaluate the effects of hysteresis on infiltration as influenced by surface boundary conditions. The total domain is taken to be a 100 cm long vertical column of Soil 1 with a zero-flux lower boundary and with initial conditions corresponding to a constant moisture content of 0.2. For the NW simulation, the initial head corresponds to $\theta^w(h)$, and for ND and H simulations $\theta^d(h)$ was employed. The respective initial pressure heads were -44 cm for NW and -75 cm for ND and H simulations.

The upper boundary condition in the present example involved constant flux infiltration with q_n = 0.3 cm h^{-1} which is 15% of the saturated conductivity of the soil and is also lower than $K(\theta_s^w)$ which will be the maximum K for the NW case. The computed water content distributions for simulation times up to 17.8 h are shown in Fig. 3.2 for H, NW and ND cases. At the final simulation time, the surface water content for all cases has reached an asymptotic value of 0.374 corresponding to the θ at which $q_n = K(\theta)$. Likewise, due to the uniqueness of $K(\theta)$, flux-control of the upper boundary, and constancy of initial water content, the $\theta(z,t)$ distributions show only small variations among the H, NW and ND cases. Variations in $h(z,t)$ between the different cases will be much greater, reflecting the various $\theta(h)$ relations for each. For example, at the soil surface at t=17.8 h, pressure heads for the three cases were -16.1, -13.3 and -33.3 cm for H, NW and ND simulations, respectively.

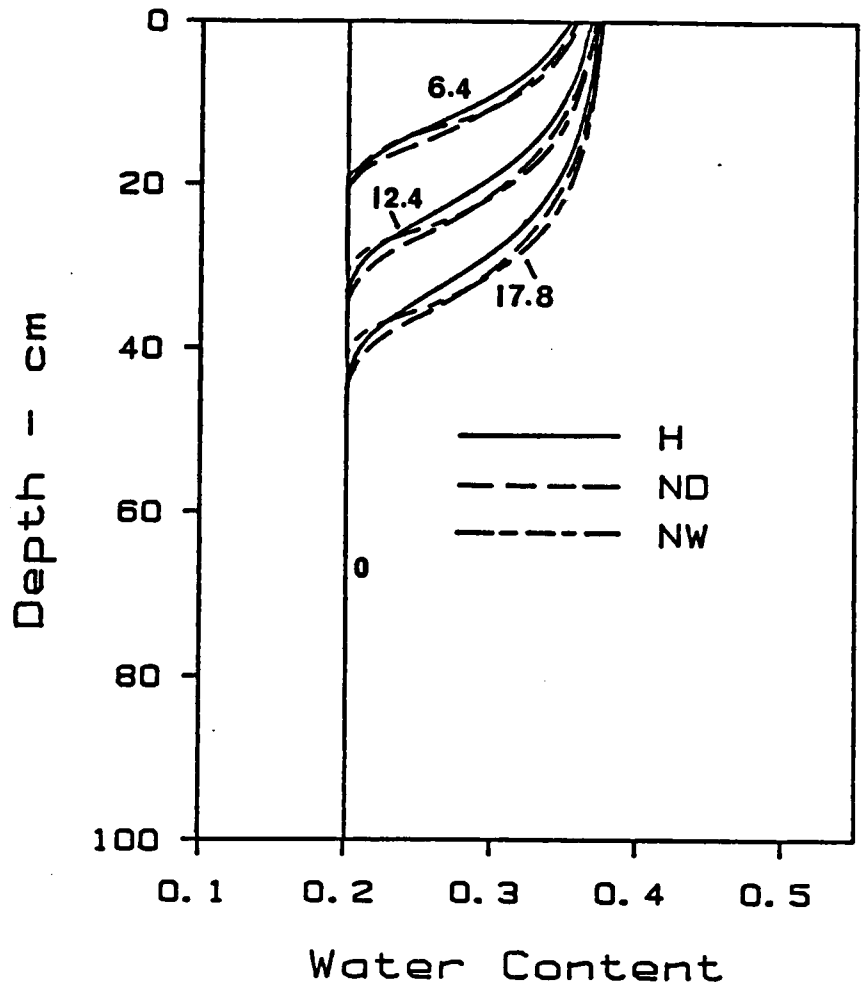

Figure 3.2 Water content distributions during infiltration for Example 1. Numbers on curves denote time in hours.

Results of this example indicate that $\theta(h)$ hysteresis will have little effect on water content distributions when the surface boundary is flux-controlled and initial water content is uniform. We caution that imposing uniform initial pressure head distributions is not expected to lead to similar conclusions (Hopmans and Dane, 1986) since this would result in different initial water content distributions depending on the assumed $\theta(h)$ relationship and the saturation history. In particular, initial water content and hence rate of wetting front advance would be greater for ND than NW simulations. Hysteretic simulations would lie intermediate depending on the assumed history.

Example 2: One-dimensional ponded infiltration with uniform initial conditions.

In this example we repeat the analysis of Example 1 but with the upper boundary condition now specified as a fixed-potential type with h=0. The computed water content distributions up to t = 6 h for H, NW and ND simulations are shown in Fig. 3.3. Note that at h = 0 the satiated water contents are θ_s^w = 0.400 for the NW case, θ_s^d = 0.500 for the ND case, and θ_u = 0.405 for the H simulation. Note that only one scanning curve is involved for the H simulation because of the assumed uniform initial condition and that the small difference between θ_u and θ_s^w is due to the relatively dry initial condition. Due to the imposed boundary conditions, surface water contents are controlled at their respective satiated values. Surface fluxes are in turn controlled by the value of $K(\theta)$ corresponding to the surface water content. For the present material properties and initial conditions, ratios of

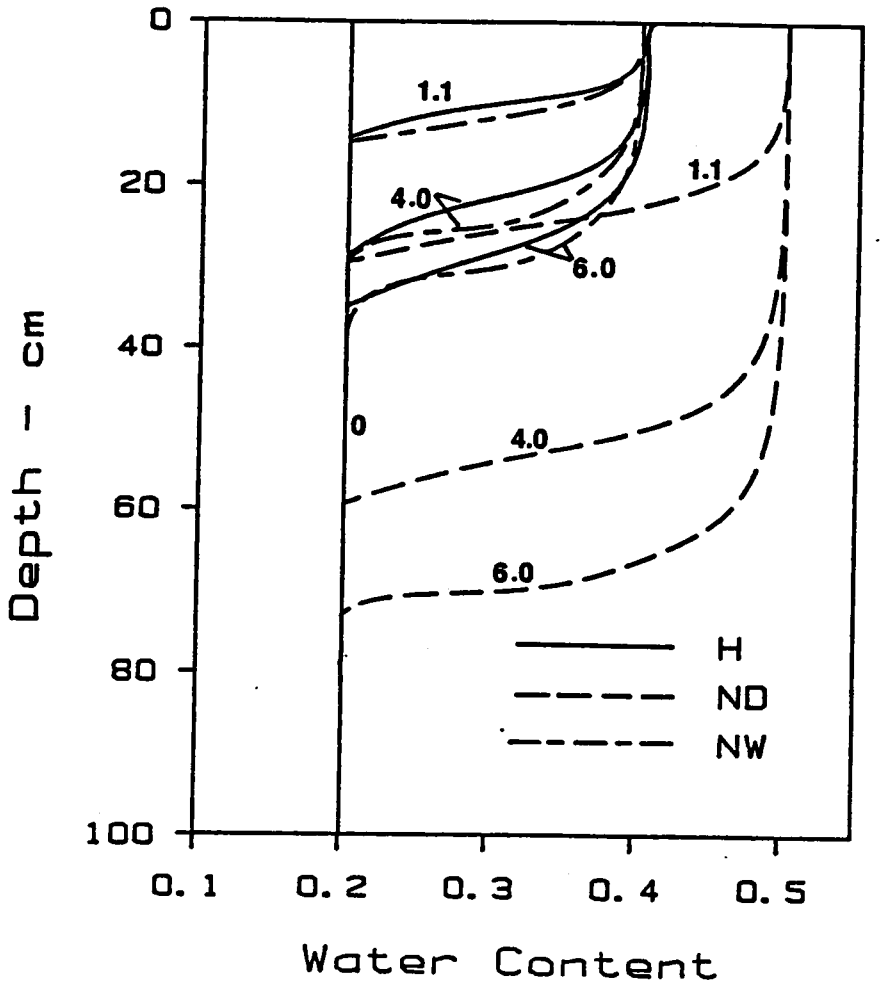

Figure 3.3 Water content distributions during infiltration for Example 2. Numbers on curves denote time in hours.

$K(\theta_s{}^w):K(\theta_u):K(\theta_s{}^d)$ are 1.0:1.08:4.92 and quasi-steady state infiltration rates for NW, H and ND simulations will eventually approach these proportions. At shorter times, differences in the C(h) functions appear to ameleorate the effects of large surface K differences. Over the duration of the simulation, cumulative infiltration for the NW simulation was 1.01 times that of the H simulation while the ND case was 3.35 times greater.

For the fixed-potential boundary condition, differences between NW and ND simulations are clearly substantial. For the initial conditions of this example, H simulations closely follow the NW case. However, since it is presumed that air entrapment diminishes as the initial condition becomes wetter, H simulations may be expected to gradually approach the ND case as the initial uniform water content is increased.

Example 3: One-dimensional infiltration and evaporation with nonuniform initial conditions.

The results of the two previous examples showed the effects of hysteresis on infiltration with uniform initial conditions and constant-head or constant-flux surface boundary conditions. We turn now to consideration of the effects of hysteresis for nonuniform initial conditions and time-varying boundary conditions. For this purpose, the identical flow domain as in the previous examples was employed with equilibrium initial conditions, zero-flux lower boundary and atmospheric-type upper boundary conditions corresponding to rainfall for a period $0 < t \leq t_1$ followed by potential evaporation for $t_1 < t \leq t_2$. We discuss simulation results for the infiltration and evaporation intervals

in turn.

Infiltration

Initial conditions for the simulations were assumed to correspond to hydrostatic equilibrium with the lower boundary at zero pressure. Accordingly, initial pressure distributions varied linearly from zero at the lower boundary to -100 cm at the soil surface. The initial water content distribution for hysteretic simulations was assumed to correspond to the main drying $\theta(h)$ curve. A rainfall rate of 4.0 cm h^{-1} was applied for a duration t_1 = 5.9 h. Since this rainfall rate is twice as great as K_S for the soil, surface ponding (h=0) occurs after a relatively short period for all simulations.

Computed water content distributions for H, NW and ND simulations are shown in Fig. 3.4. Comparison of H and NW simulations (Fig. 3.4a) indicates fairly close correspondence at early times, but progressively greater discrepancies as time procedes. The correspondence at early times reflects the similarity of ponded water contents at the surface which in turn controls the surface flux to a large extent. At longer times the effects of variable initial water content distributions increasingly dominate the simulations. The dominant influence of initial conditions in these simulations is attributable to differences in the amount of water needed to fill the unsaturated pore volume between initial and satiated water contents which increase with depth resulting in more rapid advance of the wetting front for H simulations compared to the NW case. A second factor which will influence the results is the fact that, in contrast to Examples 1 and 2, different scanning curves with gradually decreasing entrapped air contents are followed at

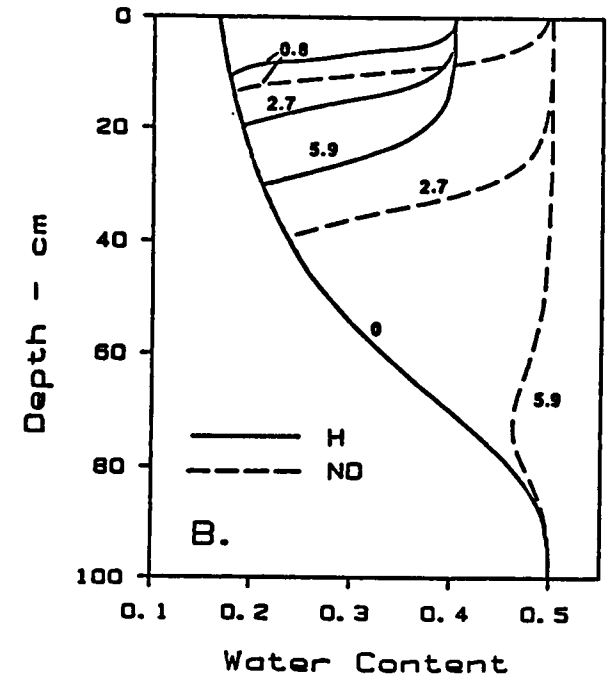

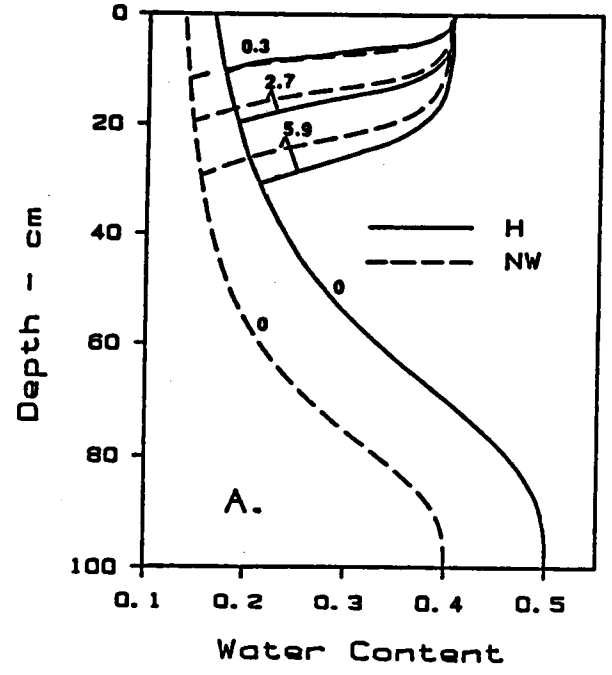

Figure 3.4 Water content distributions during infiltration for Example 3. Numbers on curves denote time in hours.

progressively greater depths. For the specific initial conditions and duration of rainfall, differences in scanning curves were rather small, however, for longer infiltration times or different initial conditions, this behavior may have a much greater effect. Over the duration of the application period, cumulative infiltration for the NW case was 1.07 times that for the H simulation.

Large deviations occur between H and ND simulations (Fig. 3.4b) due in large measure to the higher water content at the ponded surface for the ND case and correspondingly greater conductivity and surface flux. Due to the increase in initial water content with depth, the rate of wetting front advance accelerates with time resulting in an increasing disparity between H and ND simulations as time procedes. Cumulative infiltration for the ND case was 3.0 times greater than for the H simulation.

Evaporation

Immediately following the infiltration stage, a potential evaporation surface condition was imposed for a duration $(t_2 - t_1) = 120$ h. The surface flux was maintained at the potential evaporation rate of 0.02 cm h^{-1} until pressure head at the surface reached -900 cm, after which a constant head condition was imposed. The switch to Neumann-type boundary condition at h=-900 cm was imposed to avoid numerical difficulties associated with the asymptotic approach of h to $-\infty$ as $\theta \rightarrow \theta_r$. Note that $\theta \approx \theta_r$ at h=-900 cm (Fig. 3.1a). Computed water content profiles during the evaporation stage are shown in Fig. 3.5. Within the zone wetted during infiltration, water content distributions for H and NW simulations exhibit moderate deviations during the evaporation

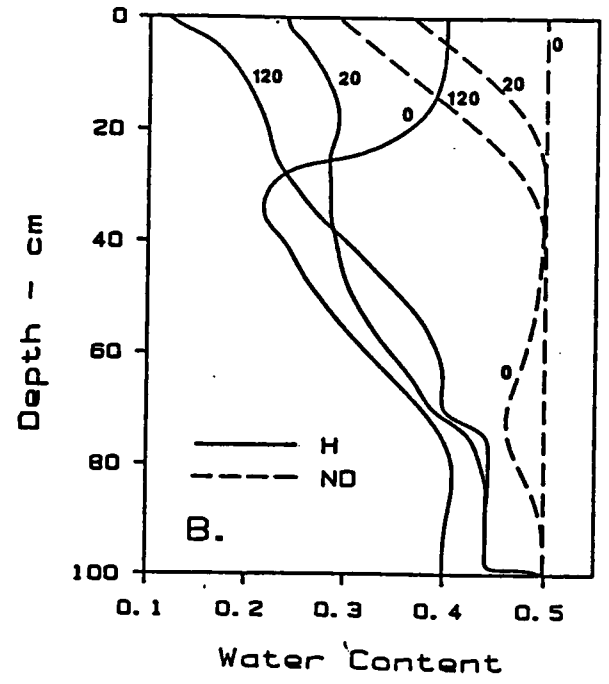

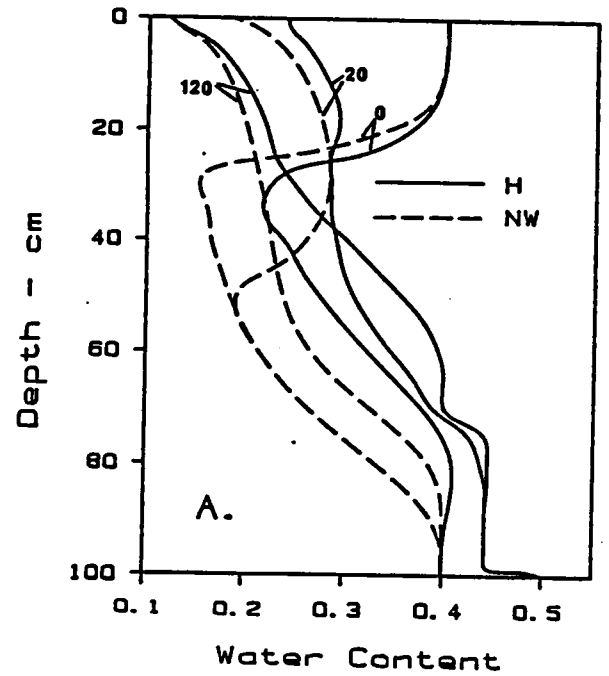

Figure 3.5 Water content distributions during evaporation for Example 3. Numbers on curves denote time since begining of evaporation ($t-t_i$) in hours.

period (Fig. 3.5a). At greater depths, devations become larger reflecting different initial distributions preceding infiltration and as well as different redistribution behavior. Cumulative evaporation predicted for the NW simulation over the 120 h period was 1.2 times greater than that for the H simulation due to more rapid redistribution of infiltrated water in the latter case.

Water distributions for the ND case during the evaporation period bear virtually no similarity to those of the H simulation, due in large part to the large differences in water contents at the end of the infiltration period (Fig. 3.5b). Because of the greater total amount of water in the profile for the ND case, constant-flux evaporation continues for a longer time before the Neumann boundary condition occurs and evaporation rate diminishes. As a result, cumulative evaporation for the ND case is predicted to be 2.0 times greater than for the corresponding H simulation.

Example 4: Infiltration, evaporation and seepage in a two-dimensional, homogeneous soil domain

The flow domain for this problem is taken to be a 1.6 m thick, 10 m long bed with a 1:25 slope on lower and upper surfaces except at the toe where a 1:1.64 slope impinges on the point of lowest elevation as illustrated in Fig. 3.6. Zones 1 and 2 are both assumed to have properties of Soil 1 used in previous simulations (Table 3.1). Boundary segments BA and AD are taken as zero-flux boundaries while DC and CB are potential seepage faces subjected to atmospheric conditions involving a period of rainfall ($0 < t \leq t_1$) followed by evaporation ($t_1 < t \leq t_2$).

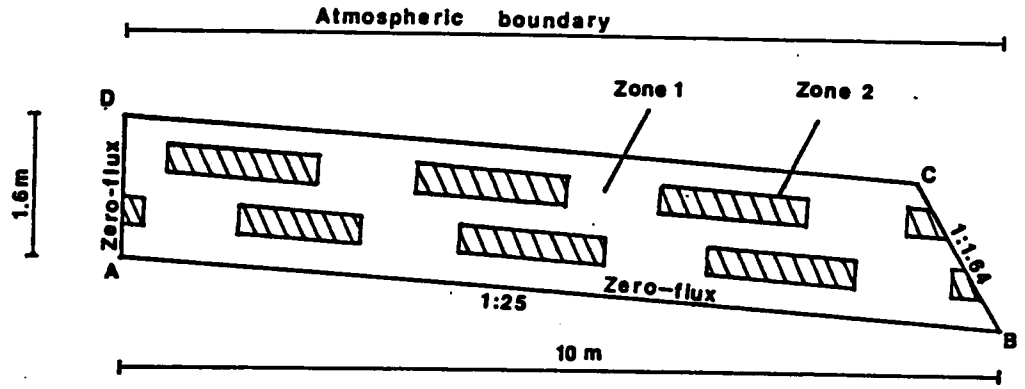

Figure 3.6 Flow domain for the two-dimensional simulations.

Example 4 - Zones 1 and 2 both refer to soil type 1.

Example 5 - Zones 1 and 2 refer to soil types 1 and 2 respectively.

Initial conditions for the simulations correspond to static equilibrium with the toe of the slope (point B) at zero pressure head. As in previous examples, initial water contents for the hysteretic simulation were assumed to correspond to the main drainage curve. Rainfall is applied at 4.0 cm h^{-1} for a period t_1 = 18.7 h. At this application rate, ponding occurs within 0.2 - 2.1 h for all simulations. It is assumed that the pressure head along the atmospheric boundary cannot exceed zero and rainfall excess is considered to run off instantaneously. Likewise along the seepage face, all rainfall is regarded as runoff. During the evaporation period from t_1 = 18.7 h to t_2 = 138.7 h, potential evaporation was 0.02 cm h^{-1} which was assumed to be met as long as the surface pressure head exceeded -900 cm as in Example 4.

Computed zero-pressure head contours for H, NW and ND simulations during infiltration and evaporation periods are shown in Fig. 3.7. Note that the zero-pressure head contour demarks the upper edge of the seepage face. As in Example 4, fairly close correspondence between NW and H simulations is observed while ND predictions indicate a gross overestimation of infiltration into the soil. This is more directly evident in Fig. 3.8, which shows the total infiltration flux on the atmospheric boundary for H, NW and ND cases computed by summing nodal fluxes along the boundary. Analogous results for total evaporation and seepage fluxes along the boundary are given in Figs 3.9 and 3.10, respectively. The constant flux stage of evaporation continues for 24 h for the ND case, which is about twice as long as for the NW and H cases. Thereafter, the ND case evaporation flux

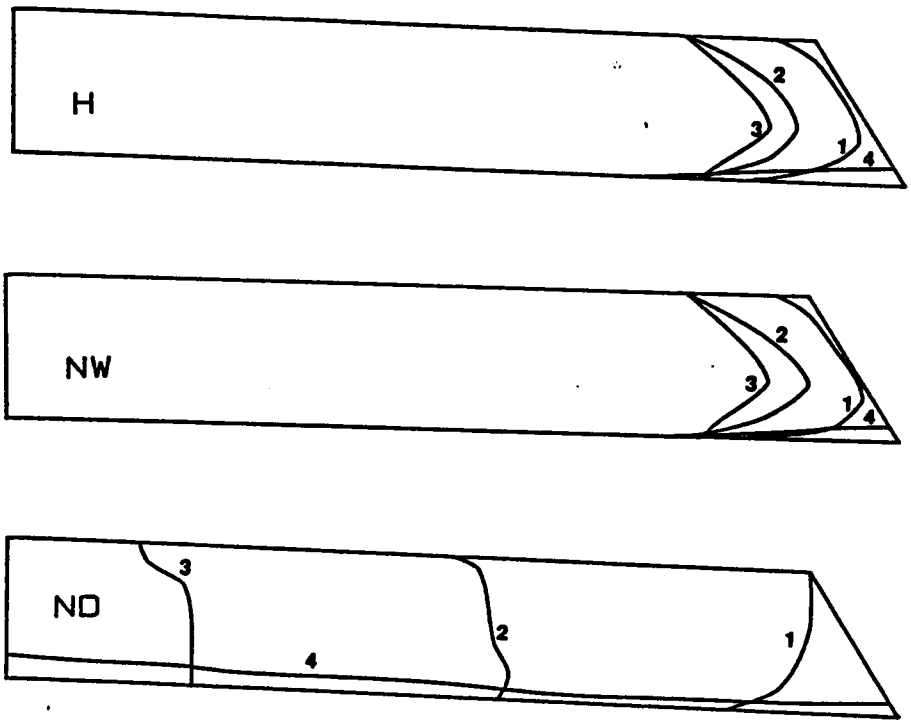

Figure 3.7 Variation of zero-pressure head contours with time for Example 4. Curves 1, 2, 3 and 4 refer to 10.1, 16.7, 18.7 and 138.7 h from the commencement of infiltration, respectively.

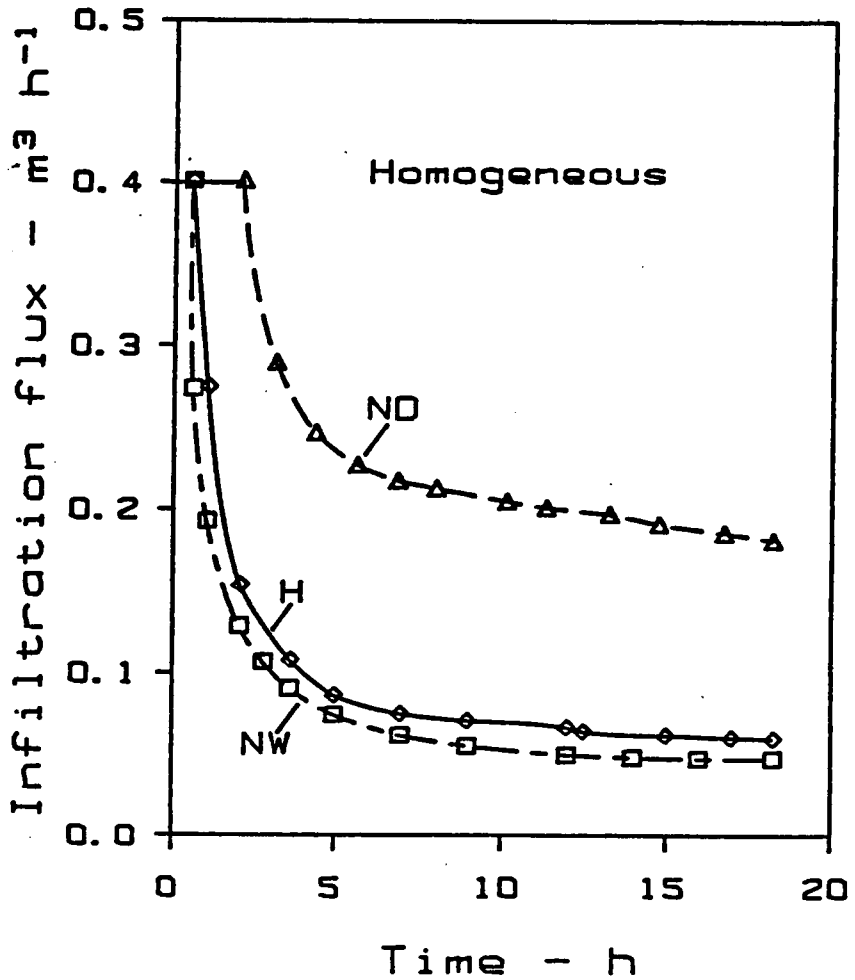

Figure 3.8 Variation of infiltration flux density ($m^3\ h^{-1}$ per m width) with time for Example 4.

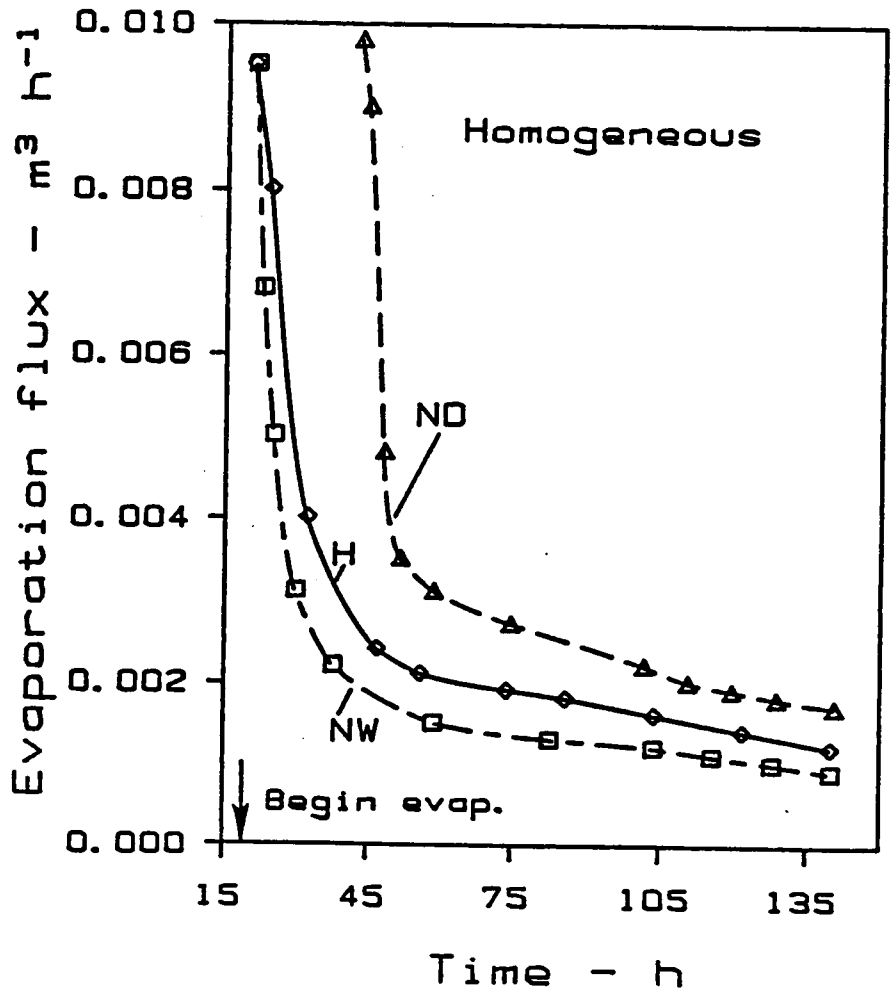

Figure 3.9 Variation of evaporation flux density ($m^3\ h^{-1}$ per m width) with time for Example 4.

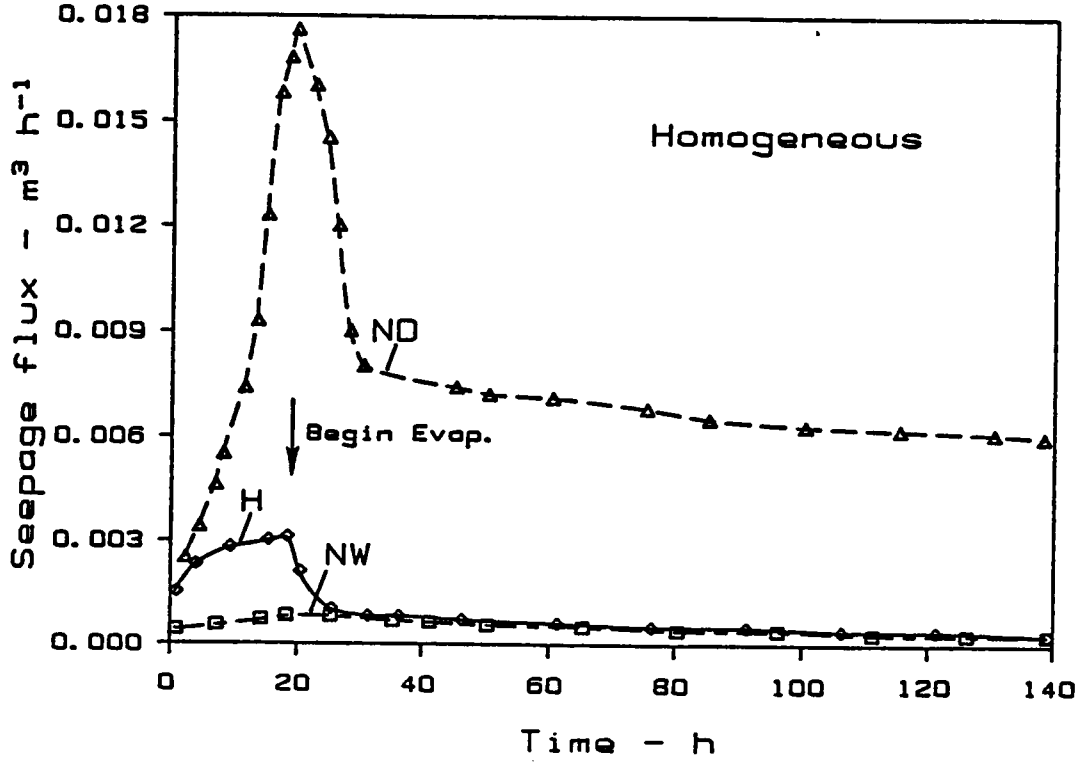

Figure 3.10 Variation of seepage flux density ($m^3\ h^{-1}$ per m width) with time for Example 4.

continues to exceed the H simulation flux, which in turn exceeds the NW case. Seepage hydrographs exhibit markedly different patterns for the three cases, but again ND-H deviations are much more severe for the initial and boundary conditions imposed than NW-H differences. A more concise characterization of the net effects of the different assumed hydraulic models may be obtained by considering various components of a time-integrated water balance over the duration of the simulation. For this purpose, we have computed cumulative total fluxes along the atmospheric boundary occurring as infiltration, evaporation, and seepage. Runoff was computed as the difference between the total rainfall (7.48 m^3 per m width) and infiltration. Net change in water storage in the soil was computed as the difference between infiltration and evaporation plus seepage. For the NW simulation, moderate underestimation of infiltration and seepage occurred relative to the H simulation while runoff and evaporation were overestimated. Net storage change for the NW case was 0.77 of that for the H simulation. In contrast, the ND simulation resulted in large overestimates of infiltration, seepage and evaporation, much less runoff and a net storage change 1.6 times greater than for the H simulation. Due to the substantial discrepancies in storage changes for the various cases, we may anticipate that effects of ignoring hysteresis will be further amplified if a second infiltration event were to follow the present simulations.

Example 5: Infiltration, evaporation and seepage in a two-dimensional, heterogeneous soil domain

In this example, we investigate the influence of nonhomogeneity in the flow domain on effects of hysteresis. The geometry of the problem and initial and boundary conditions are taken to be identical to Example 4, but with Zones 1 and 2 of the flow domain (Fig. 3.6) represented by material properties of Soils 1 and 2 (Table 3.1), respectively.

Predicted zero-pressure head contours for H, NW and ND simulations are shown in Fig. 3.11 for selected times during rainfall and potential evaporation periods. Relative to the corresponding homogeneous case, marked differences are observed due to impedance of vertical and lateral water movement in the soil. As in the homogeneous case, substantial deviations occur between ND and H simulations while NW and H simulation discrepancies are less severe. Details of the behavior for the different simulations are more readily discerned by comparing total infiltration, evaporation and seepage fluxes on the atmospheric boundary versus time for H, NW and ND cases (Figs. 3.12 - 3.14). Comparison with Example 4 indicates that differences between NW- and H-simulated infiltration fluxes and, especially, seepage fluxes are smaller for the nonhomogeneous medium, suggesting that effects of hysteresis are diminished by heterogeneity. However, it is also observed that deviations between ND and H or NW simulation evaporation fluxes are larger for the heterogeneous case relative to the corresponding homogeneous problem indicating that

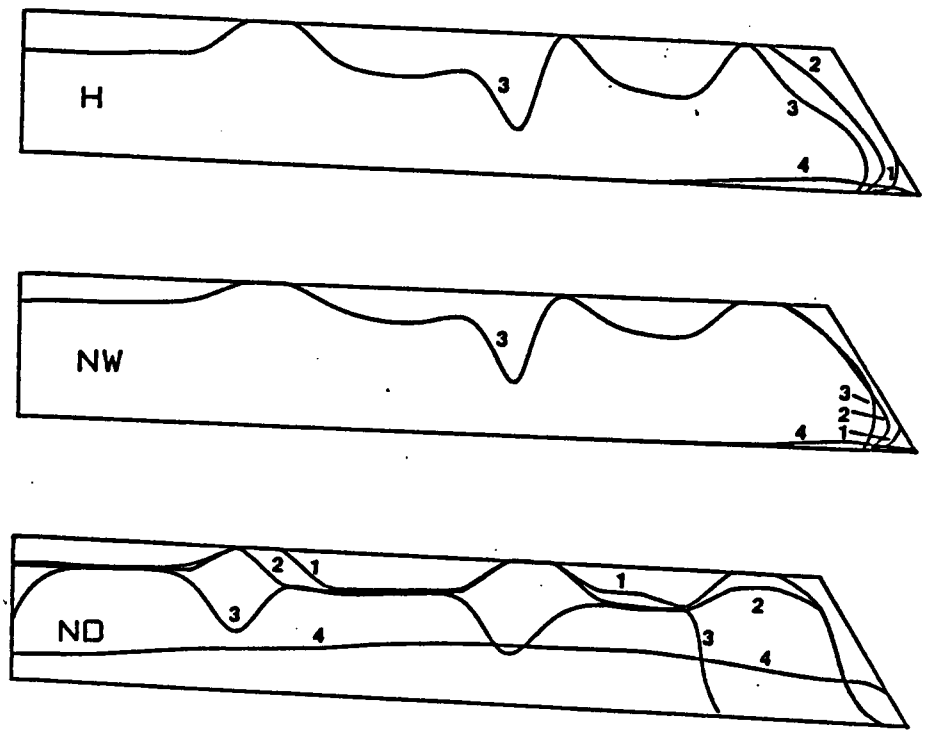

Figure 3.11 Variation of zero-pressure head contours with time for Example 5. Curves 1, 2, 3 and 4 refer to 6.1, 10.4, 18.2 and 138.7 h from the commencement of infiltration, respectively.

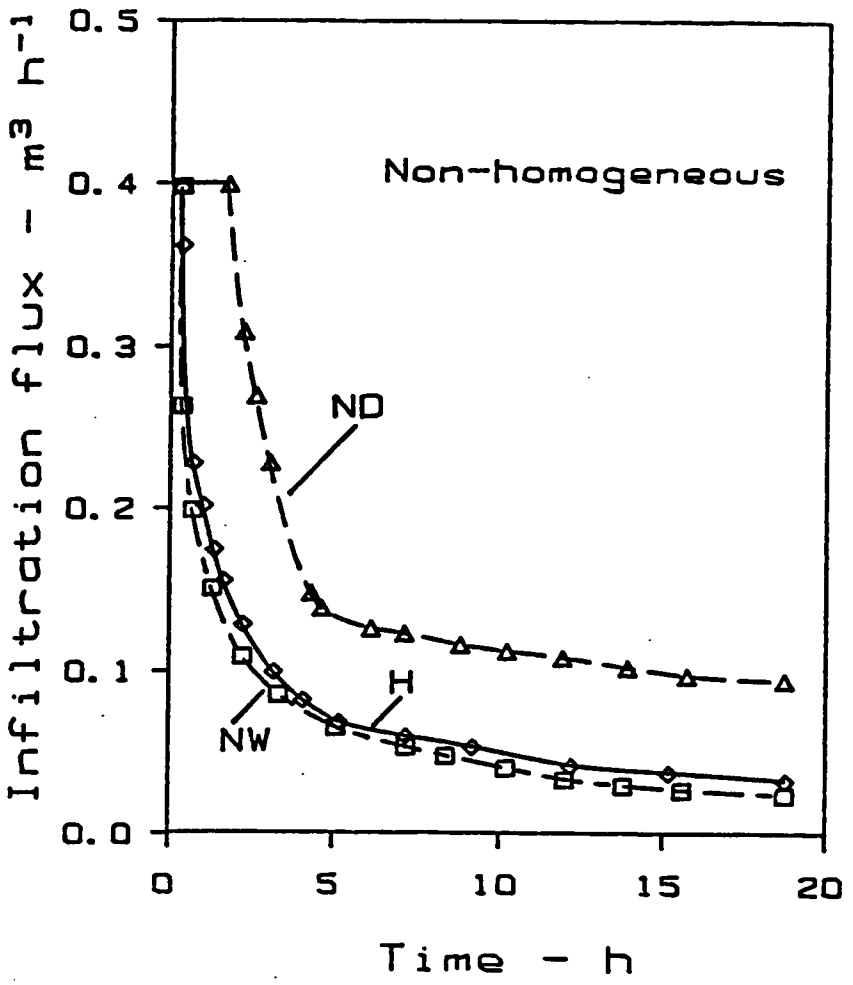

Figure 3.12 Variation of infiltration flux density ($m^3\ h^{-1}$ per m width) with time for Example 5.

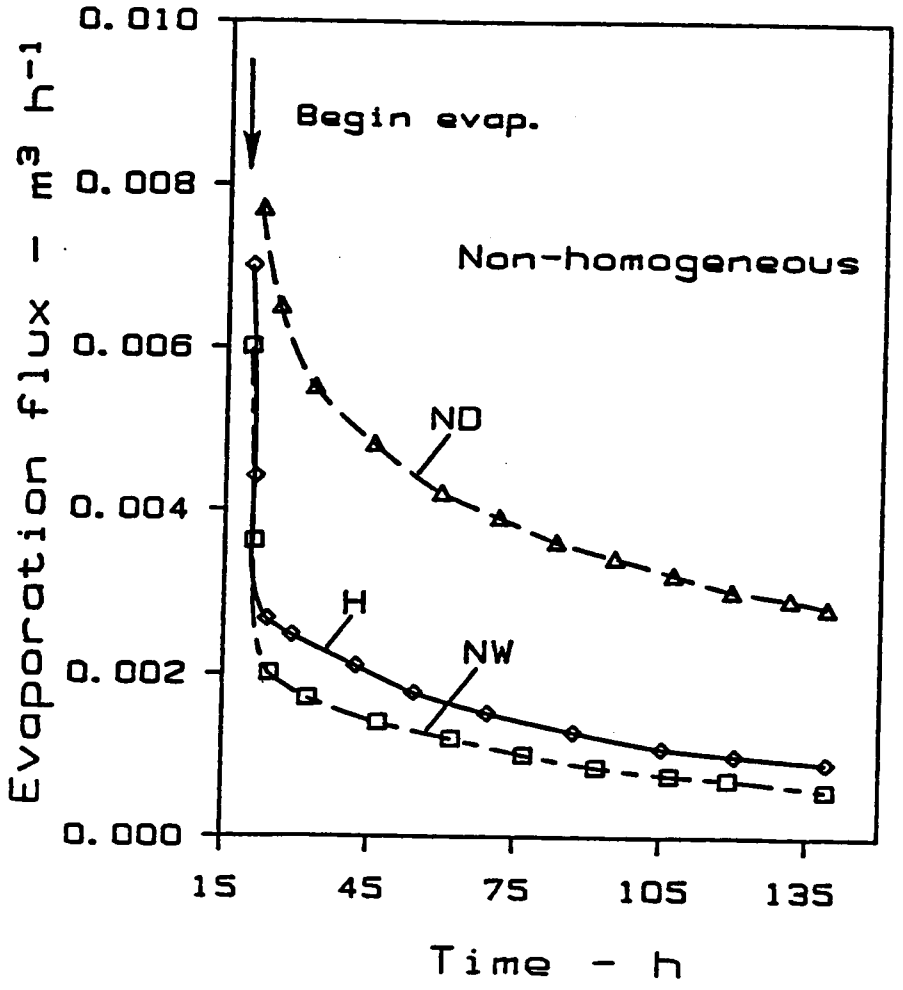

Figure 3.13 Variation of evaporation flux density ($m^3\ h^{-1}$ per m width) with time for Example 5.

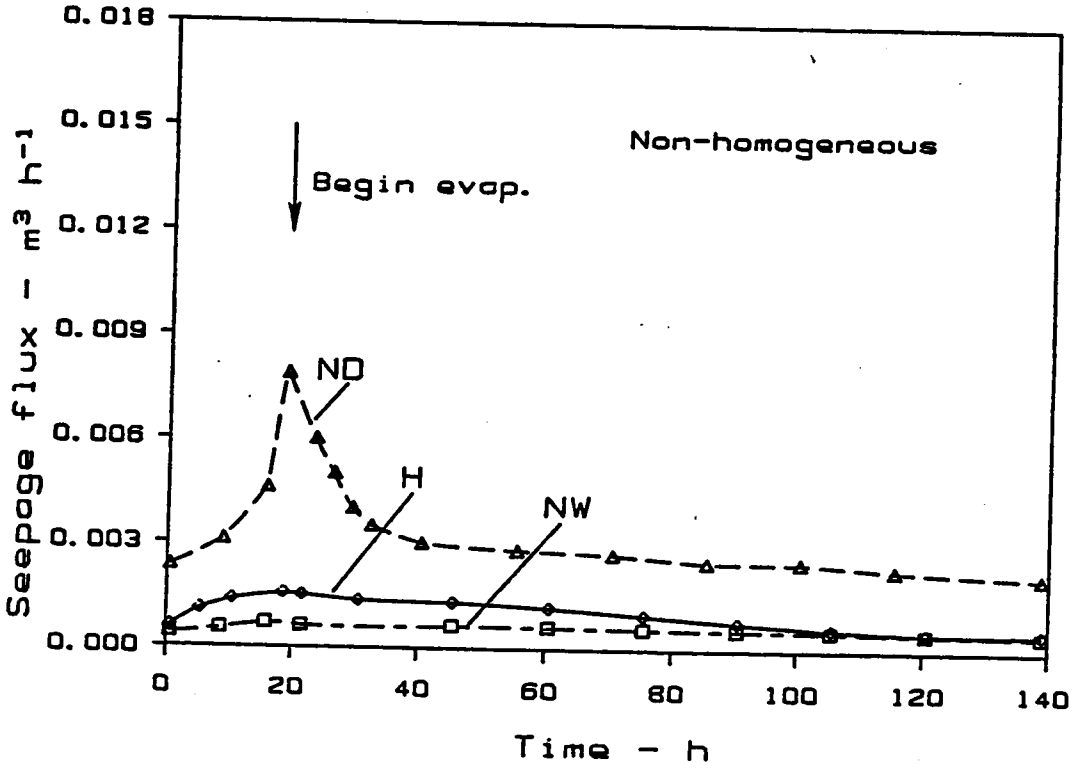

Figure 3.14 Variation of seepage flux density ($m^3\ h^{-1}$ per m width) with time for Example 5.

generalities regarding the influence of heterogeneity on hysteresis effects must be drawn with caution. The cause of the relatively large evaporative fluxes in the ND case in the heterogeneous domain is attributable to the contribution of capillary rise from the water table adjacent to the seepage face which in turn reflects the predicted slow water table fall due to greater lateral flow impedance. This increased impedance is also evidenced in the substantially greater damping in the seepage hydrographs for the homogeneous material compared to those of Example 4. Temporally averaged effects of the lower conductivity material of Zone 2 on surface fluxes is clearly evident in the water balance components computed for the duration of the simulation (Table 3.2). Introduction of heterogeneity into the system is seen to generally reduce the discrepancies between ND-H and NW-H simulation water balance components. The marked exception is for evaporation which is predicted to be 4.5 times larger for the ND simulation than the H simulation while the NW case is only 0.97 times the H simulation value.

CONCLUSIONS

Effects of ignoring hysteresis with air entrapment in analyses of unsaturated flow have been shown to vary with specific boundary and initial conditions and problem geometry. Minimal effects of hysteresis may be expected when flux-controlled boundary conditions occur, as for example for low intensity rainfall or evaporation, and when similar initial water content distributions occur. Under such circumstances,

Table 3.2 Water balance components during infiltration and evaporation for the two-dimensional simulations.

Case	Components - m^3 per m width					
	I	R	E	SL_i	SL_e	ΔS
Example 4						
H	1.790	5.690	0.660	0.048	0.101	0.981
NW	1.510	5.970	0.672	0.012	0.086	0.740
ND	4.390	3.090	1.084	0.164	0.681	2.461
Example 5						
H	1.480	6.000	0.134	0.020	0.098	1.228
NW	1.400	6.080	0.130	0.011	0.078	1.181
ND	3.110	4.380	0.603	0.068	0.311	2.119

I -infiltration; E -Evaporation; R -Runoff; SL_i -Seepage loss during infiltration; SL_e -Seepage loss during evaporation; ΔS -net storage change

evolution of water content profiles will depend predominantly on the $K(\theta)$ function which exhibits little hysteresis. Correct prediction of pressure head distributions, however, will still require the appropriate hysteretic $\theta(h)$.

Much larger differences between hysteretic and nonhysteretic simulations arise when potential-type boundary conditions occur. Substantial differences were observed during ponded infiltration for H and ND simulations while H-NW differences were comparatively small. Air entrapment has a major effect by reducing the conductivity at the soil surface, and hence the infiltration rate, for the NW case relative to ND simulations. For wetting from relatively dry initial conditions, actual air entrapment will be similar to that corresponding to the main wetting $\theta(h)$ curve, resulting in better correspondence between H-NW than H-ND simulations.

Variations in initial conditions can influence the effects of hysteresis in several ways. When initial conditions involve prescribed heads rather than water contents, substantially different initial water content distributions will be predicted for nonhysteretic simulations depending on whether draining or wetting properties are employed, and for hysteretic simulations depending on the saturation history. As a result, different quantities of water will be available for evaporation or redistribution and different water deficits will affect rates of penetration of infiltrating water. Nonconstant initial water contents will result in hysteretic simulations following different scanning curves with different potential entrapped air amounts at each depth, which will produce behavior not readily approximated by a single monotonic

function. When boundary conditions change, for example from infiltration to evaporation, conditions at the end of the infiltration event may control subsequent behavior to a large extent. Errors incurred due to disregarding hysteresis at earlier times will tend to be magnified rather than damped with time unless conditions arise which cause the soil to become uniformly saturated or very dry.

In the two-dimensional problems, marked differences were observed in infiltration and evaporation fluxes, seepage hydrographs and net changes in soil water storage between hysteretic and nonhysteretic simulations, with H-ND differences most severe. Differences between H-NW simulations were less marked but increased with simulation time particularly as boundary conditions changed. Introducing heterogeneity into the system resulted in a diminution of the effects of hysteresis on infiltration and seepage, but further accentuated differences in evaporation predicted with and without consideration of hysteresis due to specific interactions between seepage and evaporation in this problem. Thus, it would appear that while heterogeneity may attenuate effects of hysteresis in certain cases, this should not be taken as an general truth.

The results indicate that except for very simple initial and boundary conditions and system geometries, disregarding hysteresis -- especially when air entrapment is a consideration -- will lead to substantial errors in predicted water content and pressure distributions and surface fluxes. We suggest that in the absence of detailed knowledge of hysteretic soil hydraulic properties, use of a simple parametric model for hysteresis will be preferable to

disregarding hysteresis entirely.

REFERENCES

Beese, F. and R. R. van der Ploeg, 1976, Influence of hysteresis on moisture flow in an undisturbed soil monolith, Soil Sci. Amer. J., 40, 480-484.

Curtis, A. A. and K. K. Watson, 1984, Hysteresis affected water movement in scale heterogeneous profiles, Water Resour. Res., 20, 719-726.

Dane, J. H. and P.J. Wierenga, 1975, Effects of hysteresis on the prediction of infiltration, redistribution and drainage of water in a layered soil, J. Hydrol., 25, 229-242.

Fayer, M. J. and D. Hillel, 1986, Air encapsulation: I. Measurement in a field soil, Soil Sci. Soc. Amer. J., 50, 568-572.

Fayer, M. J. and D. Hillel, 1986, Air encapsulation: II. Profile water storage and shallow water table fluctuations, Soil Sci. Soc. Amer. J., 50, 572-577.

Gillham, R. W., A. Klute and D. F. Heermann, 1976, Hydraulic properties of a porous medium; Measurements and empirical representation, Soil Sci. Soc. Amer. J., 43, 1061-1067

Hanks, R. J., A. Klute and E. Bresler, 1969, A numerical method for estimating infiltration, redistribution, drainage and evaporation of water from soil, Water Resour. Res., 5, 1064-1069

Hoa, N. T., R. Gaudu and C. Thirriot, 1977, Influence of the hysteresis effects on transient flows in saturated-unsaturated porous media, Water Resour. Res., 13, 992-996.

Hopmans, J. W. and J. H. Dane, 1986, Temperature dependence of soil water retention curves, Soil Sci. Soc. Amer. J., 50, 562-567.

Huyakorn, P. S., D. Thomas and B. M. Thompson, 1984, Techniques for making finite element competitive in modeling flows in variably saturated porous media, Water Resour. Res., 20, 1099-1115.

Jaynes, D. B., 1985, Comparison of soil-water hysteresis models, J. Hydrol., 75, 287-299.

Kaluarachchi, J. J. and J. C. Parker, 1987, Finite element analysis of water flow in variably saturated soil, J. Hydrol., 90, 269-291.

Killough, J. E., 1976, Reservoir simulation with history-dependent saturation functions, Trans. Am. Inst. Mining Eng., 261, 37-40.

Kool, J. B. and J. C. Parker, 1987, Development and evaluation of closed-form expressions for hysteretic soil hydraulic properties, Water Resour. Res., 23, 105-114.

Kool, J. B., J. C. Parker and M. Th. van Genuchten, 1986, The inverse problem for hysteretic unsaturated flow, Proc. 6th International Conference on Finite Elements in Water Resources, Lisbon, Portugal, June, p.337-346.

Milly, P. C. D., 1982, Moisture and heat transport in hysteretic, inhomogeneous porous media: A matric head-based formulation and a numerical model, Water Resour. Res., 18, 489-498.

Montaglou, A. and L. W. Gelhar, A stochastic approach for modeling large-scale transient unsaturated flow, Proc. Symp. on the Stochastic Approach to subsurface flow, Montvillargenne, June 3-6, 1986, Association Internationale de Recherche Hydraulique, Ecole des Mines de Paris, Fontainebleau, France.

Mualem, Y., 1974, A conceptual model of hysteresis, Water Resour. Res., 10, 514-520.

Mualem, Y., 1984, A modified dependent domain theory of hysteresis, Soil Sci., 137, 283-291.

Neuman, S. P., 1973, Saturated-unsaturated seepage by finite elements, J. Hydraul. Div., ASCE, 99, 2233-2250.

Parker, J. C. and R. J. Lenhard, 1987, A model for hysteretic constitutive relations governing multiphase flow, 1. Saturation-pressure relations, Water Resour. Res., (in press).

Perrens, S. J. and K. K. Watson, 1971, Numerical analysis of two-dimensional infiltration and redistribution, Water Resour. Res., 13, 781-790.

Pickens, J. F. and R. W. Gillham, 1980, Finite element analysis of solute transport under hysteretic unsaturated flow conditions, Water Resour. Res., 16, 1071-1078.

Royer, J. M. and G. Vachaud, 1975, Field determination of hysteresis in soil-water characteristics, Soil Sci. Soc. Amer. J., 39, 221-223.

Rubin, J., 1967, Numerical method for analyzing hysteresis-affected, post-infiltration redistribution of soil moisture, Soil Sci. Soc. Amer. J., 31, 13-20.

Scott, P. S., G. J. Farguhar and N. Kouwen, 1983, Hysteretic effects on net infiltration, In: Advances In Infiltration, Am. Soc. Agric. Eng. Publ. 11-83, St. Joseph, Michigan, p.163-170.

Stauffer, F. and Th. Dracos, 1984, Local infiltration into layered soil and response of the watertable; Experiment and simulations, In: Frontier in Hydrology, Water Resources Publication, Littleton, Colorado, p. 228-242.

Staple, W. J., 1969, Comparison of computed and measured moisture redistribution following infiltration, Soil Sci. Soc. Amer. J., 33, 840-847.

Topp, G. C., 1971, Soil-water hysteresis: The domain model theory extended to pore interaction conditions, Soil Sci. Amer. Proc., 33, 645-651.

van Genuchten M. Th., 1980, A closed-form equation for predicting the hydraulic conductivity of unsaturated soils, Soil Sci. Soc. Amer. J., 44, 892-898.

CHAPTERT IV

FINITE ELEMENT ANALYSIS OF NITROGEN TRANSPORT AND TRANSFORMATION

ABSTRACT

A two dimensional finite element model based on Galerkin's weighted residual approach and incorporating an upstream weighting technique was developed to predict the simultaneous transformation and transport of nitrogen species. The nitrogen cycle used in the analyses assumes first order rate coefficients for nitrification, denitrification, immobilization and mineralization between the nitrogen species NH_4^+, NO_3^-, organic-N and denitrified fractions. The NO_3^--N component in the soil solution was assumed to have negligible adsorption on exchange sites while adsorption of NH_4^+ was assumed to be represented by a Freundlich type nonlinear isotherm ($S = K_dCP$). The accuracy and validity of the proposed model was examined by comparison with analytical model results and available field data. The results showed improved accuracy and stability with the upstream weighting approach in comparison to the standard weighted residual method. A sensitivity study of the kinetics of the nitrogen cycle showed that both concentration and cumulative mass distribution of different nitrogen species are substantially affected by the nitrification rate but to a lesser extend by the distribution coefficient k_d for NH_4^+ adsorption and less so by nonlinear coefficient p. To evaluate the applicability of the model in actual field situations, data on groundwater nitrogen

concentration beneath a functioning drainfield site were compared with the results of numerical simulations. Predicted results agreed with the observed data within the bounds of experimental errors.

INTRODUCTION

Contamination of groundwater resources with nitrogen species is an important environmental concern. Common sources of nitrogen contamination in groundwater include leachate from lagoons, drainfields and land application systems used for disposal of domestic, industrial and agricultural wastewater; land disposal of sludges, manure and other solid wastes; and losses from excess applied nitrogen fertilizer. To model the movement of nitrogen species through the unsaturated zone to groundwater and subsequently in the groundwater itself, due consideration must be given to the complex interactions and transformations involved in the nitrogen cycle. The principal forms of soil nitrogen are NH_4^+, NO_3^-, organic-N and denitrified gaseous nitrogen species. Most solution phase N will be in the form of NH_4^+ or NO_3^-, although the former is less prone to leaching due to retardation by solid phase partitioning associated with cation exchange on negatively charged soil surfaces.

A number of concurrent biological transformations between nitrogen species may occur which will continuously alter the distribution of N among various forms. The exact mechanisms controlling these transformations are generally not fully understood and in most instances the reactions are assumed to be first-order and reversible

and/or irreversible depending on the specific species. An important additional mitigating factor in nitrogen transport within the zone of active plant activity is uptake of N by plant roots.

Mathematical modeling of nitrogen movement in soils is further complicated by spatial and temporal variations in soil properties and hydraulic conditions which influence N transformations and transport. Early researchers (Cho, 1971; Misra et al., 1974) circumvented these difficulties by assuming homogeneous soil systems subject to steady state flow regimes for which analytical solutions to the convection-dispersion equation are feasible given also suitable simplifications in the description of N transformations. Such simplified models have been successfully applied to well controlled laboratory column experiments enabling verification of the adequacy of first-order kinetics to describe nitrification and denitrification reactions (Starr et al., 1974; Stanford et al., 1975).

The major disadvantage of analytical models is that field situations can seldom be adequately represented as homogeneous systems under steady state hydraulic conditions. In order to describe soil systems in a more realistic manner, it is necessary to consider explicitly the nonuniformity in soil properties which may affect nitrogen transport and transformations and the transient nature of atmospheric conditions which controls the hydraulic regime and surface N inputs and losses. To accomodate such phenomena, the use of numerical models becomes mandatory.

Numerical models describing the movement of nitrogen species which accomodate transient flow conditions based on a mixing cell

approach have been proposed by various researchers (Duffy et al., 1975; van Veen and Frissell, 1976). More recently, models based on finite difference analyses have been described by Gureghian et al. (1979) and Selim and Iskandar (1981a). The latter has been validated under field conditions (Selim and Iskandar, 1981b). A major limitation of these models is that they are restricted to one dimension which precludes application to problems where sources are nonuniformly distributed or where flow paths are divergent.

The objectives of this paper are to present a flexible and computationally efficient two dimensional numerical model for the prediction of transformation and transport of nitrogen species in a variably saturated medium under transient flow conditions. The accuracy and dependability of the model will be verified by selected sensitivity analyses and model validation against available field data.

ANALYSIS OF VARIABLY SATURATED FLOW

The single phase formulation for flow in a variably saturated domain under isothermal conditions in two dimensions may be written as:

$$\frac{\partial}{\partial x}\left[K_x(\psi)\,\frac{\partial \Phi}{\partial x}\right] + \frac{\partial}{\partial z}\left[K_z(\psi)\,\frac{\partial \Phi}{\partial z}\right] + Q^* - C(\psi)\,\frac{\partial \psi}{\partial t} = 0 \qquad (4.1)$$

where ψ is pressure head, $\Phi = \psi + z$ is the hydraulic head, K_x and K_z are components of the conductivity tensor along assumed principal directions x and z with z taken as the vertical coordinate measured

positive upwards, Q^* is the flow due to sources or sinks located in the region ($L^3L^{-3}T^{-1}$), $C = \partial\theta/\partial\psi$ is the specific water capacity where θ is the volumetric water content, and t is time.

Soil hydraulic properties are assumed to be described by the van Genuchten (1980) model as:

$$S_e = \frac{\theta - \theta_r}{\theta_s - \theta_r} = [1 + |\alpha^*\psi|^n]^{-m} \qquad (4.2a)$$

$$K = K_s\, S_e^{1/2}\, [1 - (1-S_e^{1/m})^m]^2 \qquad (4.2b)$$

where θ_s and θ_r are saturated and residual water contents, K_s is the saturated hydraulic conductivity, n is a parameter related to the pore size distribution, α^* is a constant and $m = 1-1/n$.

Initial and boundary conditions for (4.1) are

$$\psi(x,z,0) = \psi_0(x,t) \qquad \text{for } t=0 \text{ in } R \qquad (4.3a)$$

$$\psi(x,z,t) = \psi_1(x,z,t) \qquad \text{for } t>0 \text{ on } S_1 \qquad (4.3b)$$

$$-\left[K_x \frac{\partial\phi}{\partial x} n_x + K_z \frac{\partial\phi}{\partial z} n_z\right] = q_n(t) \qquad \text{for } t > 0 \text{ on } S_2 \qquad (4.3c)$$

where R denotes the entire flow domain and S_1 and S_2 are boundaries of the domain. Equation (4.3a) describes the initial conditions in terms of the pressure function ψ_0. Equation (4.3b) describes the boundary S_1 on which Dirichlet or specified potential type boundary conditions are applicable. Equation (4.3c) describes the Neuman or flux-type boundary condition on S_2 where n_x and n_z are unit vectors in the x and z directions and q_n is the flux normal to boundary S_2. In addition to these boundary conditions, parts of the flow domain may be

exposed to atmospheric type conditions (rainfall or evaporation) for which boundary condition may change between Dirichlet and Neuman type. Seepage faces may also occur along part of the boundary which cannot be a priori specified.

From the solution to (4.1) components of the water flux which are required for analysis of species transport are obtained from Darcy's equation:

$$q_x = - K_x \frac{\partial \Phi}{\partial x} \tag{4.4a}$$

$$q_z = - K_z \frac{\partial \Phi}{\partial z} \tag{4.4b}$$

where q_x and q_z are flux components in x and z directions, respectively.

The numerical solution of the (4.1) is obtained by a Galerkin finite element analysis. Details of the formulation and solution procedure have been presented in chapter II and will not be repeated here.

ANALYSIS OF NITROGEN TRANSPORT

Governing Equations

A diagramatic representation of the nitrogen transformation model is shown in Fig. 4.1. Nitrification ($NH_4^+ \rightarrow NO_3^-$) and denitrification ($NO_3^- \rightarrow$ denitrified-N) are assumed to follow irreversible first order kinetics (Starr et al., 1974; Stanford et al., 1975). Conversion of the intermediary NO_2^- during nitrification is assumed to be sufficienty rapid to permit neglecting this species (Misra et al., 1974). First order

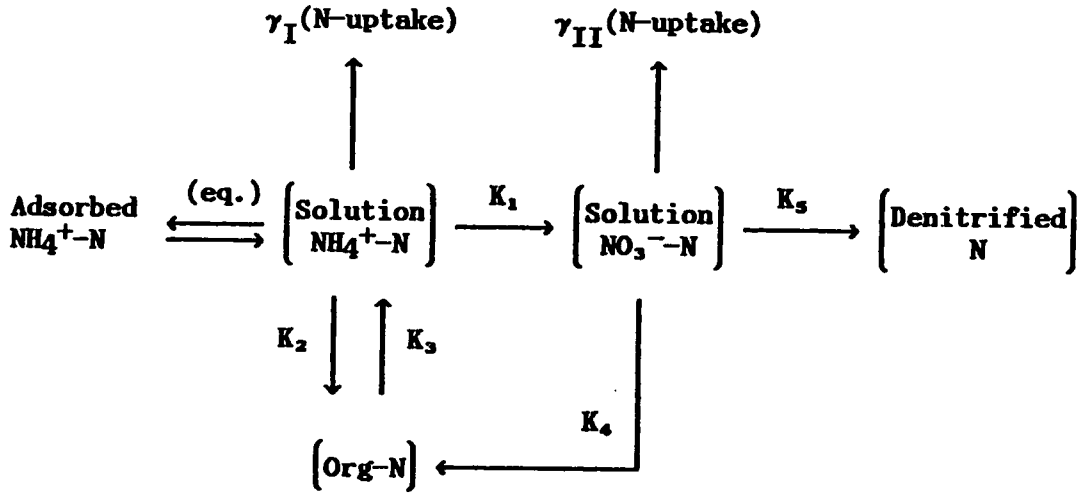

Figure 4.1 Nitrogen speciation model used in the analysis. Variables K_1- K_5 are first order rate constants and γ_I and γ_{II} are zero order rate constants.

kinetics are assumed also for immobilization of NH_4^+ and NO_3^- to organic fractions and for mineralization of organic nitrogen to NH_4^+. For simplicity, plant uptake of NH_4^+ and NO_3^- are assumed to obey zero order kinetics. Exchange of NH_4^+ between soil solution and adsorbed phase is assumed to be reversible and instantaneous.

Solution phase NO_3^- and NH_4^+ are subject to convective-dispersive transport described by:

$$\rho \frac{\partial S_i}{\partial t} + \frac{\partial C_i \theta}{\partial t} - \frac{\partial}{\partial x}\left[D_x \frac{\partial C_i}{\partial x}\right] - \frac{\partial}{\partial z}\left[D_z \frac{\partial C_i}{\partial z}\right]$$

$$+ \frac{\partial C_i q_x}{\partial x} + \frac{\partial C_i q_z}{\partial z} - Q^* C_i^* + \Phi_i = 0 \qquad (4.5)$$

where C_i is the solution phase concentration of species i (ML^{-3}), ρ is the bulk density of the medium (ML^{-3}), S_i is the adsorbed mass of species i per unit mass of soil (MM^{-1}), C_i^* is the concentration of species i in fluid line sources or sinks, and Φ_i is the net rate of transformations for species i ($ML^{-3}T^{-1}$). The dispersion coefficients D_x and D_z in the x and z directions are given by (Bear, 1972)

$$D_x = D_o\tau + \lambda_L q_x/|q| + \lambda_T q_z/|q| \qquad (4.6a)$$

$$D_z = D_o\tau + \lambda_L q_z/|q| + \lambda_T q_x/|q| \qquad (4.6b)$$

where D_o is the molecular diffusion coefficient in bulk water (regarded here as independent of species), λ_L and λ_T are longitudinal and transverse dispersivities, $|q| = (q_x^2 + q_z^2)^{1/2}$ is the magnitude of the hydraulic flux, and $\tau = \theta^{4.3}/\theta_s^2$ is a tortuosity coefficient modeled after Millington (1959). Off-diagonal terms in the dispersion tensor are

disregarded in the above formulation eliminating mixed space derivative terms which would otherwise arise in (4.5).

Adsorption is considered instantaneous and reversible with equilibrium defined by a Freundlich type isotherm of the form

$$S_i = k_d C_i^p \tag{4.7}$$

where k_d and p are parameters in general specific to the particular soil material and species under consideration. Since adsorption will be considered significant only for NH_4^+, we omit species subscripts on Freundlich parameters.

Equation (4.5) may be simplified using (4.7) to eliminate S_i under the assumption of local equilibrium and employing also the continuity equation for water:

$$\frac{\partial \theta}{\partial t} = - \frac{\partial q_x}{\partial x} - \frac{\partial q_z}{\partial z} + Q^* \tag{4.8}$$

The resulting form of (4.5) is:

$$R_i^* \theta \frac{\partial C_i}{\partial t} - \frac{\partial}{\partial x}\left[D_x \frac{\partial C_i}{\partial x}\right] - \frac{\partial}{\partial z}\left[D_z \frac{\partial C_i}{\partial z}\right] + q_x \frac{\partial C_i}{\partial x} + q_z \frac{\partial C_i}{\partial z}$$

$$+ Q^*(C_i - C_i^*) + \Phi_i = 0 \tag{4.9}$$

where the retardation factor R_i^* is given by:

$$R_i^* = 1 + \rho p k_d C_i^{p-1}/\theta \tag{4.10}$$

We shall regard species I and II to represent NH_4^+ and NO_3^-, respectively. All concentrations will be in N-equivalent mass per unit volume of soil solution i.e., C_I and C_{II} denote solution phase NH_4^+-N

and NO_3^--N, respectively. Since adsorption is assumed negligible for NO_3^-, $R^*_{II} = 1$. For the nitrogen transformation pathways shown in Fig. 4.1, the net transformation rate Φ_I for NH_4^+-N can be written as

$$\Phi_I = K_1 C_I \theta + K_2 C_I \theta - \rho K_3 S_{on} + \gamma_I \qquad (4.11)$$

where S_{on} is the concentration of organic-N expressed as mass per unit mass of soil, K_1, K_2 and K_3 are first order rate coefficients (T^{-1}) for nitrification, immobilization of NH_4^+ and mineralization of organic-N, respectively, and γ_I is the zero order rate constant describing plant uptake of NH_4^+-N. For NO_3^--N the net transformation rate is given by

$$\Phi_{II} = K_4 C_{II} \theta + K_5 C_{II} \theta + \gamma_{II} - K_1 C_I \theta \qquad (4.12)$$

where K_4 and K_5 are first order rate constants for immobilization of NO_3^- and for denitrification, respectively, and γ_{II} is the zero order rate constant for NO_3^--N uptake by plants.

Initial and boundary conditions for species transport may be written as

$$C_i = C_i(x,z,0) \qquad \text{for } t = 0 \text{ in } R \qquad (4.13a)$$

$$C_i = C_{io}(x,z,t) \qquad \text{for } t > 0 \text{ on } S_1' \qquad (4.13b)$$

$$q_n C_{io} = a q_n C_i - D_x \frac{\partial C_i}{\partial x} n_x - D_z \frac{\partial C_i}{\partial z} n_z \quad \text{for } t > 0 \text{ on } S_2' \qquad (4.13c)$$

Equation (4.13a) describes the initial distribution of species i. Equation (4.13b) describes Dirichlet-type prescribed concentration boundaries along surface S_1' with a surface concentration C_{io}. Equation (4.13c) describes mixed-type boundaries on surface S_2' for a=1

when the right hand side corresponds to the total solute flux and Neuman-type boundaries for a=0 when the RHS represents dispersive flux only. Here C_{io} represents the applied surface concentration of species i.

Finite Element Formulation

Prior to discussing details of numerical solution procedures employed for convective-dispersive transport, we note that the expressions for NH_4^+-N and NO_3^--N transformation rates (Eqs. 4.11 and 4.12) may both be written in the form:

$$\Phi_i = H_i C_i + G_i \tag{4.14a}$$

where for NH_4^+-N the H_i and G_i terms are given by:

$$H_I = K_1\theta + K_2\theta \tag{4.14b}$$

$$G_I = \gamma_I - \rho K_3 S_{on} \tag{4.14c}$$

and for NO_3^--N the respective relations are:

$$H_{II} = K_4\theta + K_5\theta \tag{4.14d}$$

$$G_{II} = \gamma_{II} - K_1 C_I \theta \tag{4.14e}$$

It may be noted that the transport equation for NH_4^+-N exhibits no dependence on NO_3^--N concentration, while NO_3^--N transport exhibits dependence on NH_4^+-N via G_{II}. Since coupling between the transport equations is one sided, the system solution may be obtained by sequentially solving the NH_4^+-N transport equation (C_I) followed by the NO_3^--N equation (C_{II}). No iteration between transport equations is required. Furthermore, iterative solution of the individual species

transport equations arises only for NH_4^+-N transport in the event that the Freundlich exponent $p \neq 1$.

In order to simplify notation in describing the numerical solution of the NH_4^+ and NO_3^- transport equations, we drop species subscripts subsequently and write a generic transport equation as:

$$R^*\theta \frac{\partial C}{\partial t} - \frac{\partial}{\partial x}\left[D_x \frac{\partial C}{\partial x}\right] - \frac{\partial}{\partial z}\left[D_z \frac{\partial C}{\partial z}\right] + q_x \frac{\partial C}{\partial x} + q_z \frac{\partial C}{\partial z}$$

$$+ Q^*(C-C^*) + HC + G = 0 \qquad (4.15)$$

for which a numerical solution will be sought via a Galerkin finite element method.

In chemical transport problems involving low dispersion coefficients, sharp solute fronts may arise which lead to numerical oscillations and mass balance errors. A dependable approach to overcome this problem is to use upstream weighting (Huyakorn and Nilkuha, 1979; Huyakorn et al., 1984). In the method of upstream weighting, unsymmetric weighting functions are applied to terms containing space derivatives while conventional symmetric basis functions are applied to other terms. Details pertaining to the description of the upstream weighting functions W_J and symmetric weighting functions N_J at node J are given in Appendix D. Applying Galerkin's principle to (4.15) using both symmetric shape functions and unsymmetric upstream weighting functions, we obtain:

$$\int_{R_e} N_I \, R^* \frac{\partial C}{\partial t} \, dR - \int_{R_e} W_I \left[\frac{\partial}{\partial x}\left(D_x \frac{\partial C}{\partial x}\right) + \frac{\partial}{\partial z}\left(D_z \frac{\partial C}{\partial z}\right)\right] dR$$

$$+ \int_{R_e} W_I \left[q_x \frac{\partial C}{\partial x} + q_z \frac{\partial C}{\partial z} \right] dR + \int_{R_e} N_I \, Q^* \, (C-C^*) \, dR$$

$$+ \int_{R_e} N_I \, (HC + G) \, dR = 0 \qquad (4.16)$$

where R_e denotes the element area. Using Green's theorem on the second integral combined with the boundary condition given by (4.13c), (4.16) can be written as:

$$\int_{R_e} N_I \, R^* \theta \frac{\partial C}{\partial t} \, dR - \int_{R_e} \left[D_x \frac{\partial C}{\partial x} \frac{\partial W_I}{\partial x} + D_z \frac{\partial C}{\partial z} \frac{\partial W_I}{\partial z} \right] dR$$

$$+ \int_{R_e} W_I \left[q_x \frac{\partial C}{\partial x} + q_z \frac{\partial C}{\partial z} \right] dR$$

$$+ \int_{R_e} N_I \, Q^* \, (C-C^*) \, dR + \int_{R_e} N_I \, (HC + G) \, dR$$

$$- \int_{S_e} W_I (aC - C_o) q_n \, dS = 0 \qquad (4.17)$$

Assuming line sources or sinks to be located at nodes, the Q^* term in (4.17) can be simplified as:

$$\int_{R_e} N_I \, Q_L \, \delta(x-x_L) \, \delta(z-z_L) \, (C_L-C^*) \, dR = Q_L(C_L-C^*) \qquad (4.18)$$

where Q_L is the volumetric flow rate at node L per length of line source-sink $(L^3L^{-1}T^{-1})$, C_L is the concentration at node L, and δ is

the Dirac delta function. In the case of a hydraulic sink ($Q_L<0$), $C_L = C^*$ and the term vanishes.

In matrix form, we may write (4.17) as:

$$[A]\ \{C\} + [B]\left\{\frac{\partial C}{\partial t}\right\} + \{F\} = 0 \tag{4.19}$$

where

$$A_{IJ} = \sum_{e=1}^{N} \left\{ \int_{R_e} \left[D_x \frac{\partial W_I}{\partial x} \frac{\partial N_J}{\partial x} + D_z \frac{\partial W_I}{\partial z} \frac{\partial N_J}{\partial z} \right] dR \right.$$

$$+ \int_{R_e} W_I \left[q_x \frac{\partial N_J}{\partial x} + q_z \frac{\partial N_J}{\partial z} \right] dR$$

$$\left. + \int_{R_e} H\, N_I\, N_J\, dR - a \int_{S_e} W_I\, N_J\, q_n\, dS \right\} \tag{4.20a}$$

$$B_{IJ} = \sum_{e=1}^{N} \int_{R_e} R^* \theta\, N_I\, N_J\, dR \tag{4.20b}$$

$$F_I = \sum_{e=1}^{N} \left\{ \int_{R_e} N_I\, G\, dR + \int_{S_e} W_I\, q_n\, C_o\, dS_e - \right\} \tag{4.20c}$$

where $\Sigma_{e=1,N}$ indicates element assembly over the total number of elements N in the flow domain. For the case of type-1 boundary conditions, the terms with q_n drop from (4.20a) and (4.20c) and

prescribed concentration nodes are dropped from the matrices.

To integrate the element equations in (4.20) we employ the method of influence coefficients to avoid more costly numerical integration (Huyakorn et al., 1984). For the case of linear rectangular elements assumed here with conventional and upstream weighting interpolation functions as described in Appendix D, the matrices in (4.20) may be written as:

$$[A] = \sum_{e=1}^{N} \left\{ \langle D_x \rangle \frac{\ell}{m} [T_D^x] + \langle D_z \rangle \frac{m}{\ell} \{T_D^z] + \langle q_x \rangle \frac{\ell}{2} \left([T_V^x] + [T_V^{xu}] \right) \right.$$

$$\left. + \langle q_z \rangle \frac{m}{2} \left([T_V^z] + [T_V^{zu}] \right) + \langle H \rangle \frac{m\ell}{4} [S] \right\} \qquad (4.21a)$$

$$[B] = \sum_{e=1}^{N} \langle R^* \theta \rangle \frac{m\ell}{4} [S^*] \qquad (4.21b)$$

$$\{F\} = \sum_{e=1}^{N} \langle G \rangle \frac{m\ell}{4} \{U\} \qquad (4.21c)$$

where ℓ and m are the element dimensions in the z and x directions, $\langle \cdot \rangle$ represents values of respective variables computed at the element centroids and the influence coefficient matrices on the right hand sides are as given in Appendix E.

Time Marching Scheme

Time integration of the finite element formulation is performed using a finite difference approximation. The finite difference form of (4.19) written at time level $(k+\omega)$ is

$$[A^*]^{k+\omega}\ \{C\}^{k+1} = \{F^*\}^{k+\omega} \tag{4.22a}$$

where

$$[A^*]^{k+\omega} = \frac{[B]^{k+\omega}}{\Delta t_{k+1}} + \omega\ [A]^{k+\omega} \tag{4.22b}$$

$$\{F^*\}^{k+\omega} = \left[\frac{[B]^{k+\omega}}{\Delta t_{k+1}} - (1-\omega)\ [B]^{k+\omega}\right] \{C\}^k - \{F\}^{k+\omega} \tag{4.22c}$$

and

$$\{C\}^{k+\omega} = (1-\omega)\ \{C\}^k + \omega\ \{C\}^{k+1} \tag{4.22d}$$

where k refers to any time level at which the concentrations are known, Δt_{k+1} is the time increment at the new time step, and ω is the time weighting coefficient which normally may take values between 0.5 (Crank-Nicolson) and 1.0 (fully-implicit method). It may be noted that the final global stiffness matrix $[A^*]$ is banded but unsymmetric requiring a storage higher than that required by the flow problem.

It may also noted that the coefficient matrix contains a nonlinear term C^{p-1} in the retardation factor for the case of NH_4^+ when $p \neq 1$. A simple Picard iteration scheme is used here to handle such nonlinearity. The approach involves considering R^* to be a constant at a given iteration computed using the most recent value of C. Iterative refinement is employed to obtain an accurate solution.

Following solution of transport equations for NH_4^+-N and NO_3^--N concentrations in the system, current amounts of organic-N and cumulative denitrified-N can be computed using suitable finite difference approximations to the expressions:

$$\rho \frac{ds_{on}}{dt} = K_2 C_I \theta + K_4 C_{II} \theta - K_3 \rho S_{on} \qquad (4.23a)$$

and

$$\frac{dC_{dn}}{dt} = K_5 C_{II} \theta \qquad (4.23b)$$

where C_{dn} (ML^{-3}) is the cumulative mass of denitrified-N per porous medium volume associated with a given element or node. Note that calculation of S_{on} is necessary to proceed with time marching since it affects NH_4^+-N production whereas C_{dn} is needed only to keep a mass balance check.

A summary of the computational procedure for solving the flow and nitrogen transport problem is as follows:

1. Solve the flow equation using a suitable iterative technique as described in Chapter II.
2. Compute hydraulic fluxes and water contents at each node using the computed pressure heads from step (1).
3. Solve the convection-dispersion equation for NH_4^+ transport and iterate as needed for the case of nonlinear adsorption isotherms.
4. Repeat step (3) for NO_3^- analysis (no iteration required).
5. Compute quantities of organic-N, denitrified-N and adsorbed N remaining in the system at the current time level.
6. Perform a mass balance check if desired.
7. Proceed to the next time step via step (1).

Guidelines for selection of numerical parameters

The commonly recommended procedure for the selection of time step and element size is based on the Peclet number, P_e, and Courant number, C_r, to meet the criteria

$$\max(P_e) \leq 2 \text{ to } 3$$

$$\max(C_r) < 1$$

$$P_e = v\,\Delta l/D'$$

$$C_r = v\,\Delta t/\Delta l$$

where Δl is the largest dimension of the element and v ($=q/\theta$) is the largest of x and z direction pore water velocities for the element, $D' = D\theta$ is the largest of x and z direction dispersion coefficients for the element, and the notation max( ) designates the maximum value for the entire mesh. The absolute value of the upstream weights will depend on the Peclet number and it is common to use values of 0.5 or so with large P_e numbers. The absolute values of upstream weight parameters α and β usually range from 0.0 to 1.0 (Appendix D) representing the standard Galerkin method and the full upstream weighting method respectively. Suggested values of α and β are between 0.1 and 0.4. The procedure of evaluating the sign of upstream weights is given in Appendix D.

RESULTS AND DISCUSSION

A number of problems have been analyzed with the purpose of (1) verifying the accuracy of the numerical model by comparison with analytical and other numerical solutions, (2) determining the sensitivity of the numerical model to various parameters, and (3) determining the applicability of the model to field conditions. The results will be discussed in this section.

Example I

To assess the accuracy of the model and to determine the effectiveness of the upstream weighting technique, a simple one dimensional vertical solute transport problem with steady-state water flow was first solved for which an analytical solution may be obtained. The problem involves an initially solute free semi-infinite system to which a flux upper boundary condition is applied with unit concentration influent. Values of the parameters $v=q/\theta$, $D'=D\theta$ and R used in the problem were 2.5 cm h^{-1}, 1.0 cm^2 h^{-1} and 1.41 respectively. The maximum mesh Peclet number is 4.5. The standard Galerkin formulation with no upstream weighting ($\alpha=\beta=0$) remained free of numerical oscillations but failed to provide an accurate solution (Fig. 4.2). This result was found to be independent of time step increment. Increasing upstream weighting resulted in marked improvement in solution accuracy. The results indicate that for this problem the optimum range of upstream weights is in the range 0.1 to 0.3.

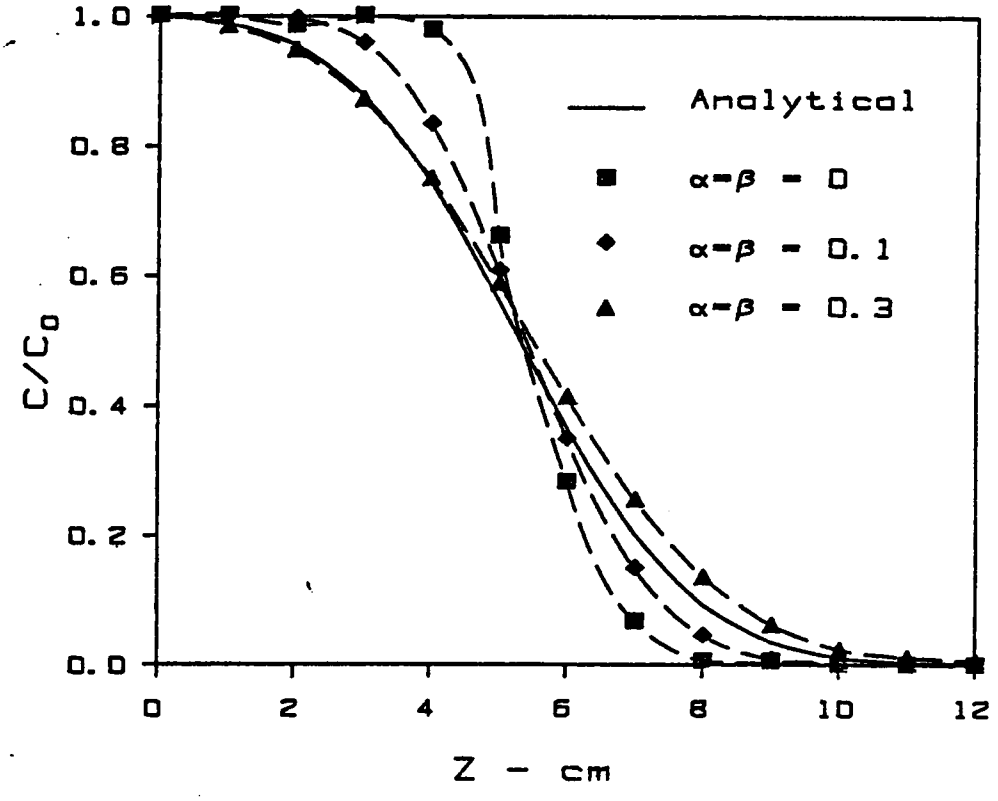

Figure 4.2 Computed relative concentrations of the 1-D simulation at 3 h for different upstream weights with Δt = 0.2 h.

Example II

In this example we consider a problem identical to that investigated analytically by Clearly and Ungs (1977) involving single species transport in a two dimensional steady-state flow domain (Fig. 4.3). The governing equation for this problem is given by (4.9) with $\phi = KC$ and with $R^* = 1$. A strip source with $C = C_o$ is applied at the upper surface of an initially solute free medium. Only half of the symmetric domain was analysed using a finite element mesh with an element Peclet number ($v\Delta L/D'$) of 4.8. The predicted relative concentrations after 1000 days along two transects taken at z = 50 ft and x = 1000 ft are compared with the analytical solution of Cleary and Ungs (1977) in Fig. 4.4. Without upstream weighting, concentrations were markedly overpredicted and the solution exhibited excessive apparent dispersion. Upstream weighting increased the accuracy substantially especially along the transect parallel to the x-axis. In this example, it was found that the optimum value of upstream weighting parameters was 0.2; further increases beyond 0.2 with the same mesh did not improve the results substantially.

Example III

In this example we analyse a one dimensional solute transport problem reported by Selim et al. (1976) involving movement of 2,4-D (2,4-Dichlorophenoxyacetic acid) in a field plot located near Quincy, Florida. The experimental work of Selim and co-workers was supported by a one dimensional finite difference model. Results of the numerical model will be used here in conjunction with the experimental data to

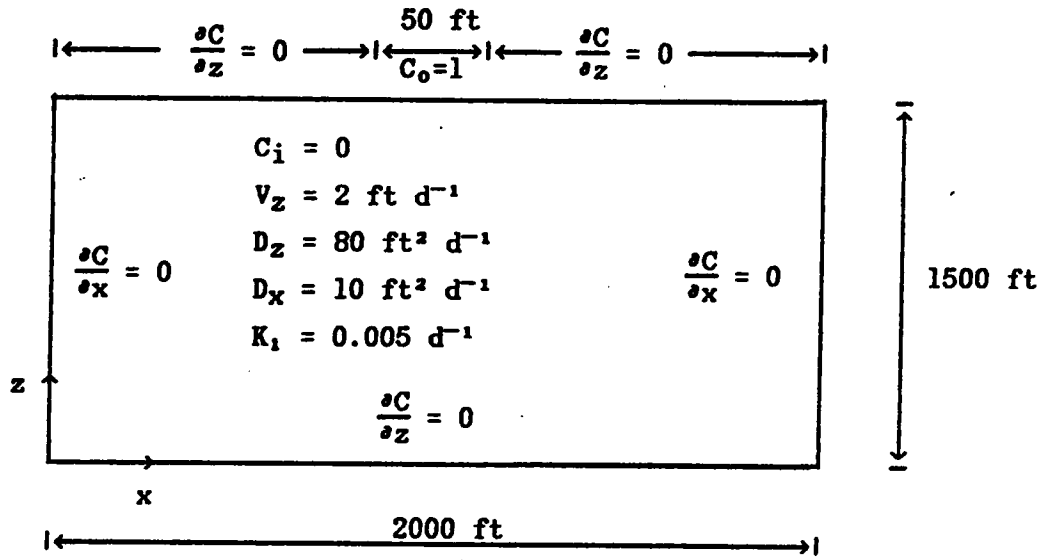

Figure 4.3 Flow and transport domain for the 2-D simulation of Example II.

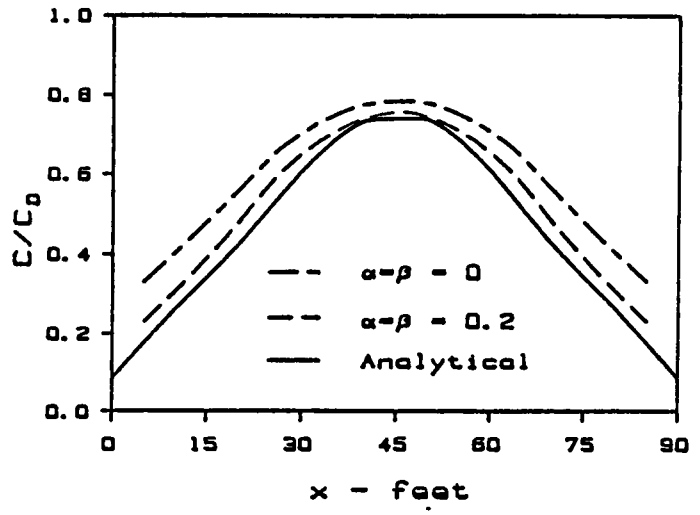

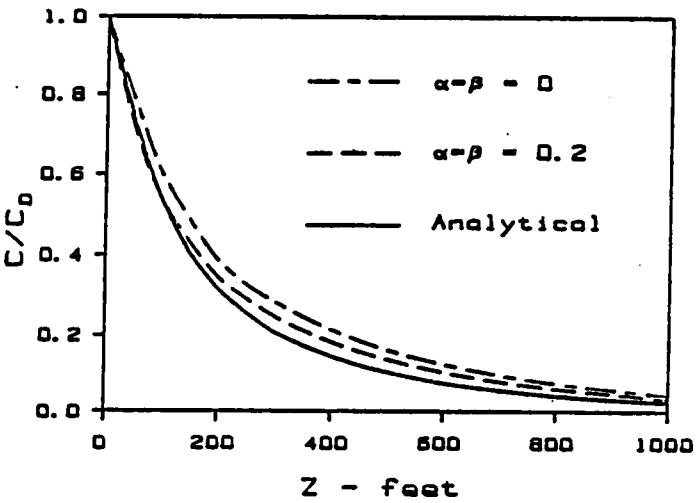

Figure 4.4 Relative concentration along different transects at 1000 days with two different upstream weights with Δt = 25 d, P_e= 4.5 for Example II.
(a) along the transect parallel to x-axis at z= 50 ft and (b) along the transect parallel to z-axis at x = 1000 ft.

validate the proposed finite element model. The field experiments consisted of two separate irrigation cycles of 2.1 and 4.1 cm h^{-1} each with a duration of 4.0 h. The initial conditions for the flow and transport problems were an equilibrium pressure distribution and zero concentration of 2,4-D. Application of 2,4-D was made with a 2 cm addition of aqueous solution having a concentration of 50 mg ml^{-1}. Adsorption of 2,4-D was described by a nonlinear Freundich isotherm with parameters k_d = 0.402 mL g^{-1} and p = 0.586. Over the relatively short time span of the experiments degradation was assumed negligible. The dispersion coefficient $D'=D\theta$ was described by $D' = 3.24 \log (q/\theta) - 0.24$. Hydraulic properties of soil in the field plot, Lakeland fine sand, which were fitted to van Genuchten's model are given in Table 4.1.

The results of the finite element analysis are compared to the experimental data of Selim for the q = 4.1 cm h^{-1} event in Fig. 4.5. Predicted wetting fronts lagged slightly behind measured fronts and were somewhat sharper but the overall accuracy of predicted water content distributions is within reasonable bounds. Water content distributions predicted by the one dimensional finite difference model of Selim were almost identical to those of the finite element model. Predicted 2,4-D movement using the finite element and finite difference models is shown in Fig. 4.5b along with measured data. Although the field data are rather sparse, they are in reasonable coincidence with predictions made by both models. Also it is noted that concentrations predicted by the one dimensional finite difference model are in close agreement with those of the two dimensional finite element model. The upstream weights used in the present analysis were 0.15 and the

Table 4.1. van Genuchten properties of the soils used in the analyses.

Problem	Soil type	K_s (cm h^{-1})	θ_s	θ_r	n	α^* (cm^{-1})
III	Fine sand	11.6	0.37	0.0671	3.2739	0.0396
IV	Sandy clay	20.0	0.42	0.0003	1.3663	0.011
V	Gravel	30.0	0.38	0.04	2.1	0.16
	Shale	0.02	0.46	0.1	1.09	0.01
	Loam	4.0	0.45	0.07	1.4	0.02
	Sand	10.0	0.41	0.06	1.7	0.145

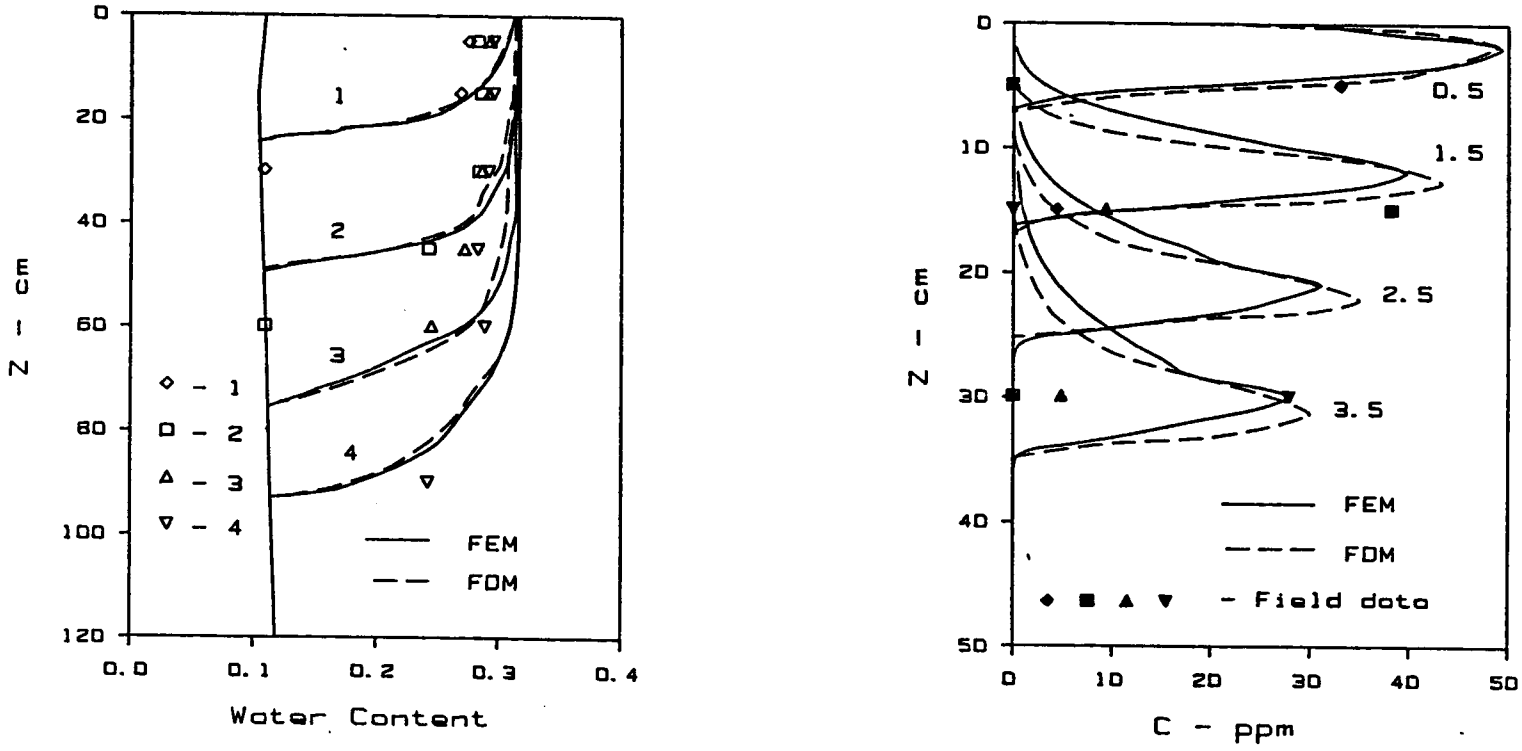

Figure 4.5 Water content and 2,4-D distribution of Example III for $q = 4.1$ cm h^{-1}. Symbols refer to field observations at times shown; (a) predicted and observed water content distributions and (b) predicted and observed 2,4-D distribution.

transport equation converged with a maximum of 4 iterations per time increment at a precision of 0.01 mg mL^{-1}. The results predicted by the finite element model have slightly lower peak concentrations and more dispersed distributions due probably to the upstream weighting, but these differences are small. Mass balance errors for the finite element analysis were less than 3.5% of the total mass in the system at any given time step. Results for the q=2.1 cm h^{-1} event (not shown) yielded very similar results to those for the q=4.1 cm h^{-1} event.

Example IV

The previous examples have verified the basic formulation and accuracy of the proposed numerical model for simple cases of single species transport. In the present example, we will investigate the sensitivity of the full multispecies N transport model to selected parameters. The soil was assumed to be a sandy clay material with van Genuchten parameters as given in Table 4.1. Initial conditions for flow correspond to hydrostatic equilibrium with a water table located 3 m below the soil surface. Boundary conditions for flow on sides AB, CD and AE (Fig. 4.6) were assumed to be zero flux type and sides AG and DF were considered to be seepage faces. On surface BC a hydraulic flux of 0.5 cm h^{-1} was applied with water containing 50 and 10 ppm of NH_4^+-N and NO_3^--N, respectively. Zero concentration gradients were assumed on other boundaries. For the base case, values of K_1, k_d and p were assumed to be 0.02 h^{-1}, 0.75 cm^3 g^{-1} and 1.0, respectively, which are within the range of reported values (Starr et al., 1974; Misra et al., 1974). Values for K_2, K_4 and K_5 were assumed to be 0.0063, 0.0063 and 0.002 h^{-1} also in keeping with values reported

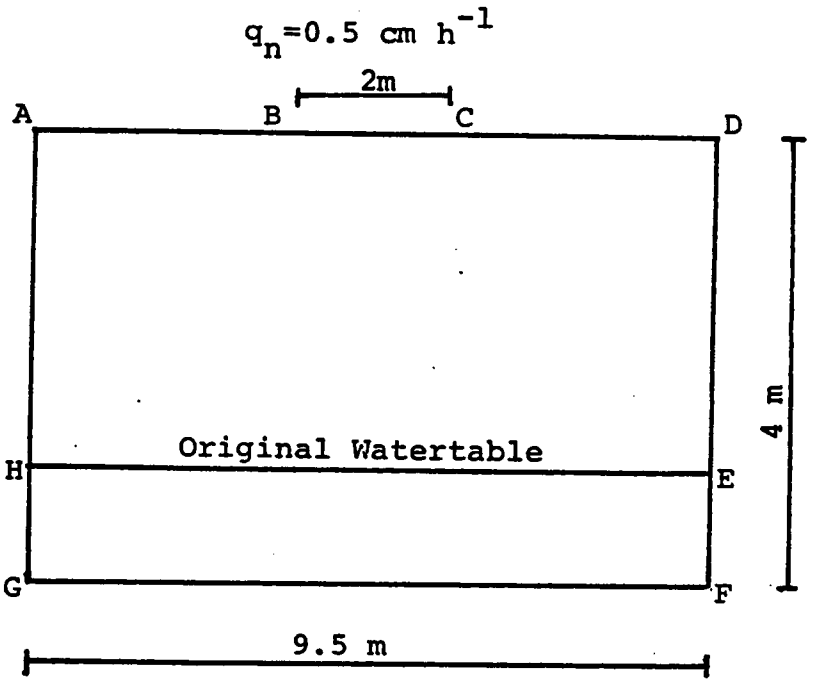

Figure 4.6 Flow and transport domain used in Example IV.

in the literature for subsurface conditions (Stajanovic and Broadbent, 1956; Mehran and Tanji, 1974; Misra et al., 1974) and K_3 was assumed to be zero. Values of ρ, D_O, λ_L, and λ_T were taken as 1.4 g cm^{-3}, 0.12 cm^2 h^{-1}, 1.0 cm and 0.2 cm (Starr et al., 1974; Gureghian and Cleary, 1979). Upstream weights for all simulations were kept constant at 0.15 after preliminary analyses indicated little change in concentration distributions with higher weights.

The first set of simulations were conducted to evaluate the effects of nitrification rate K_1 on model predictions. Simulations were performed for K_1 values of 0.005 and 0.1 h^{-1} in addition to the base value of 0.02 h^{-1}. Since nitrate is the species of greatest environmental importance, we concentrate first on its behavior. As most of the nitrogen entering the system is in the NH_4^+ form, it is not surprising that peak $NO3^-$ concentrations increase substantially with increasing K_1 (Fig. 4.7). Peak locations on the other hand are essentially unaffected by K_1.

Comparisons of cumulative mass distributions of NH_4^+-N, NO_3^--N and organic-N as a function of time are shown for the various K_1 in Fig. 4.8. Here NH_4^+-N mass refers to the total mass in both solution and adsorbed phases. As K_1 increases total NH_4^+ decreases and NO_3^- increases due to nitrification. Organic-N increases with increasing K_1 due to greater net organic immobilization of NO_3^--N than NH_4^+-N since the former is non-adsorbed and thus more readily available for microbial utilization. At any given time the fraction of NH_4^+ in solution was only 20% of the total mass of NH_4^+ in the system. Also it should be noted that part of the total N mass corresponding to denitrified-N

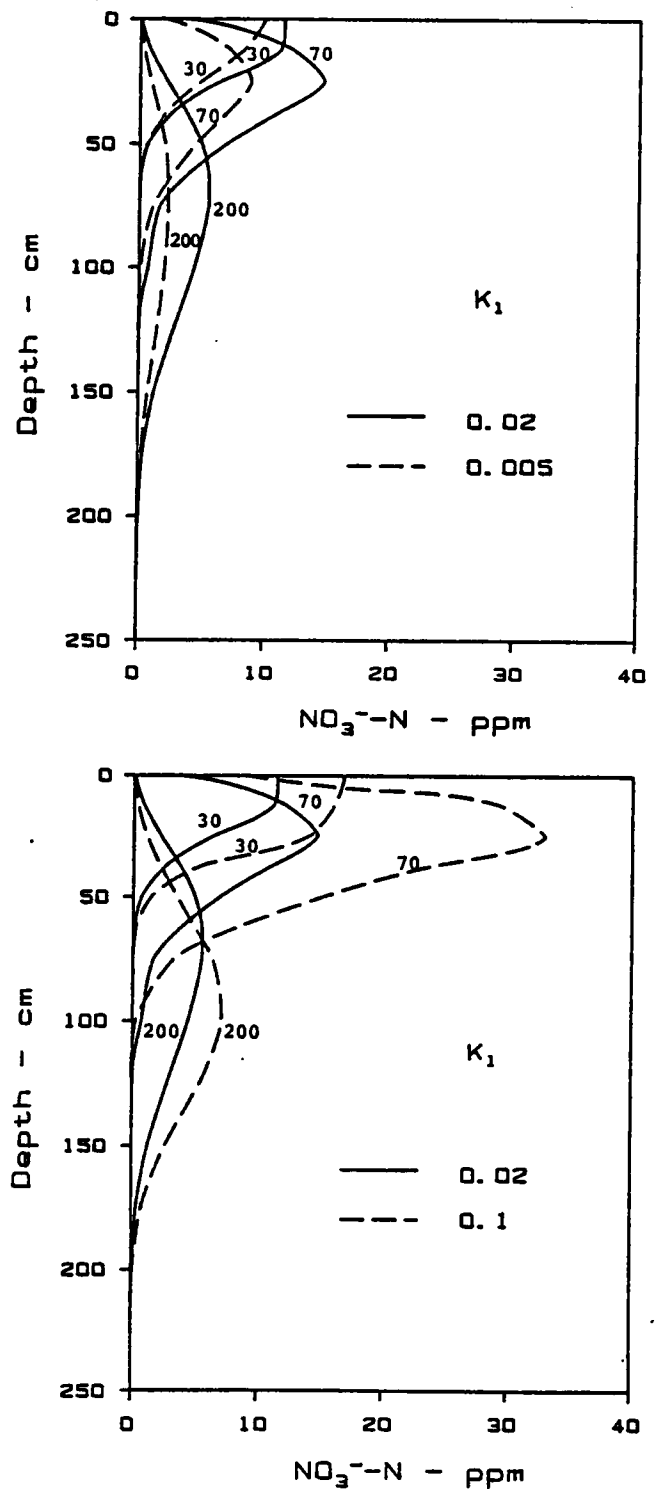

Figure 4.7 Distribution of NO_3^--N concentration with depth on center line for different K_1 values.

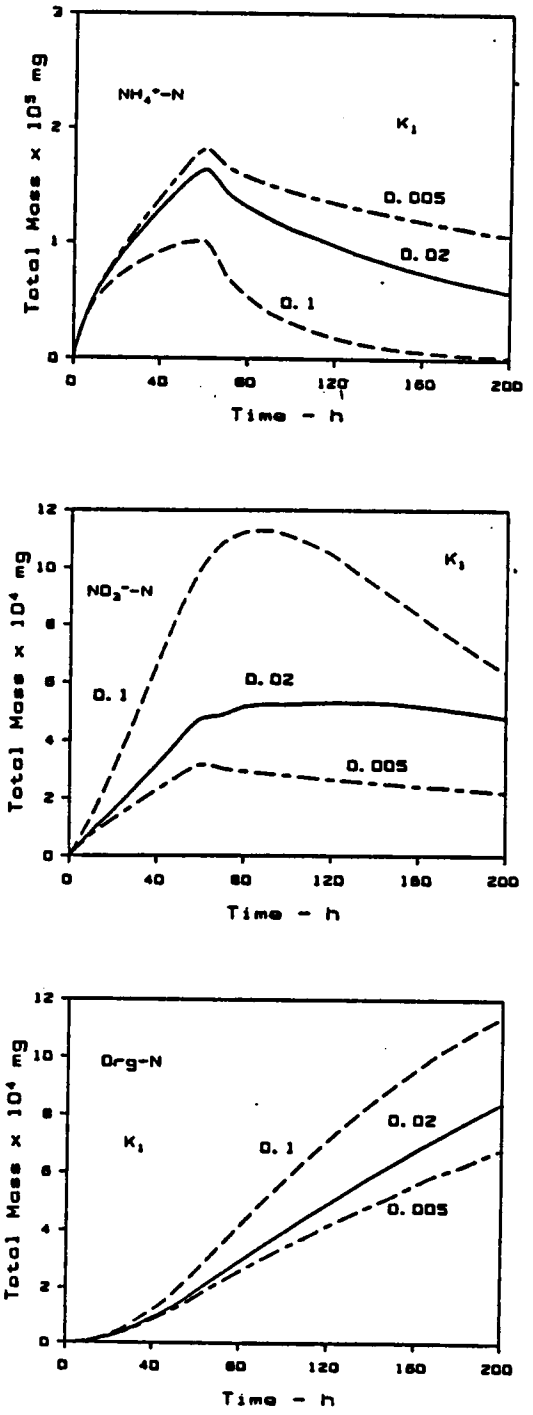

Figure 4.8 Cumulative mass distribution of various nitrogen species for different K_1 values.

is not shown in Fig. 4.8.

In the second set of simulations we focus on the sensitivity to k_d using k_d values of 0.2 and 1.5 ml g^{-1} in addition to the base value of 0.75 ml g^{-1}. The results in Fig. 4.9 show that retardation of NH_4^+ associated with increasing k_d both retards the NO_3^- peak and reduces its magnitude, although the sensitivity is fairly mild in comparison to effects of K_1. The effects of k_d on cumulative mass distributions of the various N species (Fig. 4.10) are inverse to those of K_1. Total (solution and adsorbed phase) NH_4^+-N increases and NO_3^--N decreases with increasing k_d owing to reduced nitrification due to sheltering of ammonium from microbial activity in the adsorbed state. Reduced solution phase NH_4^+-N with increasing k_d also results in diminished immobilization and hence to lower organic-N mass.

In the last set of simulations for this problem we investigate the effects of NH_4^+ isotherm nonlinearity on N transport and transformations by varying the Freundlich exponent p between 0.8 and 1.2. Solution of the nonlinear NH_4^+ transport equation required an average of 4 iterations to reach convergence with a precision of 0.01 ppm (Fig. 4.11). Increasing p has the effect of increasing NH_4^+ adsorption and hence results in qualitatively similar trends in NO_3^- distributions with depth (Fig. 4.11) and cumulative NO_3^--N, NH_4^+-N and organic-N masses (Fig. 4.12) as were observed for k_d previously. Due to the exponential effect of p on NH_4^+ adsorption, the relative sensitivity of simulation results to it are greater than to k_d; however, since the feasible range in p is much narrower uncertainty in the latter is likely to induce comparatively less output uncertainty.

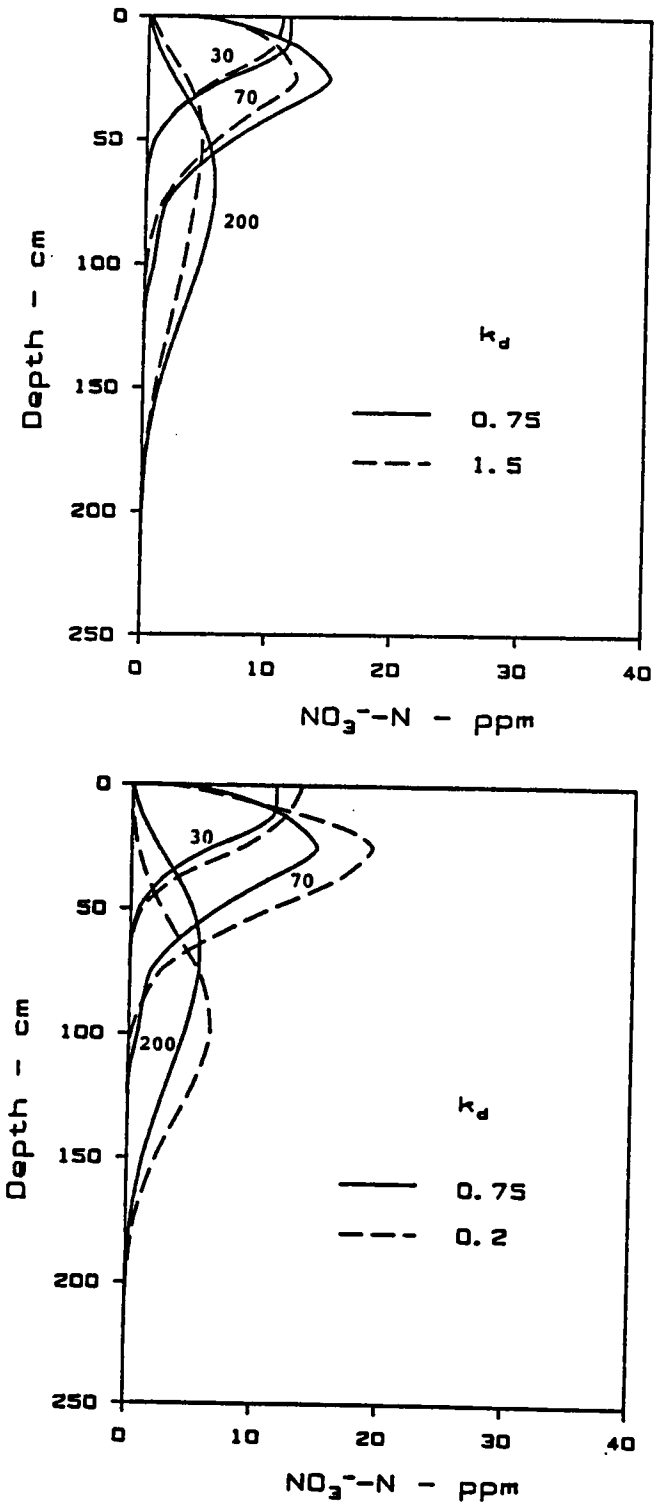

Figure 4.9 Distribution of NO_3^--N concentration with depth on center line for different K_d values.

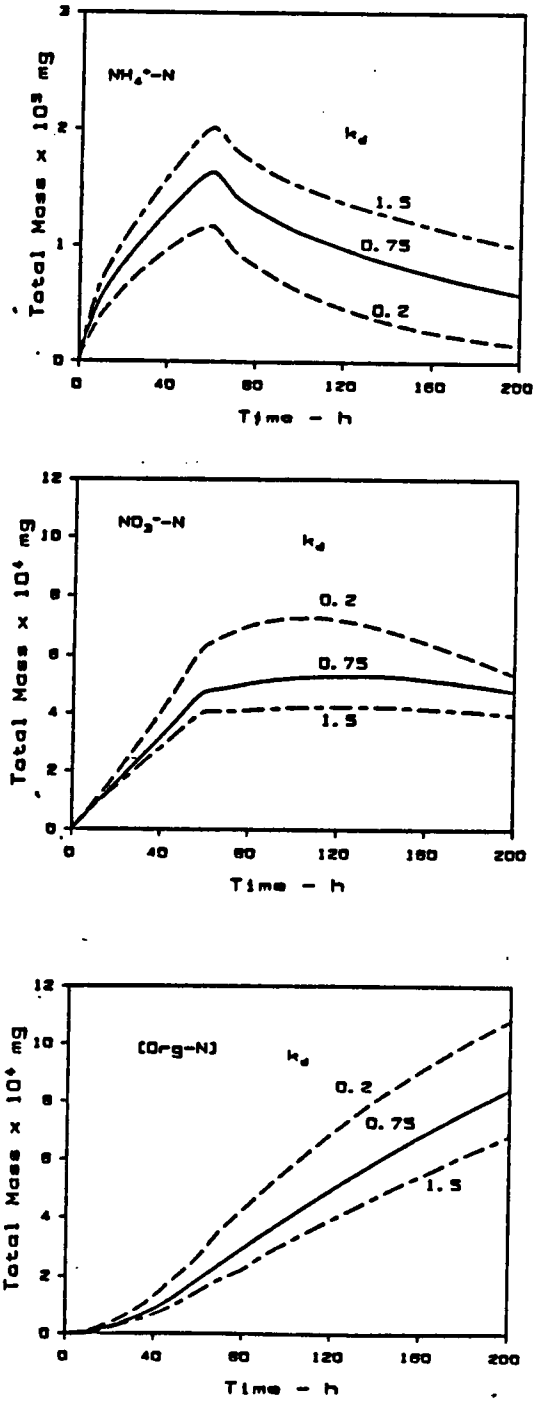

Figure 4.10 Cumulative mass distribution of various nitrogen species for different K_d values.

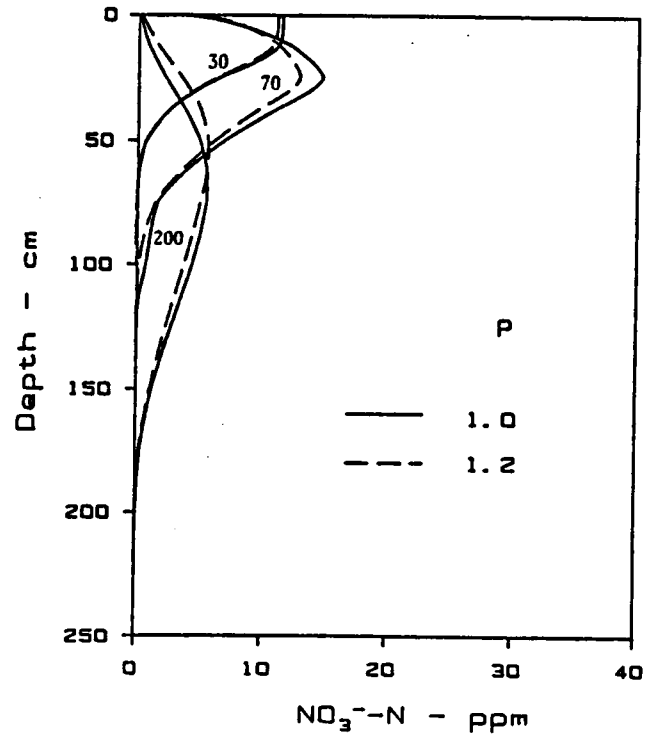

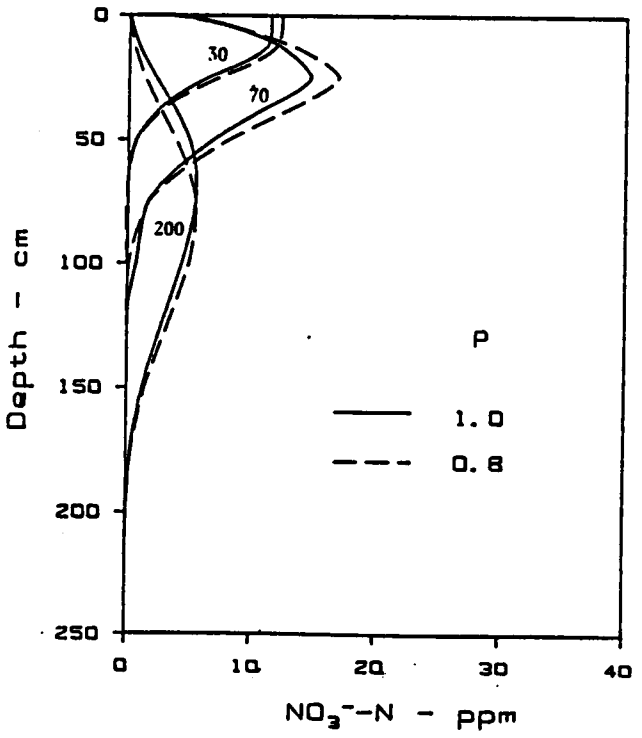

Figure 4.11 Distribution of NO_3^--N concentration with depth on center line for different p values.

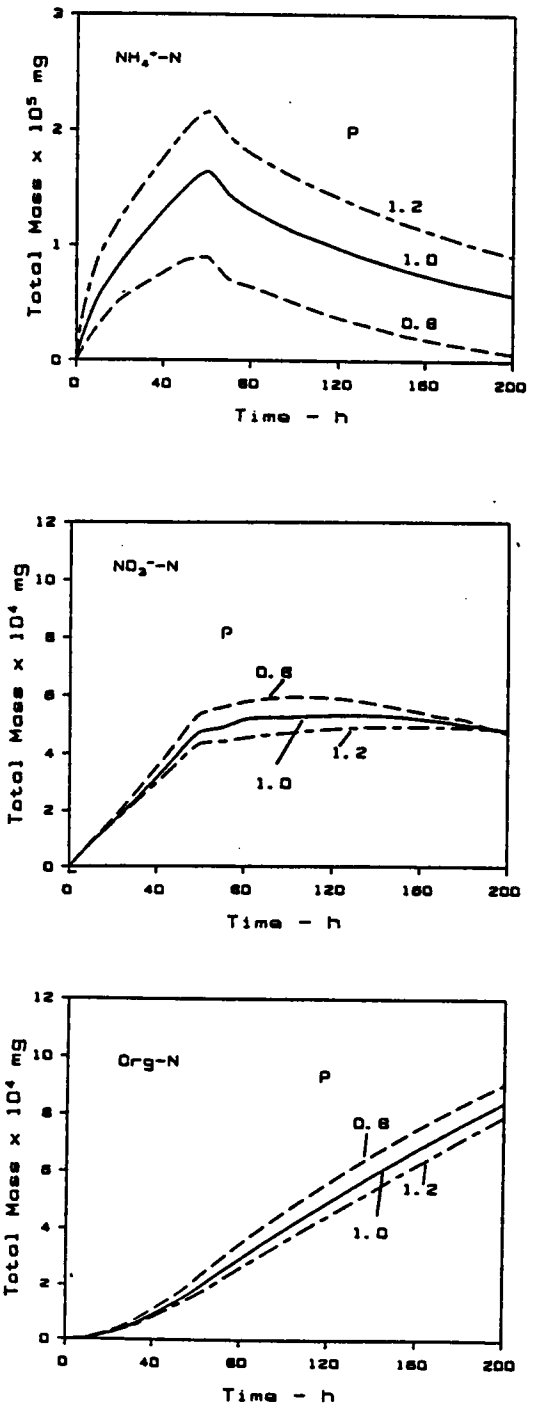

Figure 4.12 Cumulative mass distribution of various nitrogen species for different p values.

Furthermore, although the effects of varying p and k_d over the chosen ranges are very nearly identical for cumulative NH_4^+ mass, sensitivity of the environmentally important NO_3^- species as well as organic-N to p are lower than observed for k_d.

Example V

We turn next to an application of the model to an actual field problem involving nitrogen movement from an operating domestic wastewater drainfield located in Front Royal, Virginia. The system consists of a gravel bed with drain lines laid on an elevated sand mound constructed over the original shale soil of very low permeability (Fig. 4.13). French drains were installed on sides AC and DE to prevent surface water ponding. Solution sampling devices were installed at depths 0, 15 and 50 cm below the bottom of the sand mound at three locations along the centerline of the mound (i.e., perpendicular to the plane of the numerical analysis). Measurements of solution phase NH_4^+-N and NO_3^--N from samples on three dates were available for comparison with the numerical simulations.

For simulation purposes, an applied hydraulic flux of 0.0126 cm h^{-1} corresponding to the mean annual rainfall rate in northern Virginia was applied continuously along the upper boundary (A-C-F-E). Based on observations at the site the water table was taken coincident with the original ground surface just prior to system startup and the initial pressure distribution was assumed to be at hydrostatic equilibrium. French drains at the extremities of the system (A-C and E-D) were treated as seepage faces and the lower surface (C-D) was regarded as

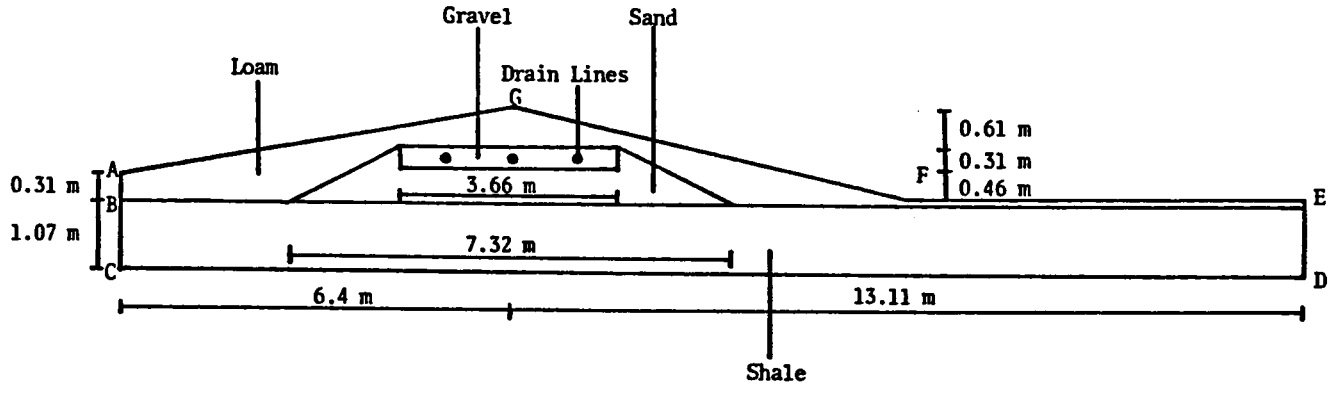

Figure 4.13 Cross-sectional view of the drainfield site described in Example V.

impermeable. The effluent dosage at the drain lines as estimated from data on household water use was taken to be 5.0 cm^3 cm^{-1} h^{-1} and average concentrations of NH_4^+-N and NO_3^--N were taken as 20 and 0.2 ppm, respectively, based on analyses of the effluent. Initial concentrations of NH_4^+-N, NO_3^--N and organic-N in the system were assumed to be 0.5, 0.1 and 0.1 ppm, respectively.

Hydraulic properties of the shale subsoil, sand and gravel used in the simulations (Table 4.1) were based on measurements of saturated conductivity and estimates of retention curve characteristics via correlations with particle size data. The average bulk density of the soil was estimated as 1.5 g cm^{-3}, first order rate coefficients K_2, K_4 and K_5 were taken to be 0.007, 0.005 and 0.006 h^{-1}, and parameters D_O, λ_L and λ_T were assumed to be 0.12 cm^2 h^{-1}, 1.0 cm and 0.2 cm (Starr et al., 1974, Selim and Iskandar, 1981a and b). Here K_3 was assumed to be zero. The foregoing parameters were selected as typical of subsurface conditions at this scale of observation (e.g., Misra et al., 1974). Ammonium will be assumed to follow a linear adsorption isotherm.

Since it was shown previously that probable variations in the nitrification rate constant K_1 and partition coefficient k_d have significant effects on N transport, a number of sets of these parameters were selected in the analysis. Results will be shown for two sets of parameters that corresponded most closely with field observations. The two cases will be designated as Simulation I for which (K_1, k_d) = (0.02 h^{-1}, 1.7 ml g^{-1}) and Simulation II for which (K_1, k_d) = (0.03 h^{-1}, 1.5 ml g^{-1}).

Transient flow and transport analyses were carried out for a period of 90 days with steady state flow conditions being reached in about 38 days. Predicted initial and steady state water content distributions at the center and the left drainline locations showed large vertical variations due to the extreme differences in material properties in the different layers (Fig. 4.14). Comparisons of predicted and observed NH_4^+-N and NO_3^--N concentrations at the three measurement depths are shown in Figs. 4.15a to 4.15c and 4.16a to 4.16c. Multiple data points at each time and depth for which samples were taken correspond to the different sampling locations perpendicular to the plane of the numerical analysis (data were available from 3 locations except in a few instances where various mishaps precluded sampling or analysis). It is apparent that scatter between data for "replicate" times and depths is substantial for NH_4^+ especially and generally irregular suggesting a random component due to sampling and analytical error in addition to possible "real" effects due to spatial and temporal variability. The numerical simulation results generally fall within the range of the experimental data. A notable exception occurs for NH_4^+ at short times which exhibits a tendency for earlier increases in concentration than predicted while early time NO_3^- behavior is closely predicted. A possible explanation for this is that it takes some time for microbial activity to acclimate at system startup resulting in a gradual increase in the nitrification rate coefficient with time.

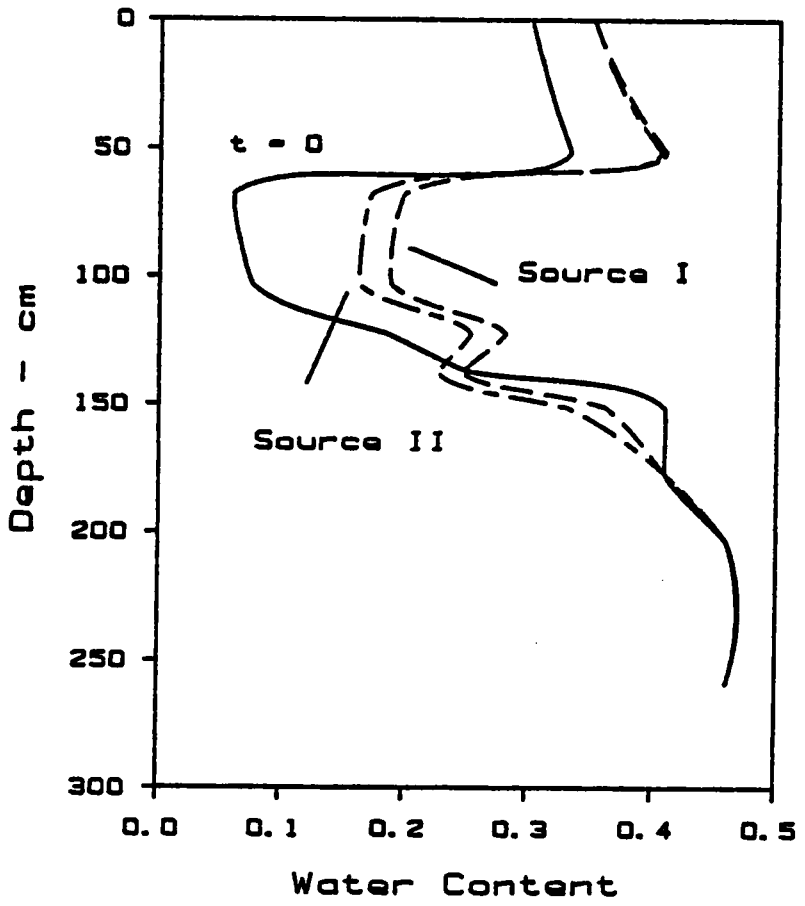

Figure 4.14 Predicted steady state water content distribution along the drain lines in Example V. Sources I and II denote the drain lines at the center and left of center of the domain.

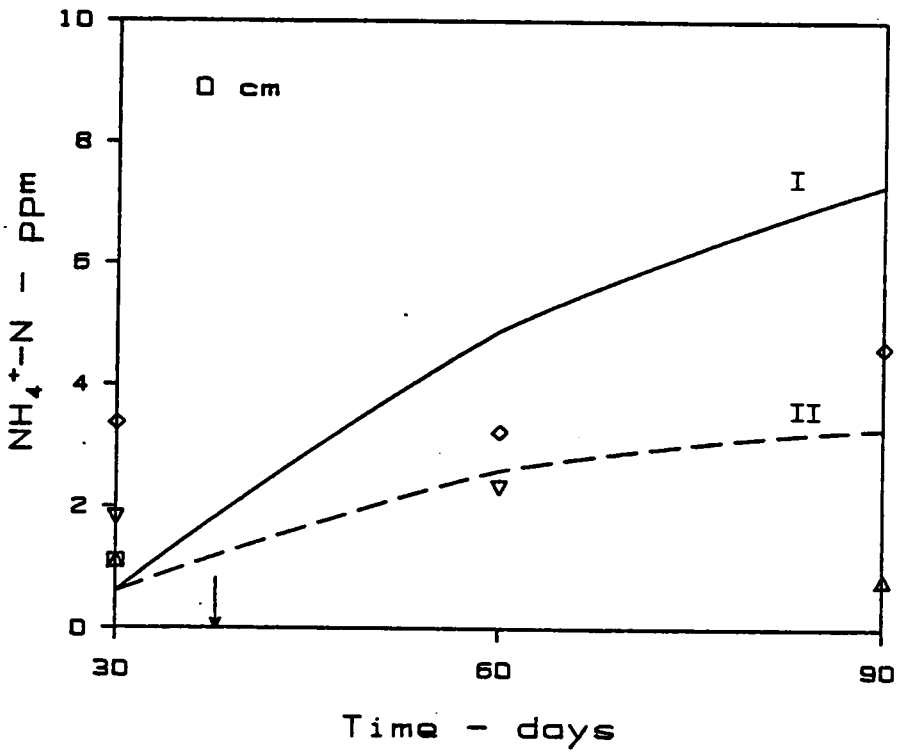

Figure 4.15a Predicted and observed NH_4^+-N concentrations along the center line of the drainfield site at 0 cm below the sand-shale interface. Vertical arrow indicates the time of attainement of steady state condition.

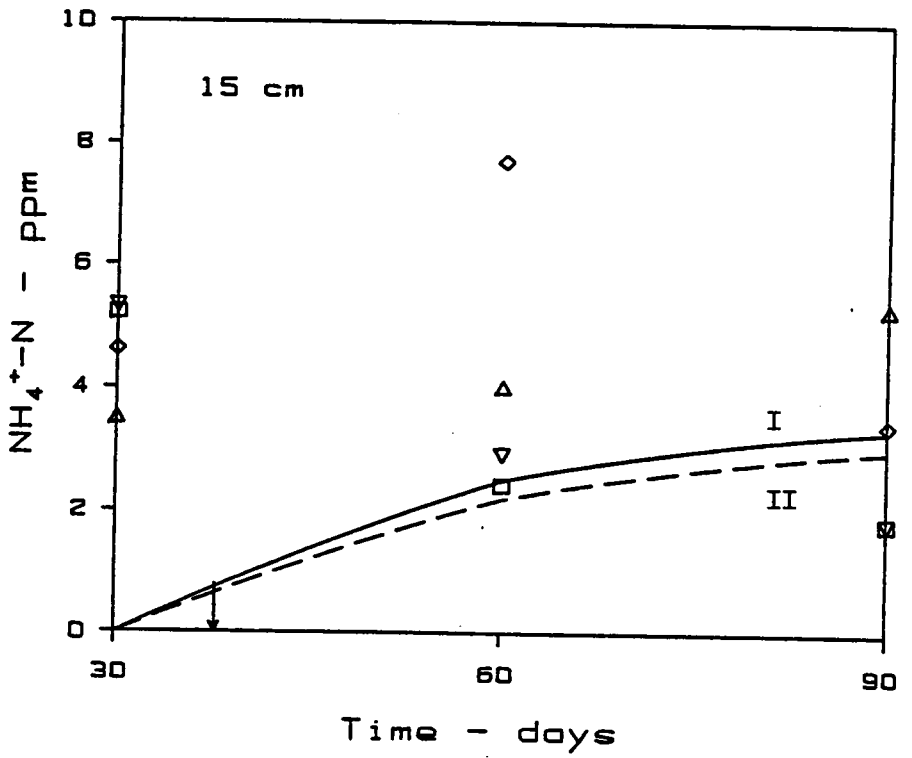

Figure 4.15b Predicted and observed NH_4^+-N concentrations along the center line of the drainfield site at 15 cm below the sand-shale interface. Vertical arrow indicates the time of attainement of steady state condition.

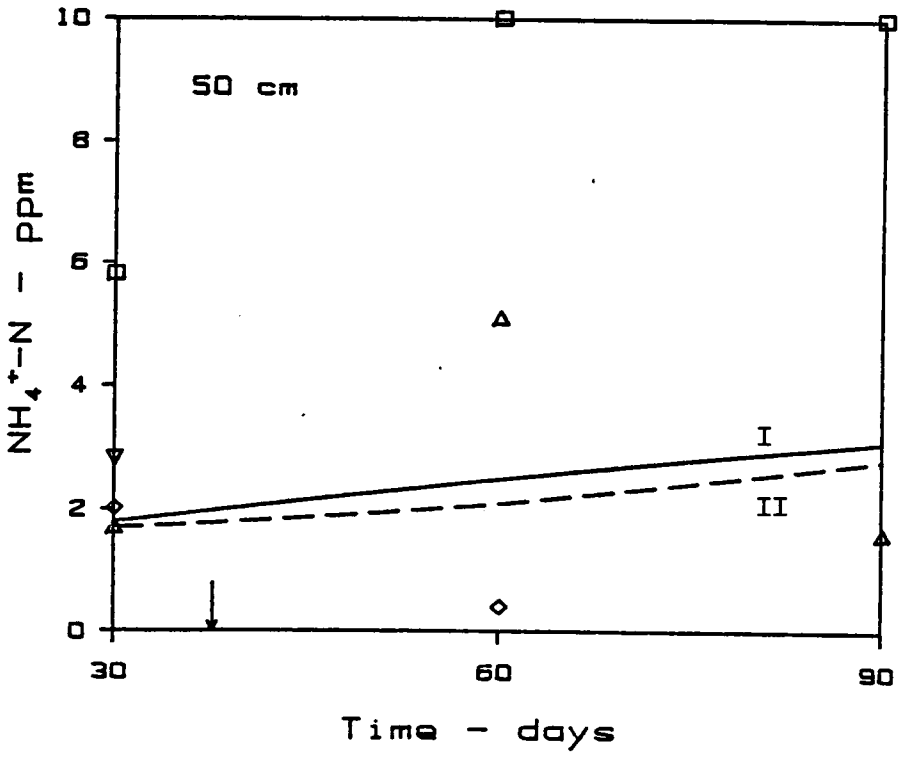

Figure 4.15c Predicted and observed NH_4^+-N concentrations along the center line of the drainfield site at 50 cm below the sand-shale interface. Vertical arrow indicates the time of attainement of steady state condition.

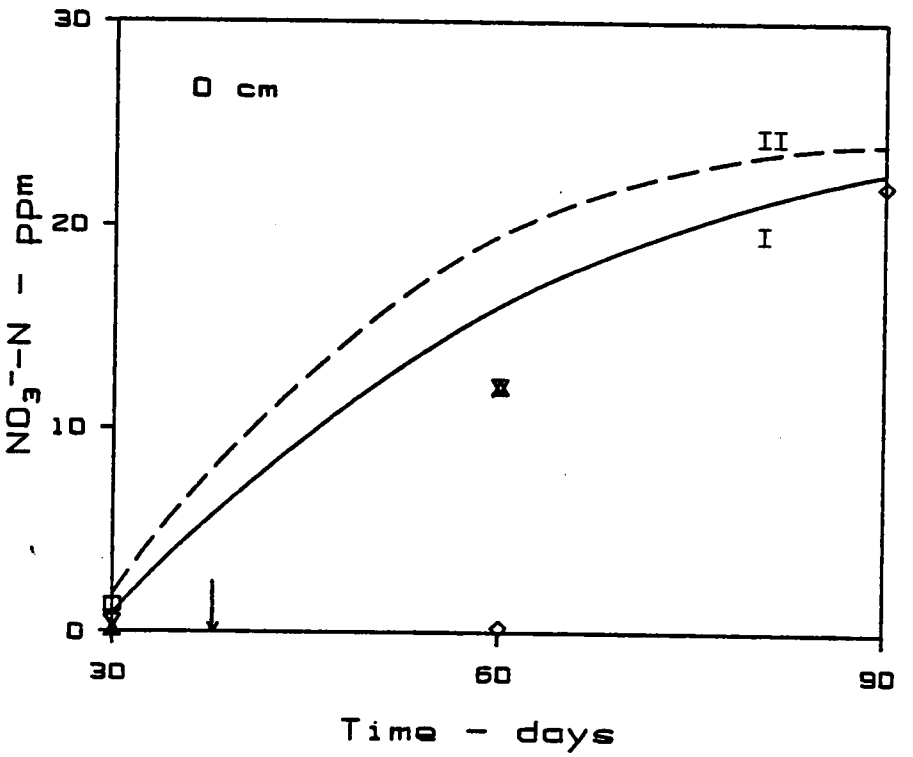

Figure 4.16a Predicted and observed NO_3^--N concentrations along the center line of the drainfield site at 0 cm below the sand-shale interface. Vertical arrow indicates the time of attainement of steady state condition.

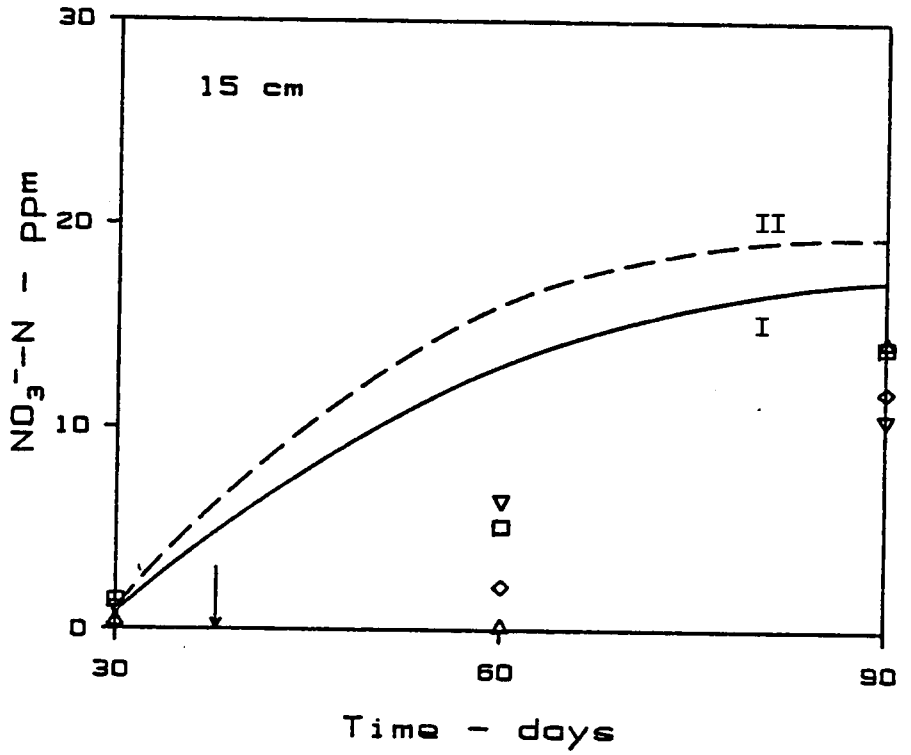

Figure 4.16b Predicted and observed NO_3^--N concentrations along the center line of the drainfield site at 15 cm below the sand-shale interface. Vertical arrow indicates the time of attainement of steady state condition.

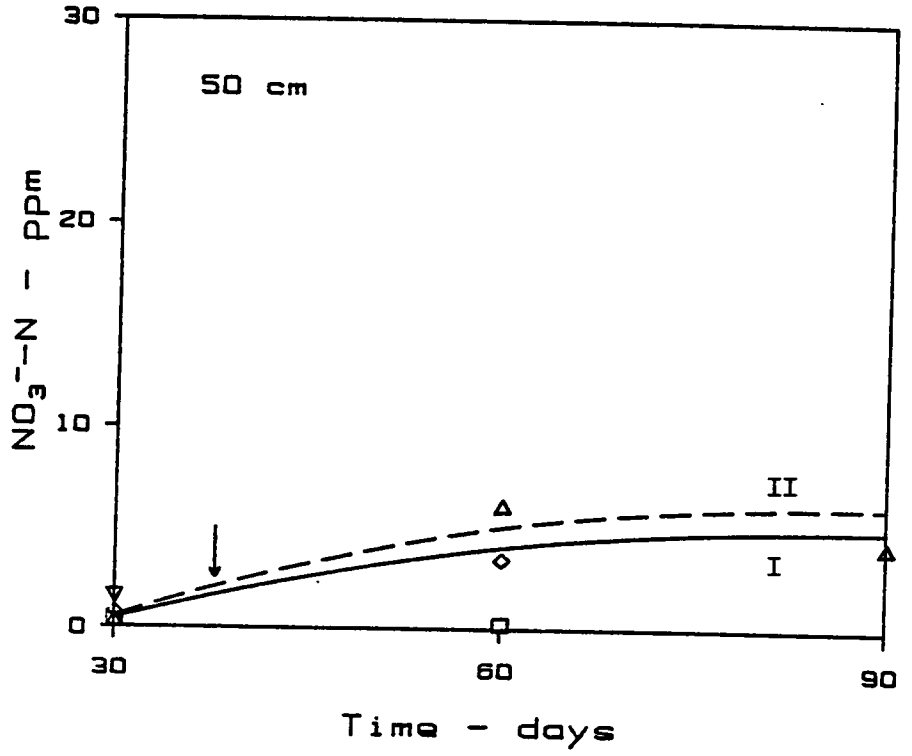

Figure 4.16c Predicted and observed NO_3^--N concentrations along the center line of the drainfield site at 50 cm below the sand-shale interface. Vertical arrow indicates the time of attainement of steady state condition.

CONCLUSIONS

A two dimensional finite element model has been described for the prediction of nitrogen species transformations and transport in unsaturated soil and groundwater. Nitrification, denitrification, mineralization and immobilization are treated as first order kinetic processes; plant uptake of NH_4^+ and NO_3^- are treated as first order processes; and NH_4^+ adsorption is assumed to be instantaneous and to follow a Freundlich type isotherm. Simultaneous transport of solution phase NH_4^+ and NO_3^- are described by convection-dispersion equations solved by an upstream weighted residual finite element technique which is shown to provide accurate solutions even under conditions of high element Peclet numbers. A sensitivity study on the model parameters showed that first order nitrification rate to have the greatest effects on the computed results and to a lesser extent by the nonlinear isotherm parameters k_d and p used to describe the adsorption of NH_4^+.

Application of the model to a real field problem involving a subsurface wastewater injection system has illustrated the utility of the model and demonstrated that in the absence of detailed site specific information on soil properties and kinetic parameters, a good approximation of the nitrogen movement can be obtained.

REFERENCES

Bear, J., 1975. Dynamics of fluids in porous media, American Elsevier, New York, 764 pp.

Cho, C. M., 1971. Convective transport of ammonium with nitrification in soil, Can. J. Soil, 52:339-350.

Cleary, R. W. and Ungs, M. J., 1977. Analytical models for groundwater pollution and hydrology, Rep. 78-WR-15, Dep. Civ. Eng., Princeton University, Princeton, N.J., 166 pp.

Duffy, J., Chung, C., Boast, C. and Franklin, M., 1975. A simulation model for biophysiochemical transformations of nitrogen in tile-drained corn belt soils, J. Environ. Qual., 4:477-486.

Gureghian, A. B., Ward, D. S. and Cleary, R. W., 1979. Simultaneous transport of water and reacting solutes through multilayered soils under transient unsaturated flow conditions, J. Hydrol., 41:253-278.

Huyakorn, P. S. and Nilkuha, K., 1979. Solution of transient transport equation using an upstream finite element scheme, Appl. Math. Modelling, 1:187-195.

Huyakorn, P. S., Thomas, S. D. and Thompson, B. M., 1984. Techniques for making finite elements competetive in modeling flow in variably saturated porous media, Water Resour. Res., 20:1099-1115.

Kaluarachchi, J. J. and Parker, J. C., 1987. Finite element analysis of water flow in variably saturated soil, J. Hydrol., 90:1269-291.

Mehran, M. and Tanji, K. K., 1974. Computer modeling of the nitrogen transformations in soils, J. Environ. Qual., 3:391-396.

Millington, R. J., 1959. Gas diffusion in porous media. Science, 130:100-102.

Misra, C. D., Nielson, D. R. and Biggar, J. W., 1974. Nitrogen transformation in soil during leaching: I, II, and III, Soil Sci. Soc. Am. Proc., 38:289-304.

Selim, H. M., Mansell, R. S. and Elzeftawy, A. A., 1976. Distribution of 2,4-D and water in soil during infiltration and redistribution. Soil Sci., 121:176-183.

Selim, H. M. and Iskandar, I. K., 1981a. Modeling nitrogen transport and transformations in soils: Theoretical considerations, Soil Science, 131:233-241.

Selim, H. M. and Iskandar, I. K., 1981b. Modeling nitrogen transport and transformations in soils: Validation, Soil Science, 131:303-312.

Stanford, G., Vander Pol and Dzienia, S., 1975. Denitrification rates in relation to total and extractable soil carbon. Soil Sci. Soc. Am. Proc., 39:284-289.

Starr, J. L., Broadbent, F. E. and Nielson, D. R., 1974. Nitrogen transformations during continuous leaching. Soil Sci. Soc. Am. Proc., 38:283-289.

Stojanovic, B. J. and Broadbent, F. E., 1956. Immobilization and mineralization rates of nitrogen during decomposition of plant residues, Soil Sci. Soc. Am. Proc., 20:213-218.

van Genuchten, Th. M., 1980. A closed-form equation for predicting the hydraulic conductivity of unsaturated soils. Soil Sci. Soc. Am. J., 44:892-898.

van Veen, J. A. and Frissell, M. J., 1976. Computer simulation model for the behavior of nitrogen in soil and leaching to groundwater. PUDOC, Wageningen.

CHAPTER V

NITROGEN TRANSPORT UNDER HYSTERETIC CONDITIONS

ABSTRACT

A two-dimensional finite element model was used to predict multispecies transport and transformation of nitrogen accompanying unsaturated flow with hysteresis and air entrapment. Results show that under potential-type boundary conditions, hysteresis substantially influences transport predictions due largely to air entrapment effects. Nonhysteretic simulations using main wetting curve parameters corresponded much more closely to hysteretic results that those using main drainage relations. For contaminant introduction via buried constant strength line sources, hysteresis had little effect on predictions of N transport.

INTRODUCTION

Disposal of secondary wastewater via direct land application or in subsurface drainfields is a potential source of excessive nitrogen loadings to unconfined aquifers. Nitrogen transport is complicated by the occurrence of transformations between various species within the unsaturated zone. These transformation processes are generally mediated by microbial populations. Furthermore, under unsaturated conditions air entrapment and hysteresis in saturation-pressure relationships may substantially affect the accuracy of predictions of

flow, which in turn impinges on transport predictions. It has also been shown in Chapter III that hysteresis effects are highest with potential type boundary conditions and almost negligible with flux-controlled boundary conditions. This is an important consideration with regard to solute transport simulations because primary variables associated with transport studies are water contents and water fluxes. In cases where multi species transport and transformations are simulated with kinetic coeffcients dependent on the water content of the soil, hysteresis will play an important role in determining the actual distribution of various species with time in the system. These factors suggest that hysteresis to be important in transport studies but very few studies have been conducted in attempting to predict the solute movement under such conditions. Previous studies of solute transport with hysteretic flow (Pickens et al., 1979; Pickens and Gillham, 1980; Jones and Watson, 1987) have been limited to cases without air entrapment and to one dimensional scenarios for single species transport. The objectives of the present study are to evaluate the effects of hysteresis with air entrapment on multispecies nitrogen transport. Since the effects of hysteresis is almost negligible with flux controlled boundary conditions attention will be focused mainly on potential type boundary conditions.

THEORY AND ANALYSIS

Nitrogen Speciation Model

The nitrogen speciation model assumed in this study is identical to that described in Chapter IV and given Fig. 4.1. As described earlier, it is assumed that first-order kinetics to hold between solution phase NH_4^+-N and NO_3^--N and organic-N (solid phase) and denitrified-N (gaseous phase) with rate constants K_1 - K_5. Instantaneous and reversible adsorption of NH_4^+-N is assumed here to follow a linear isotherm and NO_3^--N adsorption is regarded as negligible. Also for the simulations described in this study, plant uptake of nitrogen is assumed to be zero.

Analysis of Flow and Transport

Flow of water in an incompressible and variably saturated two-dimensional porous medium under isothermal conditions is described by Richard's equation and given in detail by (2.1) subjected to initial and boundary conditions given by (2.2). The solution of this equation requires numerical solution due to the extremely nonlinear soil hydraulic properties. In this study, we used a Galerkin finite element solution incorporating the method of influence coefficients to avoid costly numerical integration. Complete details of the finite element model are given in Chapter II.

The simplified convective-dispersive transport equation for species i may be written in the form:

$$R_i\theta \frac{\partial C_i}{\partial t} - \frac{\partial}{\partial x}\left[D_x \frac{\partial C_i}{\partial x}\right] - \frac{\partial}{\partial z}\left[D_z \frac{\partial C_i}{\partial z}\right] + q_x \frac{\partial C_i}{\partial x} + q_z \frac{\partial C_i}{\partial z} + Q^*(C_i - C_i^*) + \phi_i = 0 \qquad (5.1)$$

where C_i is the concentration of the species i in solution (M L^{-3}), θ is the water content, q_x and q_z are flow velocities along the principal x and z directions, D_x and D_z are dispersion coeffcients in the x and z directions, R_i is a retardation factor, Q^* and C_i^* are flow rate and concentration of species i in a line source and ϕ_i is the net species transformation rate. Defining C_I and C_{II} to be concentrations of NH_4^+-N and NO_3-N, respectively, S_{on} to be the organic-N fraction (MM^{-1}) and ρ to be the soil bulk density, net transformation rates for NH_4^+-N and NO_3^--N, respectively, are:

$$\phi_I = K_1 C_I \theta + K_2 C_I \theta - \rho K_3 S_{on} \qquad (5.2a)$$

$$\phi_{II} = K_4 C_{II} \theta + K_5 C_{II} \theta - K_1 C_I \theta \qquad (5.2b)$$

The solution of (5.1) for C_I and C_{II} is obtained by a procedure similar to that for the flow equation except that an upstream weighting technique is utilized to avoid numerical difficulties associated with low dispersion coefficients. Transport of components other than NH_4^+-N and NO_3^--N are not considered. Complete details of the finite element analysis for the N transport model are given in Chapter IV.

Hysteresis Model

We will employ the hysteretic soil hydraulic property model of Kool and Parker (1987). The hysteretic model is based on van Genuchten's (1980) parametric relations and takes the form

$$\theta^d(h) = \begin{cases} \theta_r + (\theta_s{}^d - \theta_r)[1+|\alpha^d h|^n]^{-m} & h < 0 \\ \theta_s{}^d & h \geq 0 \end{cases} \qquad (5.3a)$$

$$\theta^w(h) = \begin{cases} \theta_r + (\theta_s{}^w - \theta_r)[1+|\alpha^w h|^n]^{-m} & h < 0 \\ \theta_s{}^w & h \geq 0 \end{cases} \qquad (5.3b)$$

where h is the pressure head, θ_s is the saturated water content, θ_r is the residual water, α and n are shape constants and $m = 1 - 1/n$. The superscript w or d denotes variables pertaining to either the main wetting or main drainage branch of the θ-h relationship, respectively. Hysteresis in hydraulic conductivity, K, versus water content is assumed negligible. Complete details of the hysteresis model are given by Kool and Parker (1987).

NUMERICAL SIMULATIONS

Two examples will be considered here for the flow domain illustrated in Fig. 5.1. The watertable is located 1.5 m below the soil surface and the two end boundaries were assumed to be seepage faces. The assumed soil hydraulic properties are shown in Fig. 5.2 corresponding to values of parameters $\theta_s{}^d$, $\theta_s{}^w$, θ_r, n, α_w and α_d equal to 0.45, 0.38, 0.07, 1.4, 0.045 and 0.02 cm^{-1}, respectively. The isotropic saturated hydraulic conductivity K_s is 3.0 cm h^{-1}.

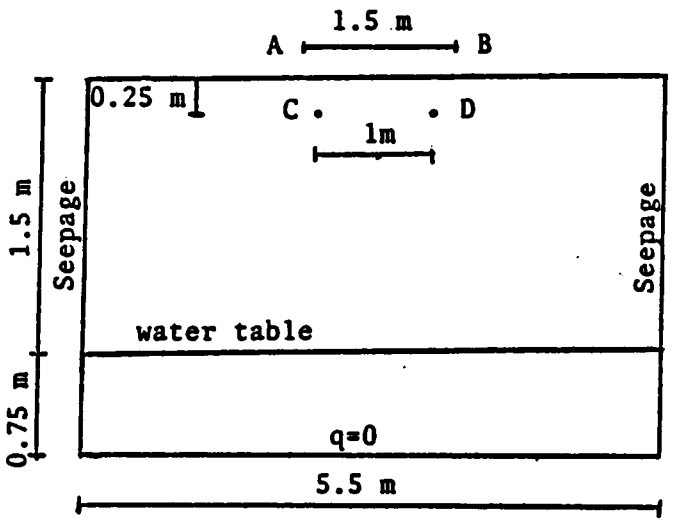

Figure 5.1 Flow domain used in simulations.

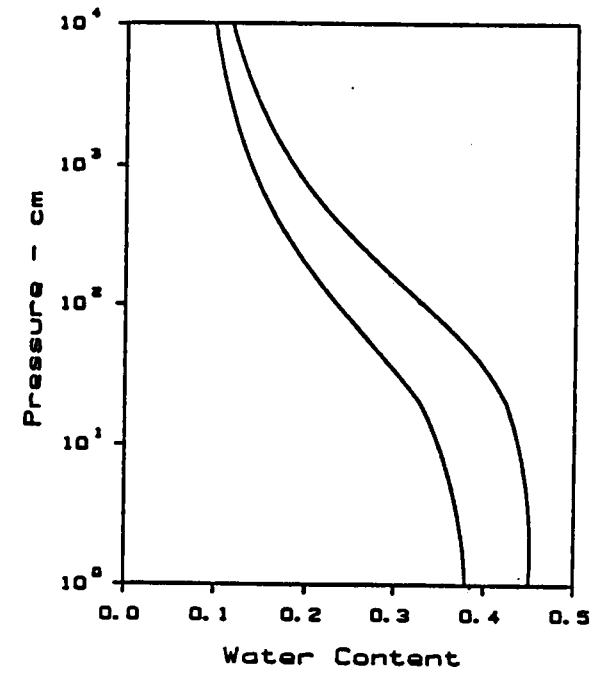

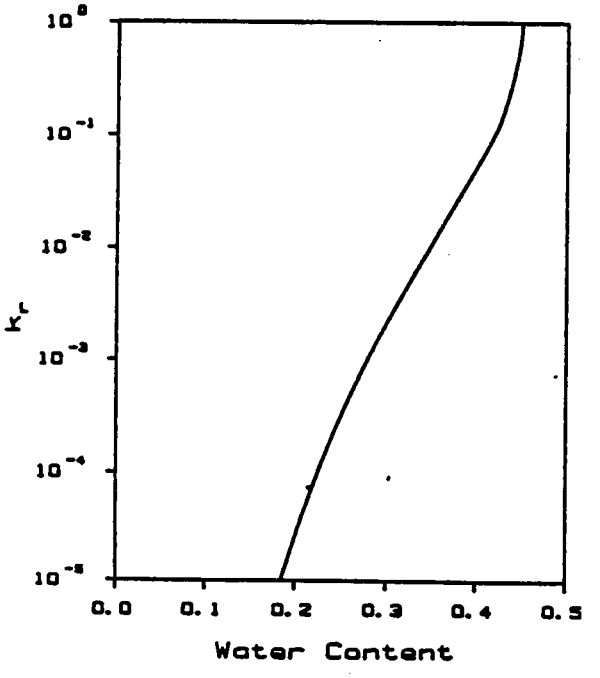

Figure 5.2 Soil hydraulic properties used in simulations.

Rate constants for nitrogen transport K_1, K_2, K_3, K_4 and K_5 were assumed to be 0.02, 0.0063, 0, 0.02 and 0.0063 h^{-1}, respectively. The distribution coefficient for NH_4^+-N adsorption is 1.0 cm^3 g^{-1}. The effective molecular diffusion coefficient (D_O) is taken as 0.12 cm^2 h^{-1} and longitudinal and transverse dispersivities are assumed to be 1.0 and 0.2 cm, respectively.

Example I

From an equilibrium initial condition for the flow problem, water was ponded at the soil surface in region AB (Fig. 5.1) while the remainder of the upper surface and the entire lower boundary received zero flux. Seepage boundaries were stipulated on both sides. Zero initial concentrations were assumed throughout the domain. Influent solution applied at the upper surface was taken to have NH_4^+-N and NO_3^--N concentrations of 50 and 10 ppm, respectively, modeled by third-type boundary conditions. Predicted NO_3^--N concentrations along the center line are shown in Fig. 5.3. Here and elsewhere, H indicates simulations which employ the hysteretic θ-h relations, ND denotes nonhysteretic analyses with the main drainage θ(h) curve and NW denotes those for the main wetting curve. Rapid movement of NO_3^--N for the ND simulation relative to the H and NW cases is evident. Total NH_4^+-N mass for the ND simulation is also very much higher than that predicted for the H and NW simulations (Fig. 5.4). Similar results are available with cumulative Org-N distribution shown in Fig. 5.5 where the Org.-N content increases steadily with time. One of the reasons for this behavior is that the mineralization rate constant of Org-N was

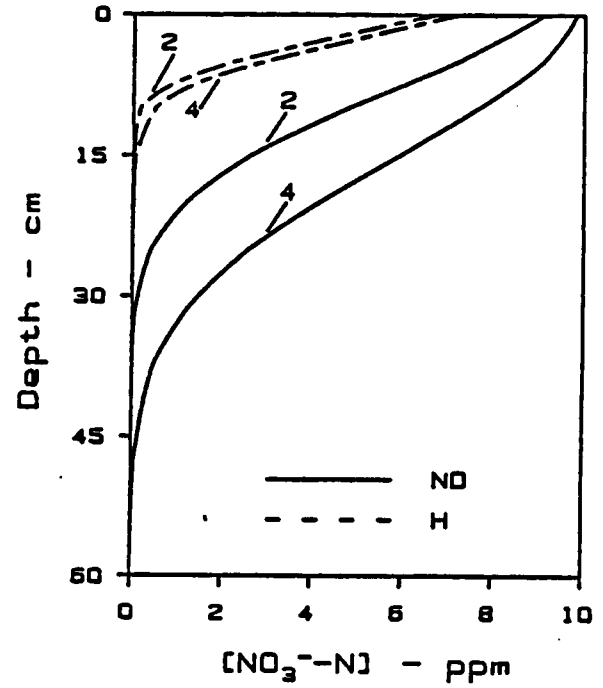

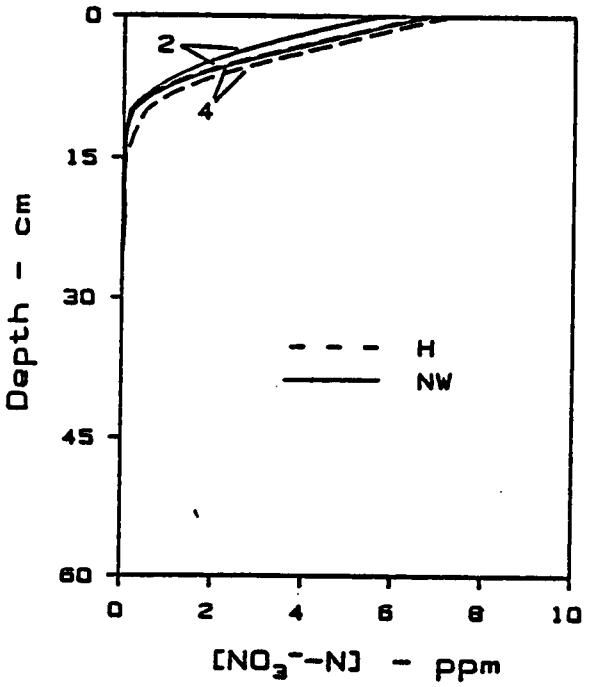

Figure 5.3 Distribution of NO_3^--N concentration along the center line for Example I.

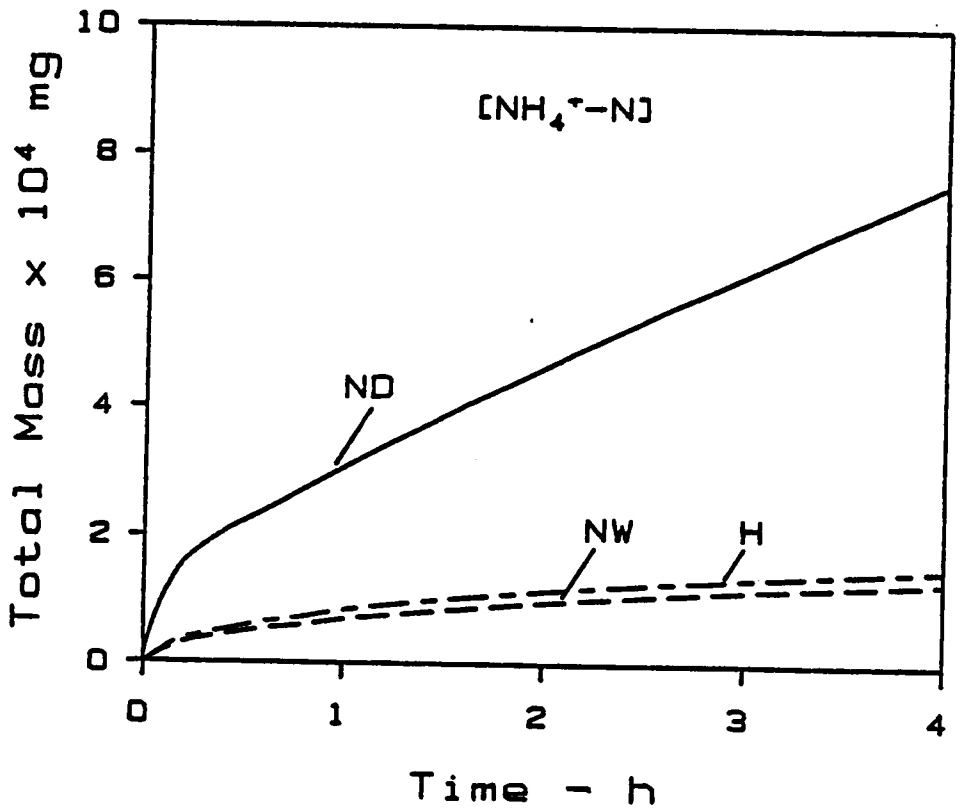

Figure 5.4 Cumulative distribution of NH_4^+-N with time for Example I.

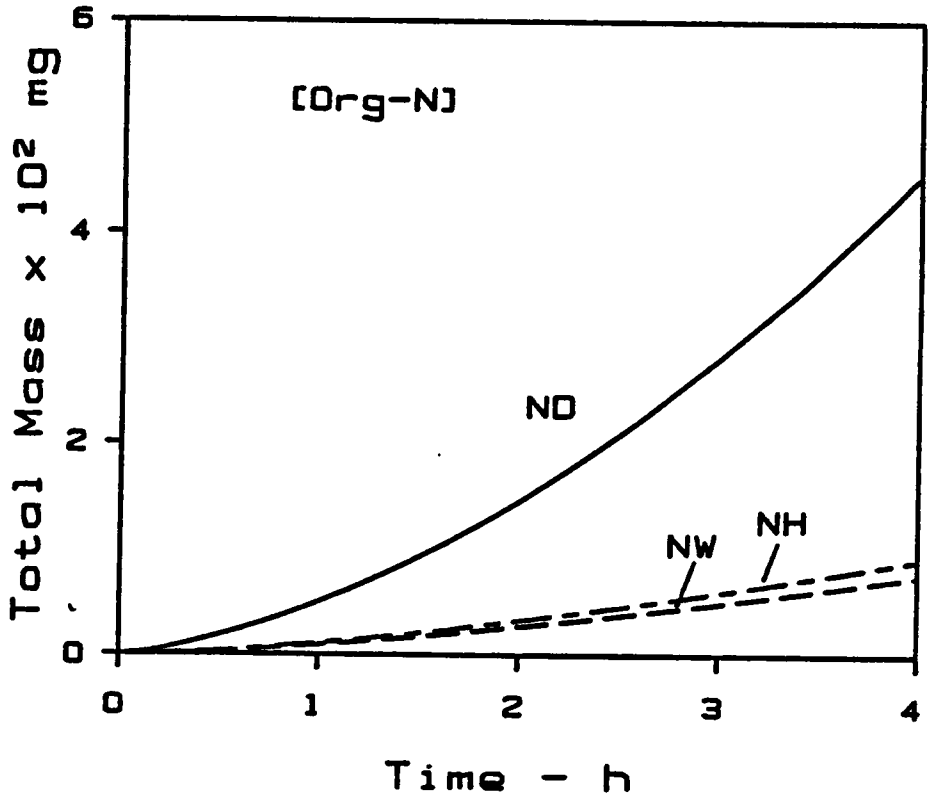

Figure 5.5 Cumulative distribution of Org.-N with time for Example I.

assumed to be zero while immobilization was considered with both NH_4^+-N and NO_3^--N. The differences in results with different saturation paths mainly reflect reductions in hydraulic conductivity at the soil surface and hence in infiltration rates for H and NW cases due to lower water contents caused by air entrapment. This suggests that if effective rather than actual saturated water contents and conductivites are used to analyze flow, neglecting hysteresis may be justifiable. Also the effects of hysteresis could have been reduced if air entrapment was absent in the pressure-saturation relationship. This is due to reduction in differences in water contents between different saturation paths.

Example II

The flow domain geometry in Example II is identical to that of the Example I except that buried line sources have been added at locations C and D. For $0<t<1.3$ h, the entire top surface had a solute free hydraulic flux of 6.0 cm h^{-1} and flow at each line source of 10 cm^3 cm^{-1} h^{-1}. Influent concentrations of NH_4^+-N and NO_3^--N were 50 and 10 ppm, respectively. For $1.3h<t<36.3$ h, the top surface had an evaporative hydraulic flux of 0.005 cm h^{-1} and zero solute flux. For $t>36.3$ h, the surface evaporative flux remained the same, but the water supply at the line sources was shut off. Other boundary and initial conditions were the same as for Example I. Predicted NO_3^--N distributions on a vertical plane intersecting either line source are given in Fig. 5.6. These results are very much different to that of the previous example and indicate little difference between H simulations

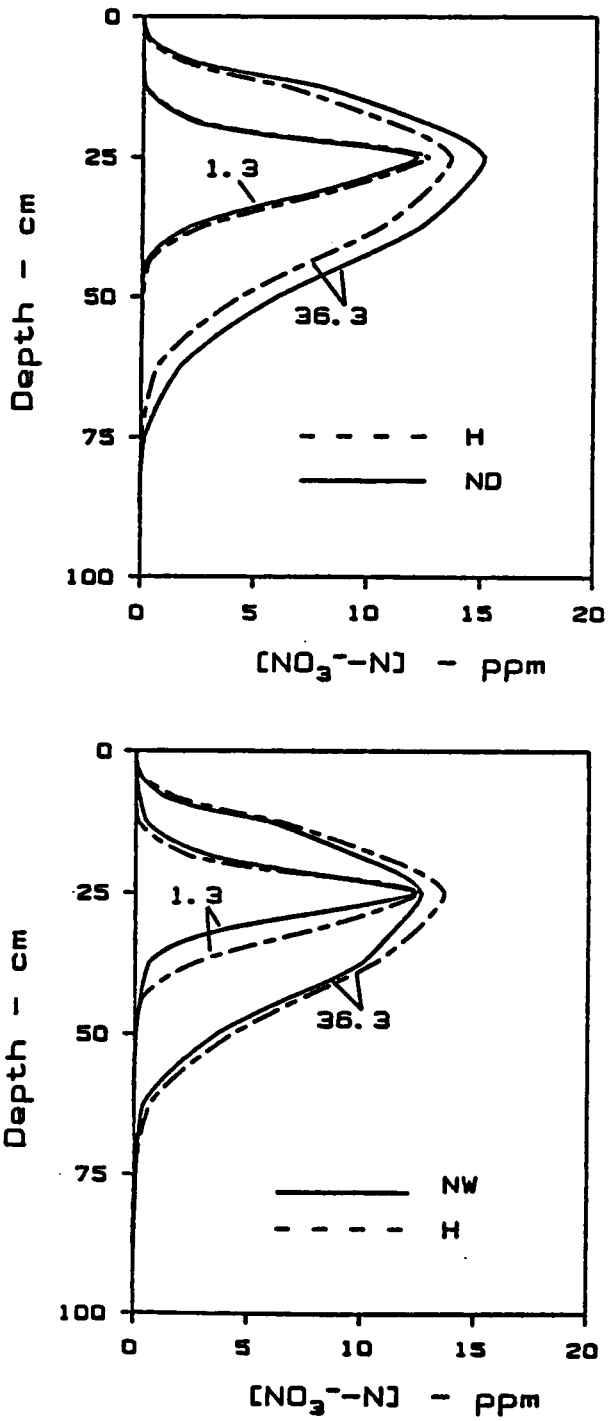

Figure 5.6 Distribution of NO_3^--N concentration along any given line source for Example II.

and either NW or ND cases. The insensitivity to hysteresis may be attributed to the fact that solute velocities are controlled principally by source strength rather than by soil properties for this problem. Although the top surface had a potential type boundary condition, the water entering the system was nitrogen-free except the line sources. Since the line source were analysed as point source in the simulations, the total mass entering the system remained same for the three cases. The only effect of hysteresis under such conditions is the flow velocities and water contents associated with the different saturation paths. In the present simualtion, these variables did not affect very much as the high intensity of the line sources (compared to the saturated hydraulic conductivity) created saturated zones with different saturation paths in the viscinity of the sources causing near constant velocities and water contents. Also it is interesting to note that the concentration distribution after 72 h (not shown) was almost identical to that at 36.3 h (Fig. 5.6) even though the surface boundary continued with an evaporation condition beyond 36.3 h. The evaporative flux is small compared to the line source strength and quasi-steady state conditions are maintained.

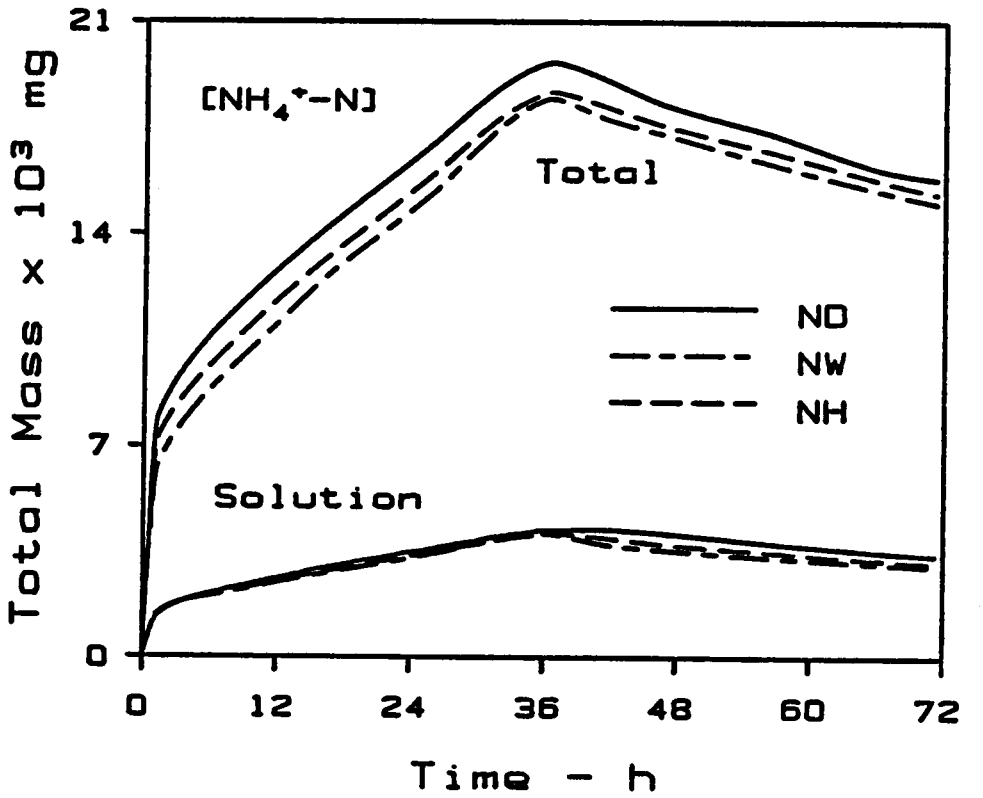

Figure 5.7 Cumulative distribution of NH_4^+-N with time for Example II.

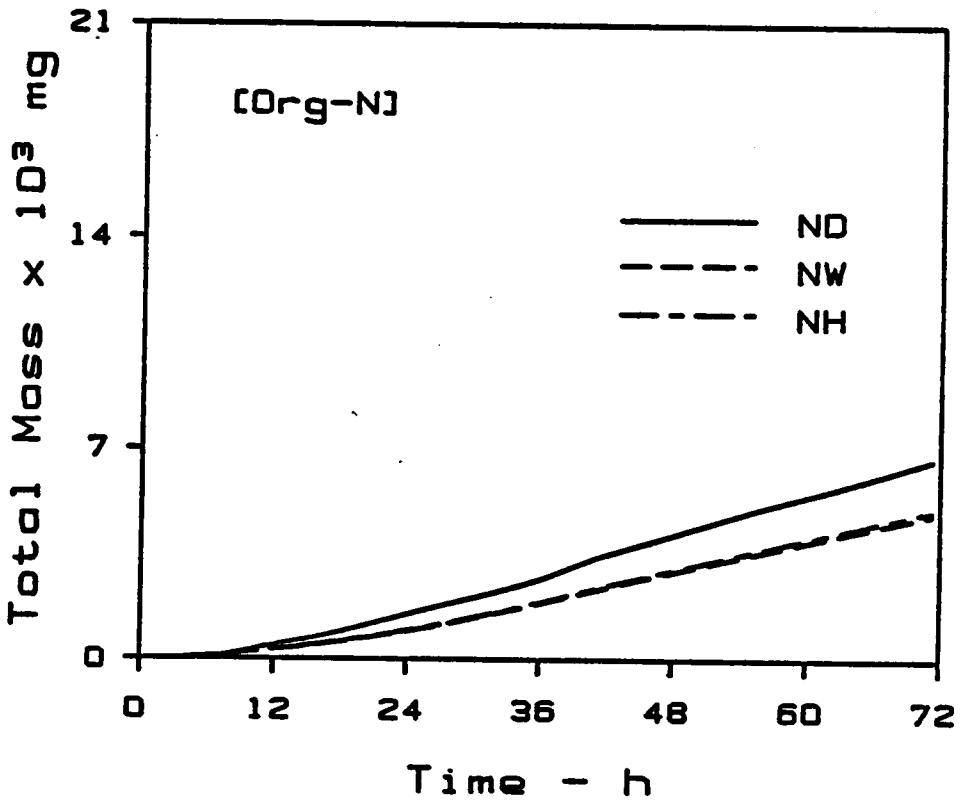

Figure 5.8 Cumulative distribution of Org.-N with time for Example II.

CONCLUSIONS

Effects of air entrapment and hysteresis in water retention relations on flow can may have substantial effects on species transport under certain conditions. For potential-type hydraulic boundary conditions, fluid entrapment results in markedly lower solute velocities compared to nonhysteretic simulations based on main drainage $\theta(h)$ parameters, while nonhysteretic analyses using the main wetting branch closely approximate hysteretic results. Since these effects are attributable principally to differences in hydraulic conductivities at apparent water saturation for wetting and drying paths, it follows that effects of disregarding hystersis will also be small if data for a primary drainage path beginning from $\theta_s{}^w$ were employed. For solute introduction via controlled flux line sources, effects of hysteresis on transport were observed to be quite small and simulation with either wetting or draining water retention data provided an adequate representation of the hysteretic system.

REFERENCES

Jones, M. J. and R. W. Gillham, Effects of soil water hysteresis on solute movement during intermittent leaching, Water Resour. Res., 23, 1251-1256, 1987.

Kool, J. B. and J. C. Parker, Development and evaluation of closed-form expressions for hysteretic soil hydraulic properties, Water Resour. Res., 23, 105-114, 1987.

Pickens, J. F., R. W. Gillham and D. R. Cameron, Finite element analysis of the transport of water and solutes in tile-drained soils, J. Hydrol., 40: 243-264, 1979.ol

Pickens, J. H. and R. W. Gillham, Finite element analysis of solute transport under hysteretic unsaturated flow conditions, Water Resour. Res., 16, 1071-1078, 1980.

van Genuchten, M. Th., A closed-form equation for predicting the hydraulic conductivity of unsaturated soils, Soil Sci. Soc. Am. J., 44,892-898, 1980.

APPENDIX A

Influence Coefficient Matrices For Linear Rectangular Elements - Flow Problem

$$[T^*] = \frac{1}{9}\begin{bmatrix} 4 & 2 & 1 & 2 \\ 2 & 4 & 2 & 1 \\ 1 & 2 & 4 & 2 \\ 2 & 1 & 2 & 4 \end{bmatrix} \qquad [S^*_x] = \frac{1}{6}\begin{bmatrix} 2 & -2 & -1 & 1 \\ -2 & 2 & 1 & -1 \\ -1 & 1 & 2 & -2 \\ 1 & -1 & -2 & 2 \end{bmatrix}$$

$$[S_z^*] = \frac{1}{6}\begin{bmatrix} 2 & 1 & -1 & -2 \\ 1 & 2 & -2 & -1 \\ -1 & -2 & -2 & 1 \\ -2 & -1 & 1 & 2 \end{bmatrix} \qquad \{V^*\} = \begin{Bmatrix} -1 \\ -1 \\ 1 \\ 1 \end{Bmatrix}$$

APPENDIX B

Influence Coefficient Matrices for Linear Triangular Elements - Flow Problem

$$[T^*] = \frac{\Delta}{12}\begin{bmatrix} 2 & 1 & 1 \\ 1 & 2 & 1 \\ 1 & 1 & 2 \end{bmatrix}$$

$$[S_X^*] = \frac{1}{4\Delta}\begin{bmatrix} \beta_1\beta_1 & \beta_1\beta_2 & \beta_1\beta_3 \\ \beta_2\beta_1 & \beta_2\beta_2 & \beta_2\beta_3 \\ \beta_3\beta_1 & \beta_3\beta_2 & \beta_3\beta_3 \end{bmatrix}$$

$$[S_Z^*] = \frac{1}{4\Delta}\begin{bmatrix} \gamma_1\gamma_1 & \gamma_1\gamma_2 & \gamma_1\gamma_3 \\ \gamma_2\gamma_1 & \gamma_2\gamma_2 & \gamma_2\gamma_3 \\ \gamma_3\gamma_1 & \gamma_3\gamma_2 & \gamma_3\gamma_3 \end{bmatrix} \qquad \{V^*\} = \frac{1}{2}\begin{Bmatrix} \gamma_1 \\ \gamma_2 \\ \gamma_3 \end{Bmatrix}$$

$\alpha_1 = (x_2z_3 - x_3z_2)$; $\alpha_2 = (x_3z_1 - x_1z_3)$; $\alpha 3 = (x_1z_2 - x_2z_1)$

$\beta_1 = z_1 - z_3$; $\beta_2 = z_3 - z_1$; $\beta_3 = z_1 - z_2$

$\gamma_1 = x_3 - x_2$; $\gamma_2 = x_1 - x_3$; $\gamma_3 = x_2 - x_1$

$2\Delta = (z_3 - z_1)(x_2 - x_1) - (z_2 - z_1)(x_1 - x_3)$

APPENDIX C

Soil Hydraulic Properties of Wagner et al. (1980) Problem

$$\psi = \psi_a \, (\theta/\theta_s)^{-b}$$

$$K = K_s \, (\psi/\psi_a)^c$$

ψ_a - air entry pressure

θ_s - saturated moisture content

K_s - saturated hydraulic conductivity

Soil	b	c	ψ_a(cm)	θ_s	K_s (cm h^{-1})
1	4.05	-2.494	-12.1	0.395	63.36
2	4.38	-2.457	-9.0	0.410	56.28
3	4.9	-2.408	-21.8	0.435	12.48
4	5.3	-2.377	-78.6	0.485	2.592
5	5.39	-2.371	-47.8	0.451	2.502

APPENDIX D

Unsymmetric Upstream Weighting Functions For Linear Rectangular Elements

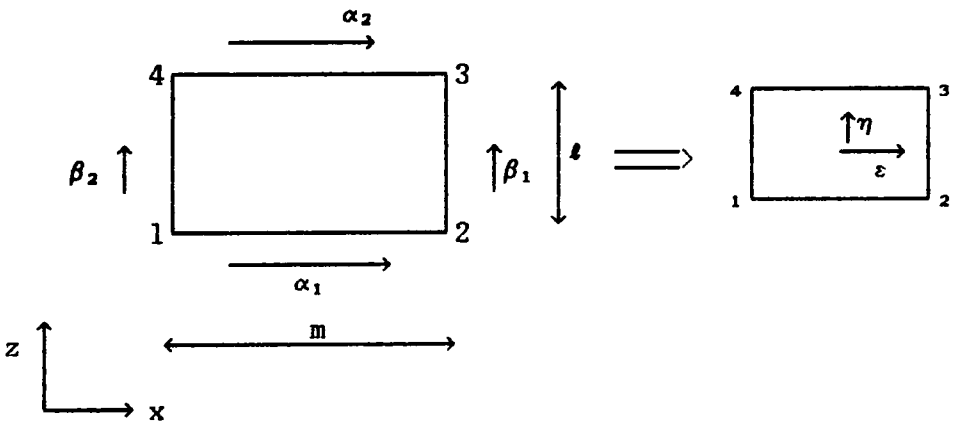

Fig. D-1

Fig. D-2

$$N_i = \frac{1}{4}(1 + \varepsilon\varepsilon_i)(1 + \eta\eta_i) \qquad \varepsilon_i = \pm 1 \text{ and } \eta_i = \pm 1$$

$$x = \sum_{i=1}^{4} N_i(\varepsilon,\eta)\, x_i \qquad z = \sum_{i=1}^{4} N_i(\varepsilon,\eta)\, z_i$$

$$W_1 = \frac{1}{16}\left[(1+\varepsilon)(-3\alpha_2\varepsilon+3\alpha_2+2)\right]\left[(1+\eta)(-3\beta_1\eta+3\beta_1+2)\right]$$

$$W_2 = \frac{1}{16}\left[(1+\varepsilon)(-3\alpha_1\varepsilon+3\alpha_1+2)\right]\left[(1+\eta)(3\beta_1\eta-3\beta_1-2)+4\right]$$

$$W_3 = \frac{1}{16}\left[(1+\varepsilon)(3\alpha_1\varepsilon-3\alpha_1-2)+4\right]\left[(1+\eta)(3\beta_2\eta-3\beta_2-2)+4\right]$$

$$W_4 = \frac{1}{16}\left[(1+\varepsilon)(3\alpha_2\varepsilon-3\alpha_2-2)+4\right]\left[(1+\eta)(-3\beta_2+2)\right]$$

To determine signs of α or β along a given side IJ, let e_{IJ} denote the direction vector of the given side (positive direction shown in Figure A-1). If q_I and q_J are velocity vectors at nodes I and J respectively and the average velocity q^* is given as:

$$q^* = 1/2\ (q_I + q_J) \cdot e_{IJ}$$

then α (or β) $\succ 0$ if $q^* \succ 0$ and

α (or β) $\prec 0$ if $q^* \prec 0$

To evaluate values of the weighting function $W_I(\alpha,\beta)$ and its derivatives $W_I(\alpha,\beta)$, $\partial W_I/\partial x$ and $\partial W_I/\partial z$, the following procedure is recommended:

$W_I(\alpha,\beta)$ along x -direction $\equiv$ $W_I(\alpha,0)$

$W_I(\alpha,\beta)$ along z -direction $\equiv$ $W_I(0,\beta)$

$$\frac{\partial W_I(\alpha,\beta)}{\partial x} \equiv \frac{\partial W_I(\alpha,0)}{\partial x}$$

$$\frac{\partial W_I(\alpha,\beta)}{\partial z} \equiv \frac{\partial W_I(0,\beta)}{\partial z}$$

where I = 1, 4 and α (or β) will be α_1 or α_2 (β_1 or β_2) depending on the side considered (Fig. D-1).

APPENDIX E

Influence Coefficient Matrices for Linear Rectangular Elements - Transport Problem

$$\left[T_D{}^x\right] = \frac{1}{6}\begin{bmatrix} 2 & -2 & -1 & 1 \\ -2 & 2 & -1 & -1 \\ -1 & 1 & 2 & -2 \\ 1 & 1 & -2 & 2 \end{bmatrix} \qquad \left[T_D{}^z\right] = \frac{1}{6}\begin{bmatrix} 2 & 1 & 1 & 2 \\ 1 & 2 & -2 & -1 \\ -1 & -2 & 2 & 1 \\ -2 & -1 & 1 & 2 \end{bmatrix}$$

$$\left[T_V{}^x\right] = \frac{1}{6}\begin{bmatrix} -2 & 2 & 1 & -1 \\ -2 & 2 & 1 & -1 \\ -1 & 1 & 2 & -2 \\ -1 & 1 & 2 & -2 \end{bmatrix} \qquad \left[T_V{}^z\right] = \frac{1}{6}\begin{bmatrix} -2 & -1 & 1 & 2 \\ -1 & -2 & 2 & 1 \\ -1 & -2 & 2 & 1 \\ -2 & -1 & 1 & 2 \end{bmatrix}$$

$$\left[T_V{}^{xu}\right] = \frac{1}{6}\begin{bmatrix} 2\alpha_1 & -2\alpha_1 & -\alpha_1 & \alpha_1 \\ -2\alpha_1 & 2\alpha_1 & \alpha_1 & -\alpha_1 \\ -\alpha_2 & \alpha_2 & 2\alpha_2 & -2\alpha_2 \\ \alpha_2 & -\alpha_2 & -2\alpha_2 & \alpha_2 \end{bmatrix}$$

$$\left[T_V{}^{zu}\right] = \frac{1}{6}\begin{bmatrix} 2\beta_2 & \beta_2 & -\beta_2 & -2\beta_2 \\ \beta_1 & 2\beta_1 & -2\beta_1 & -\beta_1 \\ -\beta_1 & -2\beta_1 & 2\beta_1 & \beta_1 \\ -2\beta_2 & -\beta_2 & \beta_2 & 2\beta_2 \end{bmatrix}$$

$$[S^*] = \frac{1}{9}\begin{bmatrix} 4 & 2 & 1 & 2 \\ 2 & 4 & 2 & 1 \\ 1 & 2 & 4 & 2 \\ 2 & 1 & 2 & 4 \end{bmatrix} \qquad \{U\} = \begin{Bmatrix} 1 \\ 1 \\ 1 \\ 1 \end{Bmatrix}$$

APPENDIX F

Publications Assoicated with Research

Kaluarachchi, J. J. and J. C. Parker, 1987, Finite element analysis of water flow in variably saturated soil, J. Hydrol., 90: 269-291.

Kaluarachchi, J. J. and J. C. Parker, 1987, Effects of hysteresis with air entrapment on water flow in the unsaturated zone, Water Resour. Res., 23: 1967-1976.

Kaluarachchi, J. J. and J. C. Parker, 1987, Finite element model of Nitrogen species transformation and transport in the unsaturated zone, J. Hydrol., (in press).

Kaluarachchi, J. J. and J. C. Parker, 1988, Finite element simulation of Nitrogen transformation and transport during hysteretic flow with air entrapment, accepted and to be appeared at the VII International Conference on Computational Methods in Water Resources, To be held at Massachusetts Institute of Technology, Massachusetts.

The vita has been removed from the scanned document